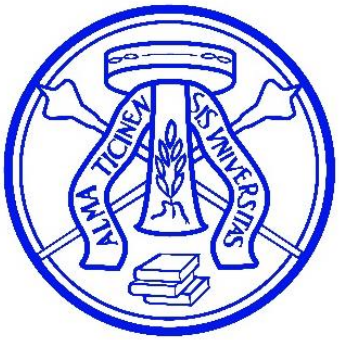

UNIVERSITÀ DEGLI STUDI DI PAVIA

DOTTORATO IN SCIENZE CHIMICHE E FARMACEUTICHE E INNOVAZIONE INDUSTRIALE

(XXXV Ciclo)

Coordinatore: Chiar.mo Prof. Giorgio Colombo

Design and Characterization of Hybrid Perovskite for New Generation Solar Cells

Tesi di Dottorato di
Matteo Degani

AA 2021/2022

Tutor
Chiar.ma Prof.ssa Giulia Grancini

Index

1 Introduction

1.1 Energy challenge

The global energy demand is annually increasing due to the rapid growth of the world's population, and the increasing development of industrial society[1]. Environmental impacts such as air pollution and climate change have resulted from energy generation driven by fossil fuels, and this has gained considerable attention not only from scientists but also from the general community.

1.1.1 Motivation and background: the problem of climate change

The Earth's temperature results from an equilibrium established between the incoming radiation from the Sun and the energy radiated back by the Earth. The outgoing radiation emitted is strongly affected by the presence and composition of the Earth's atmosphere. Although the atmosphere is necessary for life excess of the greenhouse effect can be dangerous for life on the planet. Since, the XVII century human activities have influenced greenhouse gas concentration, related to the industrial revolution. Land and ocean have taken up a near-constant proportion (globally about 56% per year) of CO emissions from human activities over the past six decades, related to the development of technology in other countries such as India and China whose impact is huge on the high population present in those territories. As shown in figure 1, since 1850 the earth became warmer, especially the global surface temperature was 1.09 [0.95 to 1.20] °C higher in 2011– 2020 than 1850–1900, with larger increases over land 1.59 °C from 1.34°C up to 1.83 °C than in the ocean 0.88°C from 0.68°C up to 1.01°C[2].

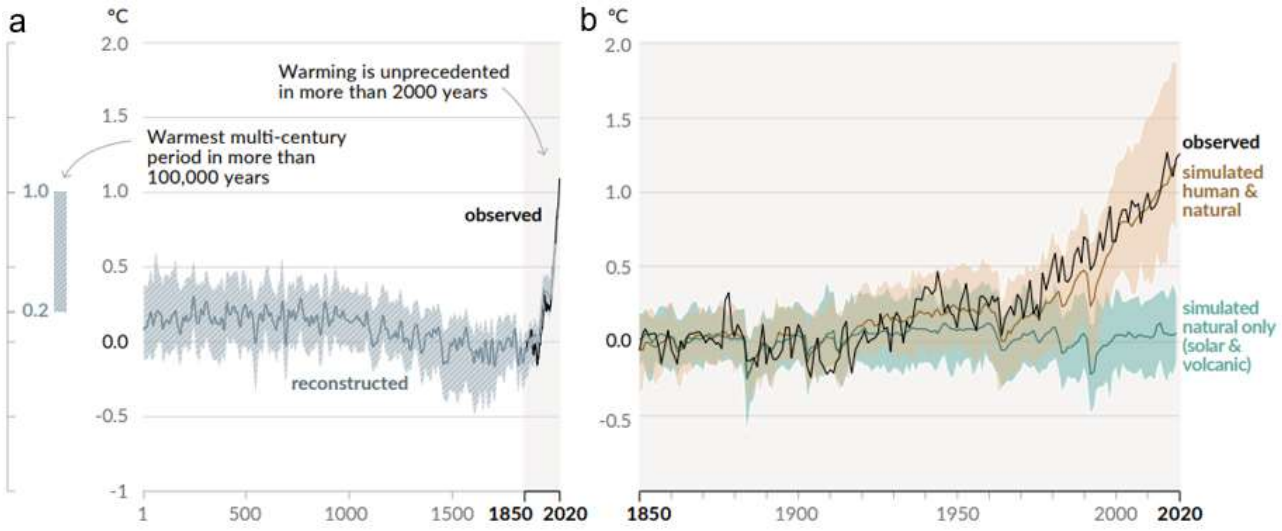

Figure 1 – History of global temperature change and causes of recent warming. a) change in global surface temperature (decadal average as reconstructed (1-2000) and observed (1850-2020) b) change in global surface temperature (annual average) as observed and simulated using human &natural and only natural factors (both 1850-2020)[2].

Human activities have now reached a scale where they are impacting the planet's environment and its attractiveness to humans and for life. The side effects can be devastating and technologies with low

environmental impact and zero "greenhouse gas" emissions are expected to become increasingly important in the coming decades. Since the energy sector is the major producer of "greenhouse gases" via the combustion of fossil fuels, and for their non-renewable nature, alternative clean sources of energy are the best solution for the issue. In recent years, several clean sources of energy have been introduced, such as wind power, waterpower, and solar energy. The aforementioned sources are known as “renewable sources of energy”. Today, electricity generation from renewable energy sources shows rapid development. The share of renewable resources in global power generation is expected to increase from 26% in recent years to 90% in 2050[3].

1.1.2 Potential of renewable energy

Despite lower electricity demand and wholesale power price drops due to the pandemic crisis, as shown in figure 2, governments around the world auctioned a record amount of renewable energy capacity, awarding almost 75 GW of wind, solar PV and bioenergy last year – 20% more than in 2019[4]. Solar PV, and wind are set to contribute two-thirds of renewable growth[5].

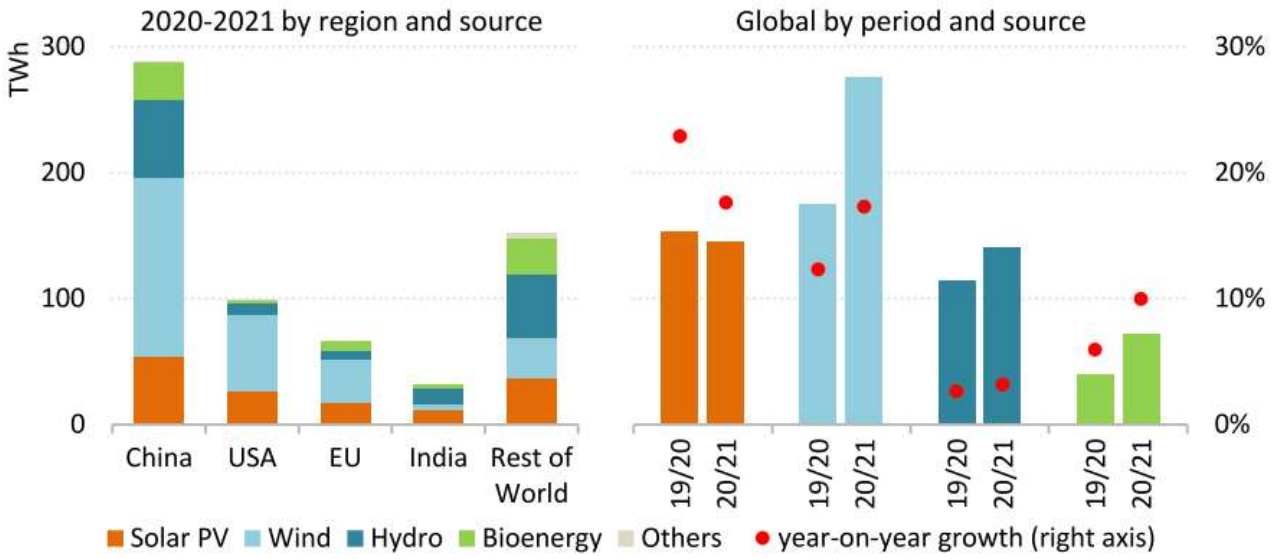

Figure 2 – Electricity generation from renewable sources increases by technology, country, and region in 2020–2021[6].

Among the available renewable energy resources, solar energy is the most abundant, globally accessible, and clean source of energy to supply the globally growing energy demand for future generations. Promisingly, in recent years electricity production from solar energy shows a significant enhancement. The share of power production from solar energy is predicted to increase from almost 115GW/yr to 444GW/yr in 2050. Therefore, improvement and optimization of the existing technologies and development of novel technologies are critical subjects for the scientific and economic communities.

1.1.3 Properties of sunlight

The Sun is a star, for simplicity is usually represented as a sphere of plasma whose internal temperatures reach over 20 million Kelvin due to nuclear fusion reactions at the Sun's core. The energy produced in this way is transferred to the outer part firstly throw thermal radiation, then by convection until the surface of the Sun is called “photosphere”. It has a temperature of about 6000 K number used commonly for calculations, but 5778 K is a more accurate approximation. To estimate the energy that arrives at the earth is possible to approximate the Sun as a blackbody in thermal equilibrium at the temperature mentioned above. Using Plank’s equation given by

$$F(\lambda) = \frac{2\pi hc^2}{\lambda^5 \left(exp\left(\frac{hc}{k\lambda T}\right) - 1\right)} \tag{1}$$

Where F is the spectral irradiance [Wm^{-3}], λ is the wavelength of light (m), T is the temperature of the blackbody (K), h is the Planck constant, c is the speed of light, an k is Kelvin constant. Using the equation above, and a temperature of 5800 K, it is possible to calculate the radiant power density throw the equation

$$H = \int_0^\infty F(\lambda)\, d\lambda \tag{2}$$

gives the radiation of H_{sun} = 64 x 10^6 W/m^2. The calculation is made knowing the Sun adius of 695 x 10^6 m so the surface area is 6.07 x 10^{18} m^2, which is equal to 3.9 x 10^{26} watts. Even considering that only a small amount hit the earth’s surface is an enormous amount of power. The power emitted from the Sun is composed by an electromagnetic radiation, starting from the UV up to infrared. The incident light of the Sun without atmospheric absorption is also called AM0. As solar radiation passes through the atmosphere, the incident photons are absorbed by the gases and dust. Specific gasses, notably ozone (O_3), carbon dioxide

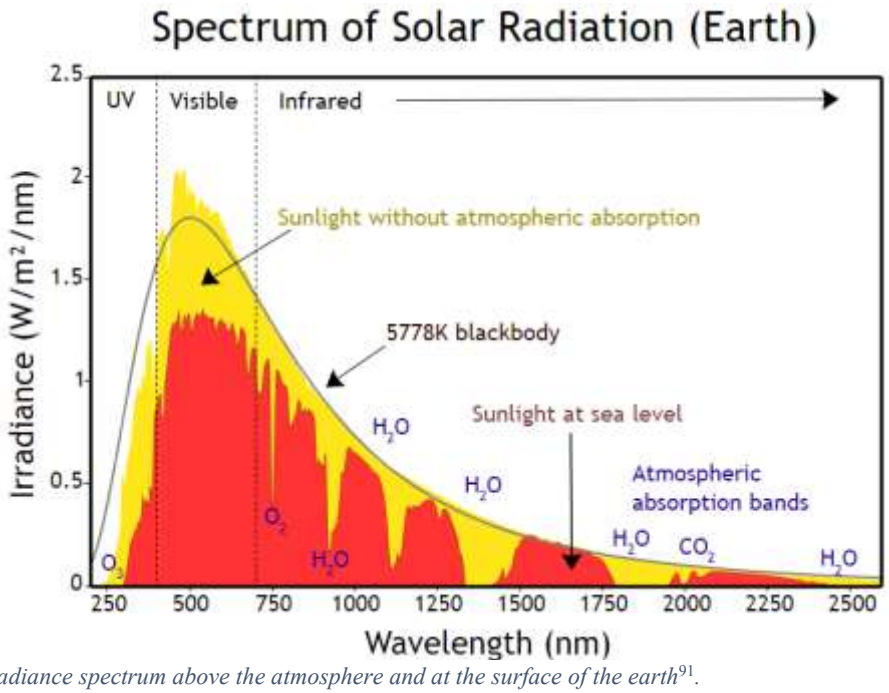

Figure 3 – Solar irradiance spectrum above the atmosphere and at the surface of the earth[91].

(CO_2), and water vapor (H_2O), have a very high absorption of photons that have energies close to the bond energies of these atmospheric gases. This absorption changes the shape of the spectrum and the effective intensity that hits the earth surface also called AM1,5. Scattering is the major responsible of the reduction of the short wavelengths that is also the reason of the coloration of the sky and the Sun; yellow during the day and orange/red during the sunlight or the sunset. At long wavelength the molecules mentioned before have a stronger absorption. A representative graph of the solar spectrum as a blackbody, as arrives before passing the atmosphere and after the absorption of the atmosphere is presented in figure 3.

Considering solar cells with 8% of PCE are necessary only 6 discs represented in the map to fully cover global energy demand. The total amount in the area is around less than 1000 km^2, despite looking unignorable number if we think about the desert areas this value is negligible.

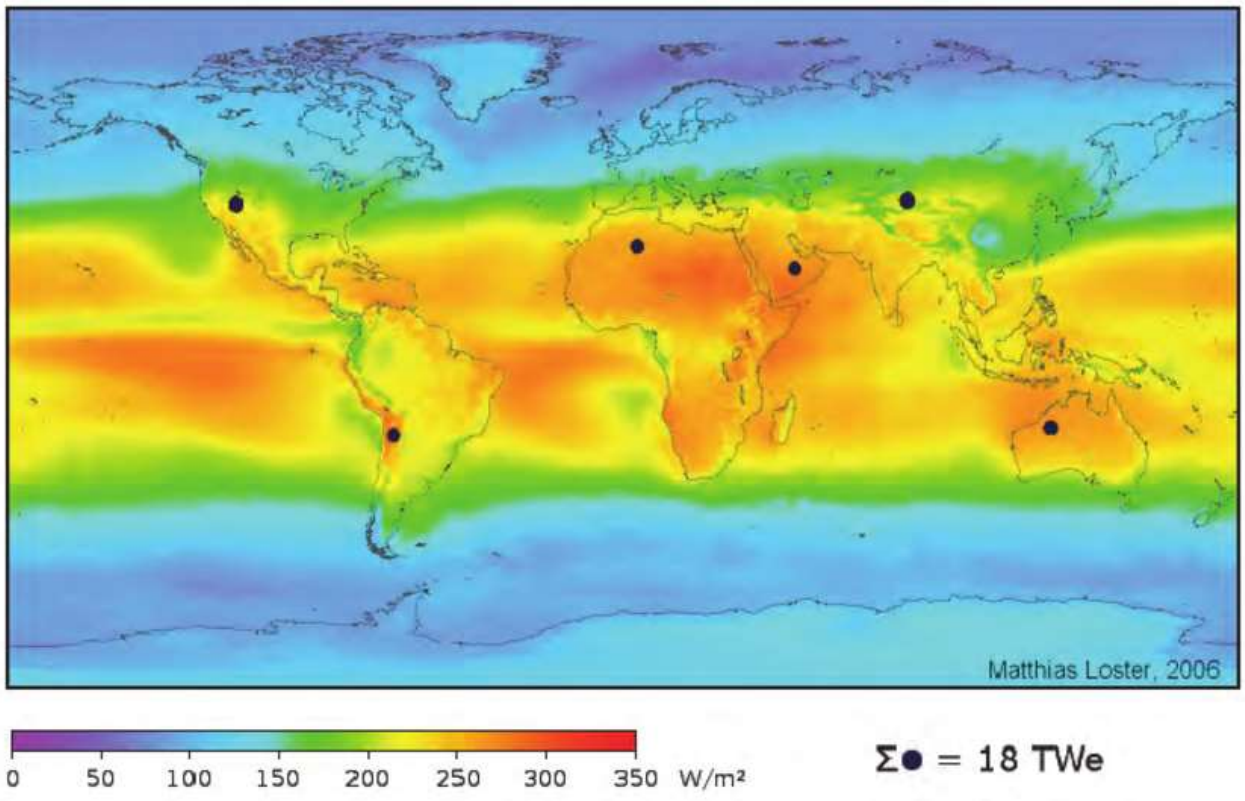

Figure 4 – Global average solar irradiance. The six black spots are the areas required to be used by solar panels with an efficiency of 8% which will produce enough to fulfill the global energy requirement[7].

1.2 Semiconductors materials

A semiconductor material has an electrical conductivity lower respect a conductor, such metals (silver, gold, etc.), and higher respect an insulator, such as plastic or glass. The elements called semiconductors are those composed of single species of atoms such as silicon Si, germanium Ge, selenium (Se), or tellurium (Te). There are, however, numerous semiconductor compounds composed of two or more elements as a

combination of group III and group V (called III-V semiconductors), or of combinations from group II and group VI (called II-VI semiconductors), or more complex compounds.

1.2.1 Semiconductor: physics

To describe the electric properties of semiconductors is necessary to describe the crystal structure of the semiconductors. When a molecule is formed at least a pair of atoms are involved, and their atomic orbitals combine to form pairs of molecular orbitals these orbitals have higher and lower energy respecting the atomic orbitals. We say that the energy levels have split. When a very large number of atoms come together as in a solid, each atomic orbital splits into a very large number of levels, so close together in an energy that they form a continuum of allowed levels, also called band. These bands, are occupied depending on the original molecular orbitals occupancy. The highest occupied band is called valence band (VB), which contains the valence electrons. The lowest unoccupied band is called the conduction band (CB) and this band has the first energy levels empty.

In a solid, the Energy gap (E_g) is an energy range in a solid where no electronic states can exist. The energy necessary to promote an electron is equal to the first free level in the CB (E_C) minus the energy of the level in which the electron is in the VB (E_V)

$$E_g = E_C - E_V \tag{3}$$

In figure 5 it is represented the electronic band structure of solids, the band gap generally refers to the difference between the top of the valence band (highest band occupied) and the bottom of the conduction band (lowest empty band). Matter can be subdivided depending on the E_g value: conductors (E_g don't exist); semimetals (E_g higher than 0 and lower than 0.5eV); semiconductors (roughly E_g in the range of 0.5 to 3eV) and insulators (E_g >3eV). The semiconductor needs kinetic energy for the electrons that can break the electron bond, and the vibrations of the lattice can give this energy if the temperature is enough high.

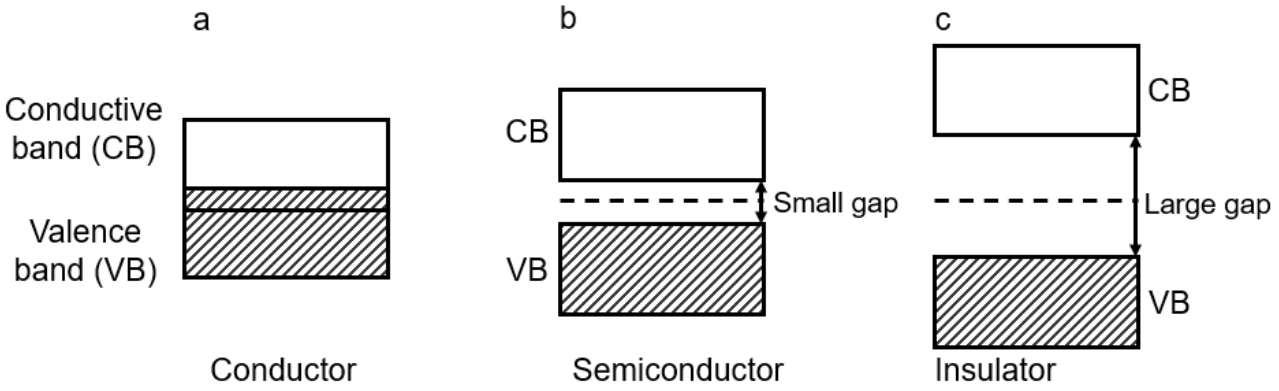

Figure 5 – Energy level diagrams for (a) metal, (b) a semiconductor and (c) an insulator. The bands are filled with electrons up to the Fermi level E_F. This is indicated by the pattern filling.

The electrons produced can travel and transport charge or energy. The vacancies left behind the promoted electrons are also able to move and conduct, these positive charges are possible to represent as quasi-particles called holes. Since holes form when an electron is released, the number of holes must coincide with the number of free electrons. Indicating n as the concentration of electrons per unit volume [cm^{-3}] and p as the concentration of holes

$$n = p = n_i \qquad np = n_i^2 \tag{4}$$

At 0K the VB is filled, and the CB is empty. This collocated the Fermi level (E_F)in the middle of the band gap. In this condition E_F is far enough from both band edges then is possible to use the Maxwell-Boltzmann approximation so is possible to write Fermi Dirac static in the simplified form:

$$n_i^2 = np = N_C N_V e^{-E_g/k_B T} \tag{5}$$

Where "n" is the electron density, "p" is the density of the holes, N_C is the effective conduction band density, N_V is the effective valence band density, k_B is the Boltzmann constant, and T is the temperature; n_i is equal to the density of electrons which are thermally excited into the CB of a pure semiconductor in thermal equilibrium and it is equal to holes (for each electron promoted a hole is also created). The concentration of free electrons in silicon at 300 K is around $n_i = 1.02 \cdot 10^{10}$ cm^{-3} where n_i is called the intrinsic concentration of free charge carriers; the term intrinsic (pure) refers to the fact that the structure being analyzed is composed exclusively of silicon atoms. The properties of those bands also determine the conductivity of the carriers given by:

$$\sigma = q\mu_n n + q\mu_p p \tag{6}$$

Where μ_n and μ_p are respectively the mobility of electrons and holes, and q is the electronic charge. At 300K for silicon $\sigma = 3 \cdot 10^{-6}$ $Ohm^{-1}cm^{-1}$ and contrary to metals the conductivity increases with increasing temperature. To improve the conductivity is possible to use a material with lower E_g for example germanium or, another way is introduced to the crystal impurity atom or structural defects.

1.2.2 Doped semiconductors

The impurity or defect introduces bonds of different strengths to those which make up the perfect crystal and therefore changes the local distribution of electronic energy levels. The semiconductor in this case is called doped or extrinsic semiconductor. Depending on the kind of defect is possible to introduce impurity levels above the E_F of the intrinsic material which increases the density of electrons. Alternatively, is possible to introduce unoccupied levels below E_F that increase the density of holes.

A semiconductor that has been doped to increase the density of electrons relative to holes is called n-type (the principal charge carriers are negative). The doping consists in replacing some of the atoms in the crystal

lattice with impurity atoms that possess one too many valence electrons for the number of crystal bonds. Since these impurities give an extra electron to the lattice, they are called donor atoms. Taking as example silicon is possible to do n-doping through elements of the V group as phosphorous. The valence of these atoms is 5 in which 4 electrons are used to create bonds with the silicon atoms the fifth is only a coulombic weak bond to the P atom. These quasi-free electrons form a level E_D just below the CB and require energies of meV to be promoted. In this situation, the E_F shift in a position between CB and E_D, and the electrons donated don't correspond to the creation of a hole, so the conductivity of n-type semiconductors is mainly electrons. The density of carriers can be controlled by varying the density of the donors (N_d). At room temperature the electron also called majority carriers are

$$n \approx N_d \tag{7}$$

Meanwhile, the holes (minority carriers) according to (4) became

$$p = n_i^2/N_d \tag{8}$$

Another possibility is to do the doping with an element that few the valence electrons for the bonds they need to form these impurities are called acceptors. For silicon, the elements of the III group are p-type dopants for example boron. The acceptor removes a valence electron from another bond, this releases a hole. These holes create an energy level (E_A), and the E_f shifts between the VB and E_A. The results are similar to the previous case with the positive charges (now the majority carriers), their density is equal to the density of acceptors

$$p \approx N_a \tag{9}$$

Meanwhile, the electrons (minority carriers) according to (4) became

$$n = n_i^2/N_a \tag{10}$$

The concentrations of dopant that can be inserted range from 10^{13} to 10^{20} cm^{-3}, which is equivalent to saying that the conductivity can increase by 10 orders of magnitude compared to monocrystalline silicon. Heavy doping is also likely to increase the density of defect states which act as centers for carrier recombination or trapping.

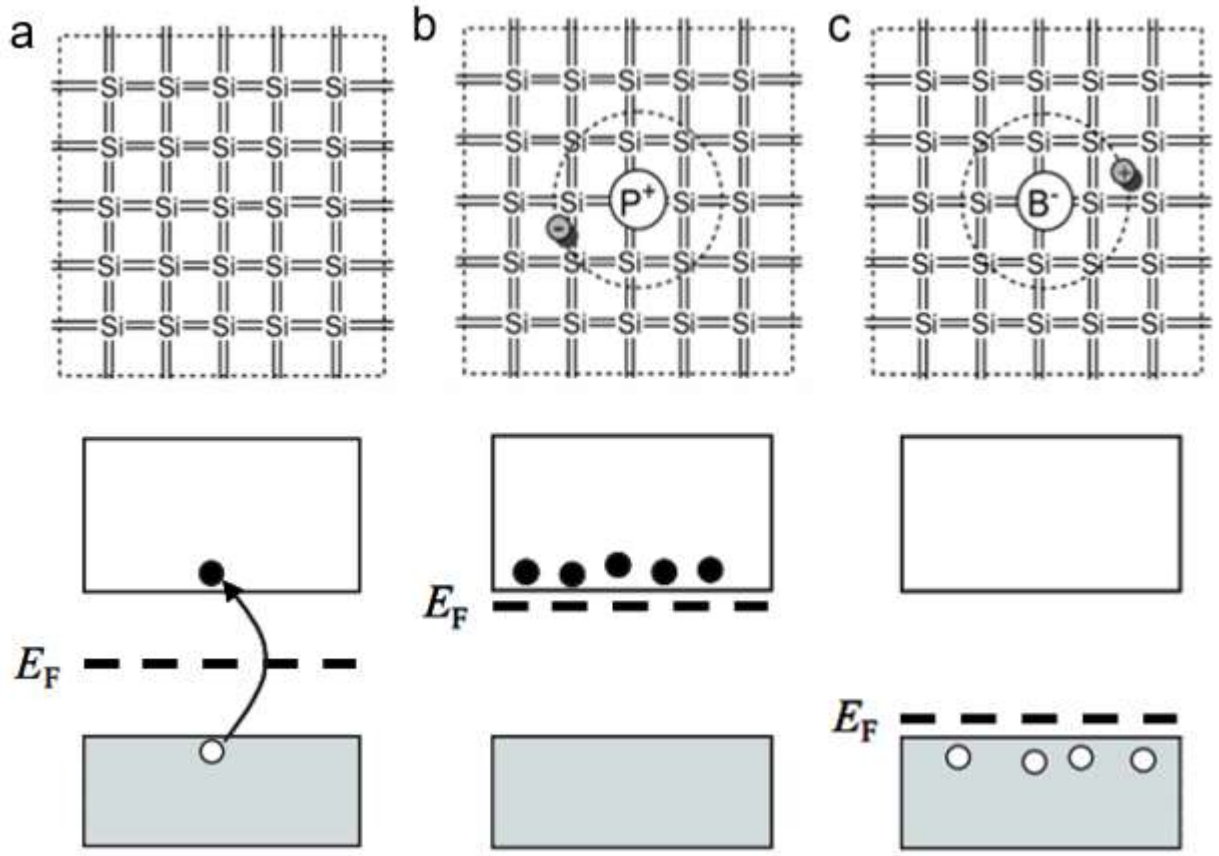

Figure 6 – schematic of silicon crystal lattice, valence, and conduction bands for: (a) a pure (intrinsic) semiconductor; (b) a semiconductor with n-type doping; and (c) a semiconductor with p-type doping. The • and ◦ symbols represent free electrons and holes respectively. The Fermi energies of the n- and p-type samples lie very close in energy to the impurity levels arising from the donor or acceptor atoms respectively[8].

1.2.3 Photogeneration

For a working solar cell, photogeneration is a fundamental step. By photogeneration we mean the absorption of light by the active material that causes the generation of an electron and a hole. Though most relevant for photovoltaics, this is not the only optical process that occurs in semiconductors. The absorption (α) of light is not the only process that can occur in the interaction of light matter, the photons can be reflected (R), transmitted (T), or scattered (S). Expressing this concept with an equation

$$\alpha(\lambda) + T(\lambda) + R(\lambda) + S(\lambda) = 1 \tag{11}$$

To evaluate the absorbed photons considering a: light beam I_0, that passes throw a material of thickness dx, with a coefficient absorption α will be expressed by

$$\frac{dI}{dx} = -\alpha I \tag{12}$$

Considering α uniform along all the material it is possible to integrate and obtain the Lambert-Beer law

$$I(\lambda) = I_0(\lambda)e^{\alpha(\lambda)x} \tag{13}$$

The photon absorbed can increase the energy of the already present carriers, scatter or generate phonons. Considering that the effects mentioned are negligible and all the light absorbed generates a pair electron-hole the generation rate is

$$G = \alpha N_0 e^{-\alpha x} \tag{14}$$

Where N_0 is the photon flux at the surface ($m^{-2}s^{-1}$). Ideally a photovoltaic device will have this generation rate, but in the real case is necessary to take in account the recombination.

1.2.4 Recombination

With recombination, we refer to the opposite process to generation, so all the losses of carriers. Unlike generation, there are several different mechanisms, and depending on the type of material one can be dominant respect the other. There are three different types of recombination: Shockley-Read-Hall, radiative, and Auger.

1.2.4.1 Radiative

The radiative recombination is the process that is at the base of some devices as light emitting diode (LED) for example. This process is particularly present in the direct bandgap semiconductors, and the processes at the base of photoluminescence and electroluminescence. The mechanism consists in an electron in the CB recombines with a hole in the VB this cause the emission of photon with energy close to the band gap, depending on the thermal spread of the carriers along the bands. The rate of this effect for electrons is

$$U_{n,rad} = \frac{n - n_0}{\tau_{n,rad}} \tag{15}$$

Where n_0 is the number of electrons at equilibrium, where the minority carrier radiative lifetime is

$$\tau_{n,rad} = \frac{1}{B_{rad}N_a} \tag{16}$$

In an analogue way for holes

$$U_{p,rad} = \frac{p - p_0}{\tau_{p,rad}} \tag{17}$$

And

$$\tau_{p,rad} = \frac{1}{B_{rad} N_d} \tag{18}$$

1.2.4.2 Shockley-Read-Hall (SRH)

SRH is the recombination related to the defects present in the material, these defects or impurities generate trap states in the band gap. Usually, free carriers are delocalized to respect the trap states but during free path of the carriers they can meet and have an interaction. When this happens, the free carrier can be released by thermal energy for example if this is not the case then the recombination has in effect succeeded. To quantify the losses of this mechanism is necessary to consider a semiconductor with defects (N_t). The rate at which electrons are captured in this bimolecular process is given by:

$$U_{nc} = B_n n N_t (1 - f_t) \tag{19}$$

where f_t is the probability that the trap is already occupied. The coefficient B_n that expressed the probability of capture of the electron is

$$B_n = v_n \sigma_n \tag{20}$$

where v_n is the thermal velocity of the electron and σ_n is the capture cross-section of the trap for electrons. For holes is possible to write a similar equation:

$$U_{pc} = B_p n N_t (1 - f_t) \tag{21}$$

And also

$$B_p = v_p \sigma_p \tag{22}$$

It is useful to define a lifetime for electron capture by the trap

$$\tau_{n,SRH} = \frac{1}{B_n N_t} \tag{23}$$

And for holes

$$\tau_{p,SRH} = \frac{1}{B_p N_t} \tag{24}$$

Another kind of defects present in non-ideal materials are the surface and grain boundary recombination.

1.2.4.3 Surface and grain boundary

Usually, in solids a higher number of traps is located on the surface and in the grain boundaries, this is related to the fact that both are disruptions of the crystal lattice. These kinds of traps are not three-

dimensional but only two-dimensional for this reason is better to express them in density per unit area instead of per unit volume. The surface recombination velocity for holes is defined by

$$S_n = B_n N_s \tag{25}$$

With a lifetime

$$\tau_{n,S} = \frac{W}{2S_{surf}} \tag{26}$$

Where W is the thickness of the absorbing material and S_{surf} is the surface recombination velocity

Meanwhile for holes

$$S_p = B_p N_s \tag{27}$$

and

$$\tau_{p,S} = \frac{W}{2S_{surf}} \tag{28}$$

Another nonradiative recombination is the Auger recombination.

1.2.4.4 Auger

In Auger recombination consists in the collision between three carriers. The first collision causes a radiative recombination, but the energy released in this way is given to another carrier. The absorption of this radiation will increase the kinetic energy of the carrier, then this excess of energy will release thermally. The three carriers can be an electron and two holes, or a hole and two electrons are involved. The rate is proportional to the densities of all three carriers, it will be for two-electron and one hole is

$$U_{Aug} = A_p(n^2 p - n_0^2 p_0) \tag{29}$$

For two holes and one electron will be

$$U_{Aug} = A_n(p^2 n - p_0^2 n_0) \tag{30}$$

Where A_p or A_n are Auger coefficients. This process is important where dependence is low so for p-type doped material the electron lifetime is

$$\tau_{n,Aug} = \frac{1}{A_n N_a^2} \tag{31}$$

Similarly, the hole lifetime in n-type material is

$$\tau_{p,Aug} = \frac{1}{A_p N_d^2} \tag{32}$$

Auger recombination can also occur via a trap state. In that case, the lifetime will be for p-type

$$\tau_{n,Aug} = \frac{1}{N_t N_a} \tag{33}$$

Similarly, the hole lifetime in n-type material is

$$\tau_{p,\ Aug} = \frac{1}{N_t N_d} \tag{34}$$

Auger events conserve energy but also momentum for this reason this effect can occur in indirect bandgap usually is the dominant mechanism in this kind of material.

To evaluate the lifetime of a material the reciprocal is given by the sum of the reciprocal mechanism

$$\frac{1}{\tau_{bulk}} = \frac{1}{\tau_{Auger}} + \frac{1}{\tau_{rad}} + \frac{1}{\tau_{SRH}} + \frac{1}{\tau_S} \tag{35}$$

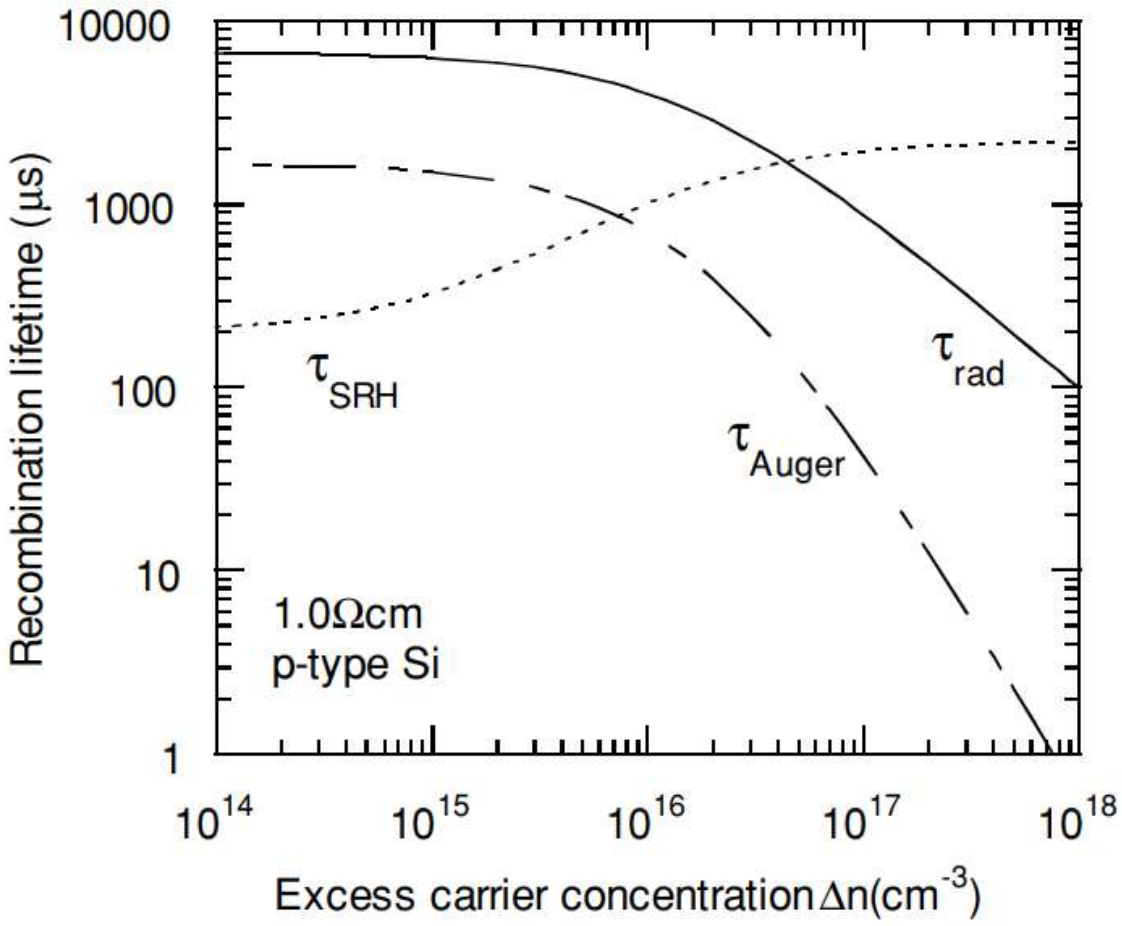

Figure 7 – Radiative, Auger and SRH recombination lifetimes for 1Ωcm p-type silicon. The radiative and Auger curves are intrinsic, whereas the SRH curve is one of many possibilities for this material[92].

1.2.5 Drift

We have considered the semiconductor at equilibrium. One feature of the material at equilibrium is that no current flows, since current should flow in the operating solar cell, the device cannot be at equilibrium. To understand the operation of a solar cell is necessary to study what happens to the semiconductor when it is no equilibrium conditions. If the intrinsic silicon is subjected to an electric field the number of electrons is equal to the number of holes and the electric current can be expressed as

$$J = -qnv_e + qpv_h \tag{36}$$

where q is the charge of the electron equal to 1.6 10^{-19} C, and v_e or v_h represents the speed at which the charges move. It is proportional to the applied electric field (up to a saturation value), in particular

$$v = -\mu E \tag{37}$$

Putting together the two equations we have that the current density is expressed as

$$J = (-qn\mu_e + qp\mu_h)E = \sigma E \tag{38}$$

where it is seen that the overall conductivity σ depends on the sum of the mobility of electrons and holes (less than that of the electron).

1.2.6 Diffusion

When there is a non-uniform concentration of doping atoms inside the semiconductor the carriers distribute uniformly in the materials. So the concentration of the dopant equals the number of the distribution of electrons or holes, since they act as free carriers. When there is no uniform distribution of the carriers a movement of the carriers occur from the regions with higher concentration to the regions with lower concentration. The different distribution of carriers in solar cells may occur relate to the directional absorption of the light. The movement of carrier aforementioned has an important consequence that is the generation of a current called diffusion current [A/m^2]. Since these carriers are "free" is possible to treat them as a gas since the distance between them is large so there aren't interatomic interactions between them. The current generated in this way is proportional to the derivative of the concentration of the charges, for electrons

$$J = (-qn\mu_e + qp\mu_h)E = \sigma E \tag{39}$$

$$J_{n,diff} = qD_n \frac{dn}{dx}$$

where q is the charge of the carriers and the constant D_n [cm^2/s] is called the electron diffusion coefficient. In a similar way for holes is

$$J = (-qn\mu_e + qp\mu_h)E = \sigma E \tag{40}$$

$$J_{p,diff} = -qD_p \frac{dp}{dx}$$

This current, not associated with an applied voltage, is negative and moves towards the zone with the highest concentration of dopant. For holes and electrons, the current has the same direction due to the opposite sign for electrons respect the motion. The diffusion coefficient is an indicator of the ability of carriers to spread in the lattice in the presence of a concentration gradient different from zero. The diffusion coefficient is intuitively linked to mobility according to the Einstein relations for electrons

$$J = (-qn\mu_e + qp\mu_h)E = \sigma E \tag{41}$$

$$\mu_n = \frac{qD_n}{k_B T}$$

Where q is the charge of the carrier, k_B is the Boltzmann constant and is equal to $8.62 \cdot 10^{-5}$ eV/K and T is the temperature. For holes is possible to write analogue equation:

$$J = (-qn\mu_e + qp\mu_h)E = \sigma E \tag{42}$$

$$\mu_n = \frac{qD_n}{k_B T}$$

The diffusion is present when there is a gradient of carrier this is a case of a doped semiconductor, since the electron moves away from the donor atom since the surrounding regions have less electrons. This effect is just locally since the move of the electron creates an opposite charge of the atom that creates an electric field and this recall the carrier. These two effects are to minimize the electrostatic potential and statistical potential, can be presented as a dynamic equilibrium, it is a stationary condition. As mention before the currents are present only locally so macroscopically considering the entire system the total current is zero. In formula at certain temperature without external stress for electrons is given by

$$J = (-qn\mu_e + qp\mu_h)E = \sigma E \tag{43}$$

$$J_n = J_{n,diff} + J_{n,drift} = qD_n \frac{dn}{dx} + q\mu_n nE = 0$$

For holes

$$J = (-qn\mu_e + qp\mu_h)E = \sigma E \tag{44}$$

$$J_p = J_{p,diff} + J_{p,drift} = -qD_p \frac{dp}{dx} + q\mu_p pE = 0$$

Only if the semiconductor is not in thermodynamic equilibrium can the total current be different from zero. These cases can be external light or electric fields or with a certain device configuration like p-n junction. In this case there are two different regions where the carriers gradients are very different, this case will be better explained next section.

1.2.7 PN junction

After the generation of a pair electron-hole, the second step to having a photoelectric generation is the charge separation. There are different mechanisms, but one of the most used is the p-n junction. It is possible to create this junction by doping different regions of the same material. Taking silicon as an example doping one side p and the other side n will create a pn junction. This junction acts as a selective barrier to charge carrier flow, in fact close to the interface between the p and the n the charges are removed due to the presence of the ions left by the free carriers, since these charges cannot move and they have opposite side along the interface an electric field form. In this region, the free carriers are quickly swept for this reason it is also called "depletion zone". The minority carrier lifetime is the last step for the photovoltaic device, it is necessary that the carriers reach the contacts after crossing the depletion zone to have electric power. All the recombination mechanisms mentioned in the previous section play a role for pn junctions SRH recombination is the dominant mechanism. The electric field causes also the potential V_{bi} and it depends onthe difference in the work function of the n and p regions

$$V_{bi} = \frac{1}{q}\left(\Phi_n - \Phi_p\right) \tag{45}$$

This difference is equal to the shift in the Fermi levels so the previous equation is given by

$$V_{bi} = \frac{1}{q}\Big((E_i - E_F)|_{p\ side} - (E_i - E_F)|_{n\ side}\Big) \tag{46}$$

Substituting it is possible to obtain

$$V_{bi} = \frac{k_B T}{q} \ln\left(\frac{N_d N_a}{n_i^2}\right) \tag{47}$$

The Fermi level shifts if an external electrical bias is applied so the resulting potential will be

$$V_J = V_{bi} - V \tag{48}$$

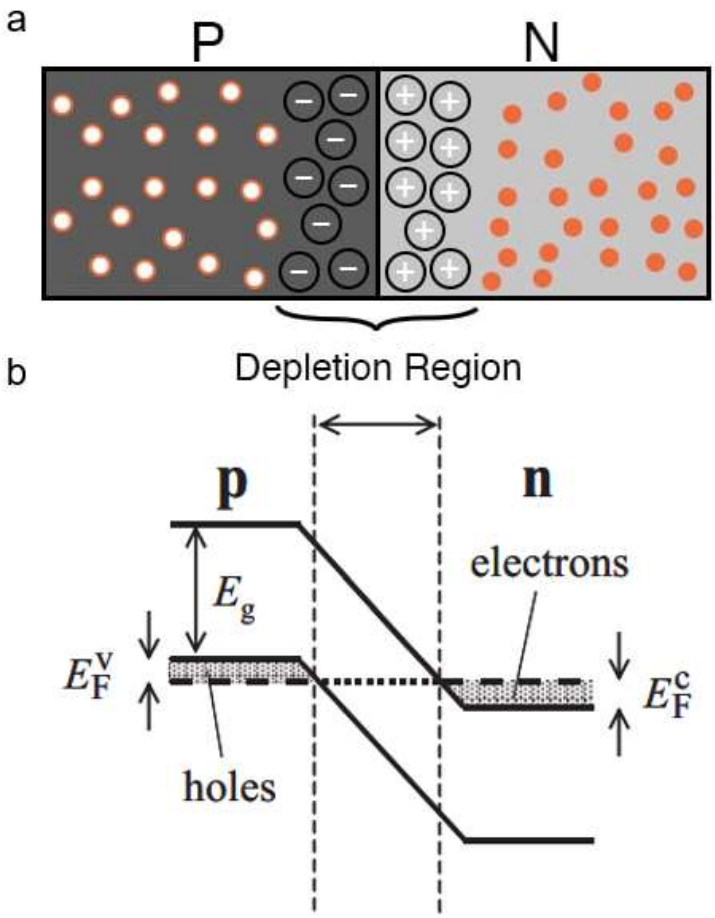

Figure 8 – a) Schematic representation of the pn junction. b) band profile of the pn junction at equilibrium[8].

It is possible to apply an external voltage V>0 called forward bias or V<0 called reverse bias. In this last case the electric field increases so the barrier in the depletion zone increases so the probability of a carrier crossing the zone is lower. This means that the overall current diffusion is lower since the minority carriers are fewer. Vice versa with forward bias the potential energy gap is lower for this reason more major carriers can cross the depletion zone allowing a higher diffusion current.

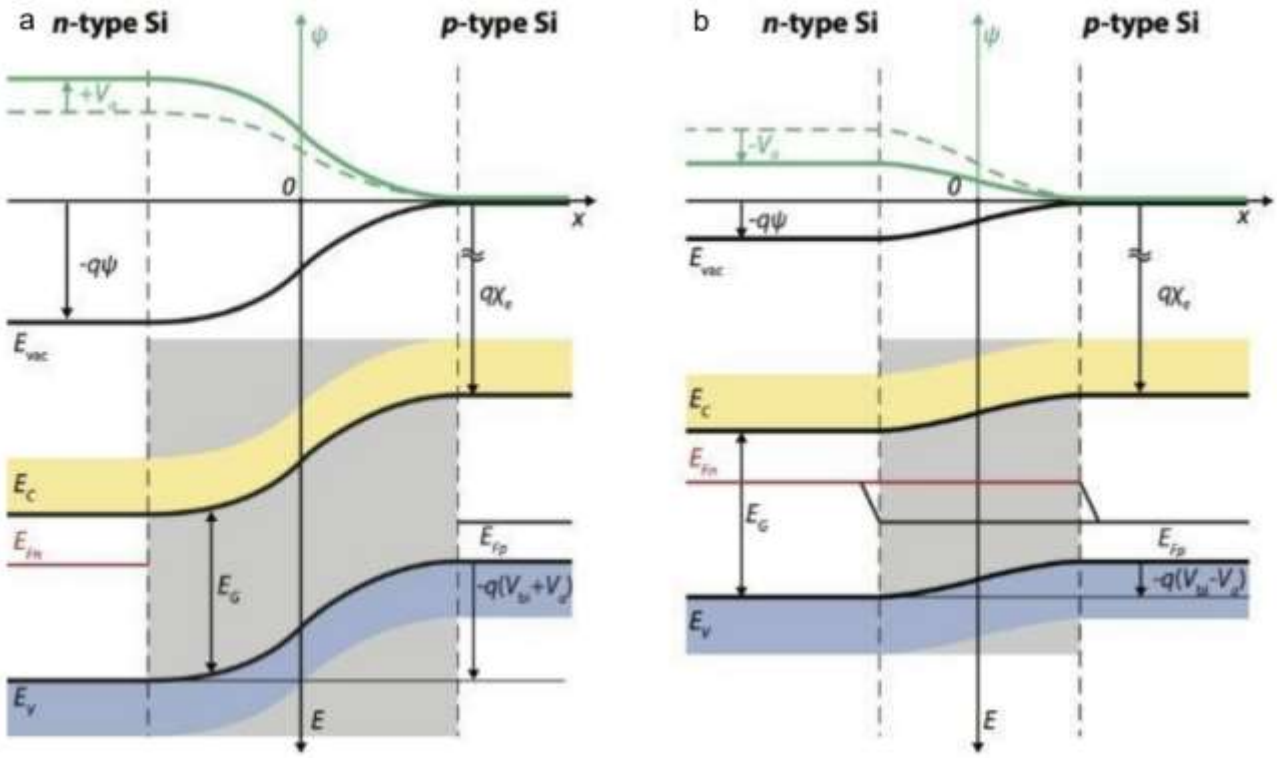

Figure 9 – Energy band diagram and electrostatic-potential (in green) of a p-n junction under (a) reverse bias and (b) forward bias conditions[9].

To evaluate these different cases is possible to use the equation of the drift-diffusion and the minority carrier density to determine the current density

$$J = J_0\left(e^{\frac{qV}{k_BT}} - 1\right) \tag{49}$$

Where

$$J_0 = \frac{J_0}{A} = \frac{qD_p p_{n0}}{L_p} + \frac{qD_n p_{p0}}{L_n} \tag{50}$$

The equation it is also used for describing the ideal diodes. For a more general diode the ideality factor "n" is used. The equation became

$$J = J_0\left(e^{\frac{qV}{nk_BT}} - 1\right) \tag{51}$$

1.3 Solar cell operation

A solar cell, as already mentioned, is an electronic device that converts light into electricity. The light of the Sun produces a positive and a negative charge that will be separated and then collected. All these processes will produce a current and a voltage and so an electric power. To have a commercial competitive solar panel is necessary to have a material that absorbs all the sunlight, and most of the carriers move to an external circuit. To evaluate the efficiency of a solar device, exist different figures of merit one of them is the quantum efficiency.

1.3.1 Quantum efficiency

The "quantum efficiency" (QE) indicates the amount of current that the device will produce divided by the different photon a certain wavelength λ or energy E. It can be divided in the "external" quantum efficiency (EQE) this is the number of carriers collected dividing by incident photons so are included all the optical effects as reflection scattered photons, it is also known as “incident photon to converted electron” (IPCE). Another type of QE is the "internal" quantum efficiency (IQE) and it refers to ratio of the carriers and the absorbed photons. By measuring all the optical effects of the device studied, the external quantum efficiency curve can be corrected to obtain the internal quantum efficiency curve. The ideal photovoltaic device absorbs all the incident photons and every carrier produced in this way will be collected, graphically it will result in a perfect square where the edge is given by the band gap or the incident light.

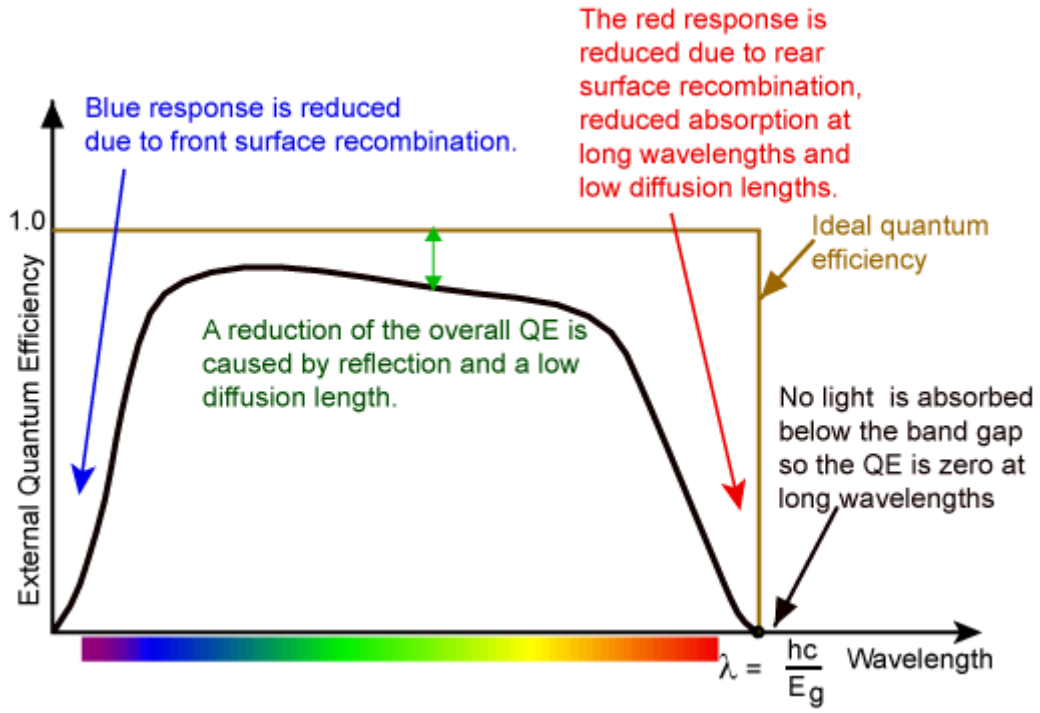

Figure 10 – The quantum efficiency of a solar cell, highlighting the characteristic losses in each region[93].

In the real case there are some losses as the recombination effects that will alterate the ideal square. Depending on the shape of the curve is possible to understand which recombination mechanism or the concomitance of more than one effect reduce the efficiency of the device. As presented in figure 10 is possible to observe that the reduction at short wavelength is related to surface recombinations, meanwhile at long wavelength the losses are more related to diffusion lengths. It is possible to evaluate the theoretical current with the equation

$$J_{SC}(\lambda) = \int_{\lambda_1}^{\lambda_2} EQE(\lambda) AM1.5(\lambda)\, q d\lambda \tag{52}$$

It is also possible determine the Eg of a material with this measure, but unfortunately this measure is quite long respect the so-called JV measure.

1.3.2 JV curve

The diode equation is the curve of a solar device without any light applied. The only process that occurs is spontaneous emission. When a solar device is under illumination generates carriers that will produce a current (J_L) so the diode equation will be

$$J = J_L - J_{dark} = J_L - J_0 \left[e^{\frac{qV}{nkT}} - 1 \right] \tag{53}$$

Graphically the dark JV will be shifted according to the current generated so related to the intensity of light used

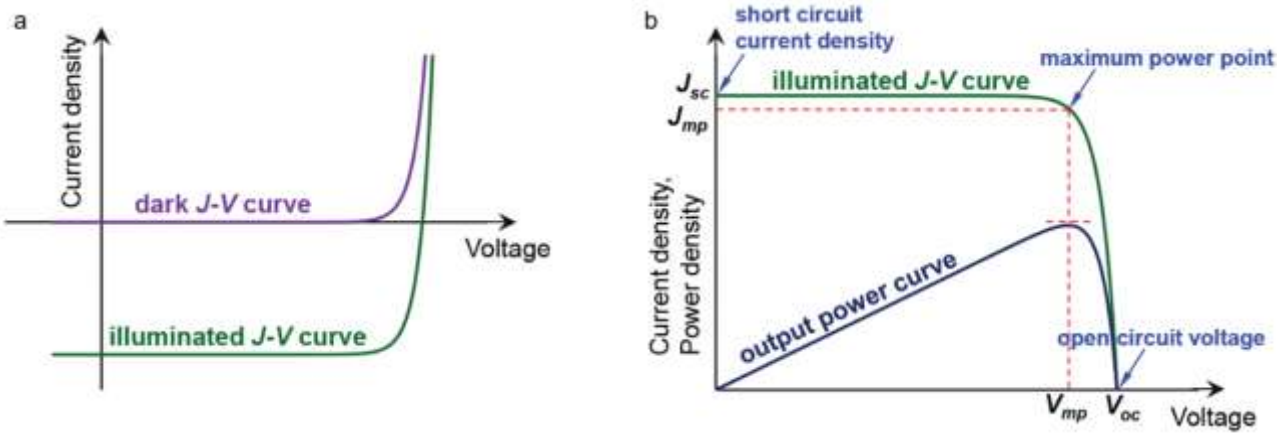

Figure 11 – a) Dark and illuminated J–V curves of a solar cell; b) a typical representation of an illuminated J–V curve as well as output power density curve as a function of voltage, including indication of the short-circuit point (0, Jsc), the open-circuit point (Voc, 0), as well as the maximum power point (Vmp , Jmp)[10].

From a simple manipulation is possible to obtain from the JV curve the PV curve (power versus voltage) from this graph is possible to find a maximum (P_{MP}) that is given by

$$P_{MP} = J_{MP}V_{MP} \tag{54}$$

P_{MP} is also known as a maximum power point (MPP). From the JV curve is possible to identify some important points, the first presented is at y=0 it is called short-circuit current (J_{SC}).

We identify the short-circuit current as the current through the solar cell when it is short circuited (V=0). The J_{SC} depends on the properties used as active material (optical properties, minority-carrier collection probability, etc.). The characteristic of the device like the area (related to the design of the solar cell) and the number of photons (incident light). As an approximation is possible to interchange I_L and I_{SC}. Usually, the most critical parameters to have a high current are the surface passivation and the diffusion length, for this reason, one of the first steps for an efficient solar cell is the optimization of the active material. The short-circuit density is given by the formula

$$J_{SC} = qG(L_n + L_p) \tag{55}$$

Where q is the charge of the carriers, G is the generation rate, and L_n and L_p are the diffusion lengths of electron and holes.

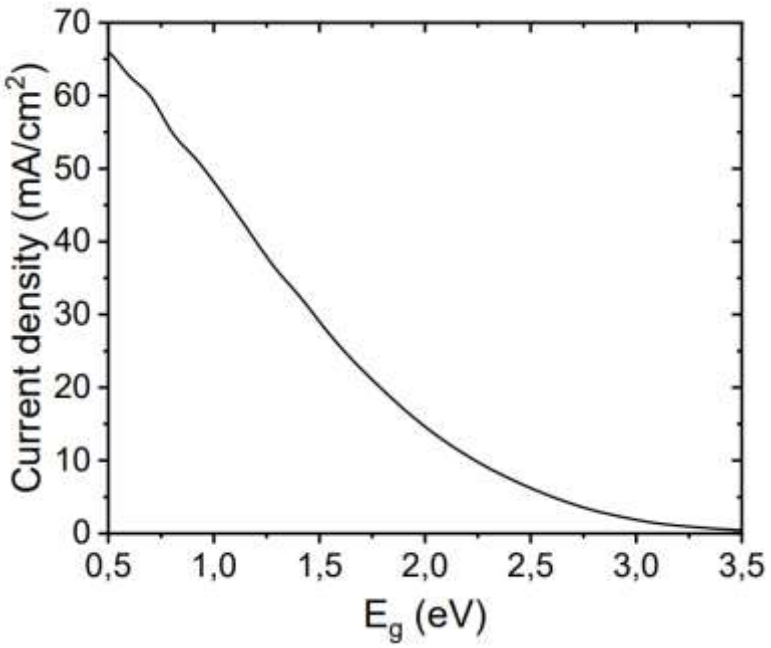

Figure 12 – Current density limit depending on the bandgap of the active material used, under AM0 and AM1.5

It can be useful to calculate the maximum value that a device can reach. It is possible to obtain the maximum current depending on the band gap of the active material. Another point that is possible to identify from the JV curve is the open-circuit voltage (V_{OC}) that is located at x=0.

The V_{OC} occurs at the current equal to zero and it is the maximum voltage that the device achieves. The open-circuit voltage is shown on the JV curve below. Changing the equation of the ideal diode:

$$V = \frac{nkT}{q} ln\left(\frac{J_{SC} - J}{J_0}\right) \tag{56}$$

That in case of open circuit voltage became

$$V_{OC} = \frac{nkT}{q} ln\left(\frac{J_{SC}}{J_0} + 1\right) \tag{57}$$

Where J_{SC} decreases exponentially with increasing bandgap, is not the case of the open-circuit voltage that increases linearly with the band gap (in the ideal case).

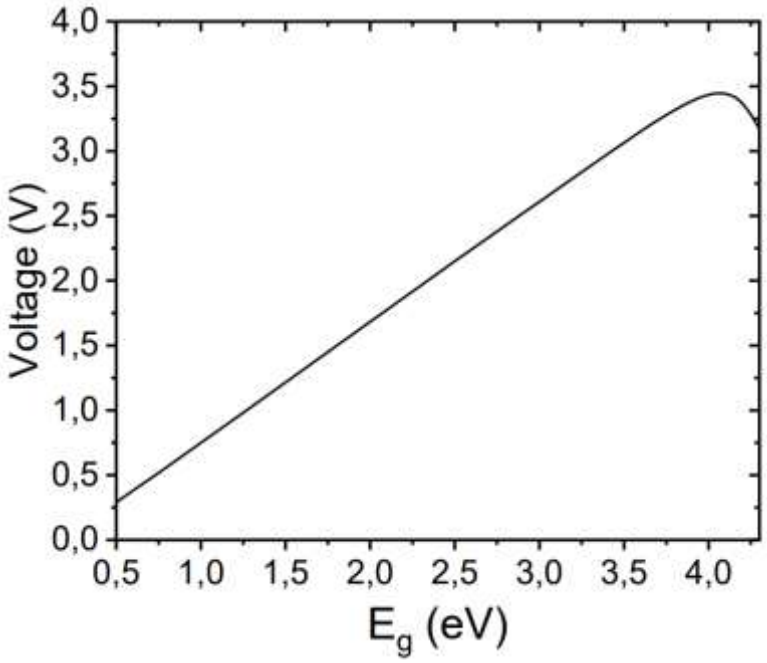

Figure 13 – Voltage limit depending on the bandgap of the active material used

In a solar cell, J_{SC} and V_{OC} are the maximum current and voltage of the device ideally the JV curve should be a perfect square. The ratio between this ideal case and the real case in which are present losses is called fill factor (FF).

The real case of a working solar cell is the maximum power point so the ratio between the real case and the ideal case that identify the FF is given by

$$FF = \frac{P_{MP}}{J_{SC}V_{OC}} = \frac{J_{MP}V_{MP}}{J_{SC}V_{OC}} \tag{58}$$

Since the ideal case is a square, higher FF corresponds to a more "squared" JV curve. The FF can improve depending on the quality of the fabrication of the device but is also intrinsic to the materials as V_{OC} higher band gap higher FF is possible to achieve.

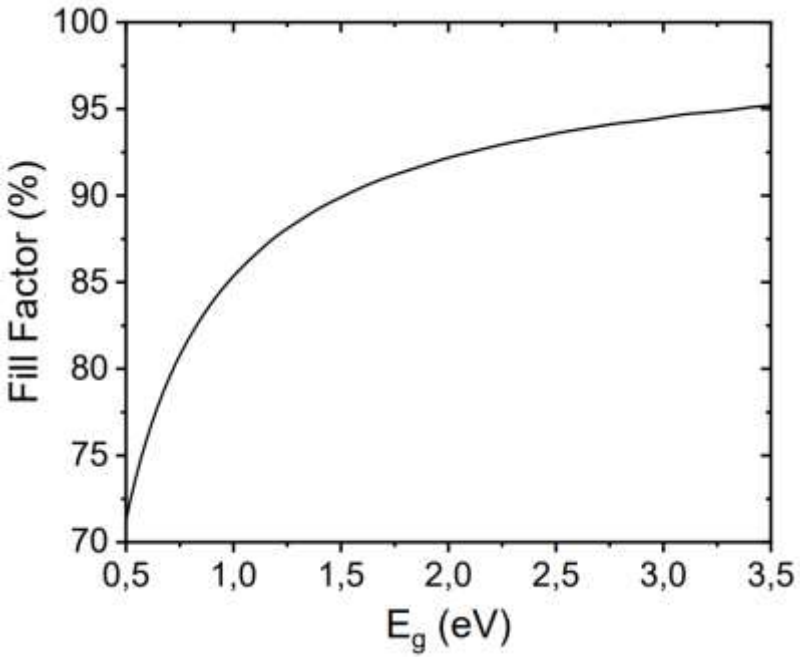

Figure 14 – Fill factor limit depending on the bandgap of the active material used

The efficiency (η) or power conversion efficiency (PCE) of a solar cell is defined as the ratio of the power density produced and the power density coming from the incident light, also using the equation (58) is possible to have

$$PCE = \eta = \frac{P_{MP}}{P_{in}} = \frac{V_{OC}J_{SC}FF}{P_{in}} \tag{59}$$

This is one of the most used parameters to evaluate different solar cell. As shown in the equation the performance of solar cells depends on the incident light for this reason is important knowing the spectrum and the intensity of the light used. As mentioned in the previous section the incoming radiation coming from the Sun is the AM0 and it is called AM1.5 after passing through the atmosphere. From the PCE vs band gap is possible identify the semiconductors that are ideal to achieve high efficiencies.

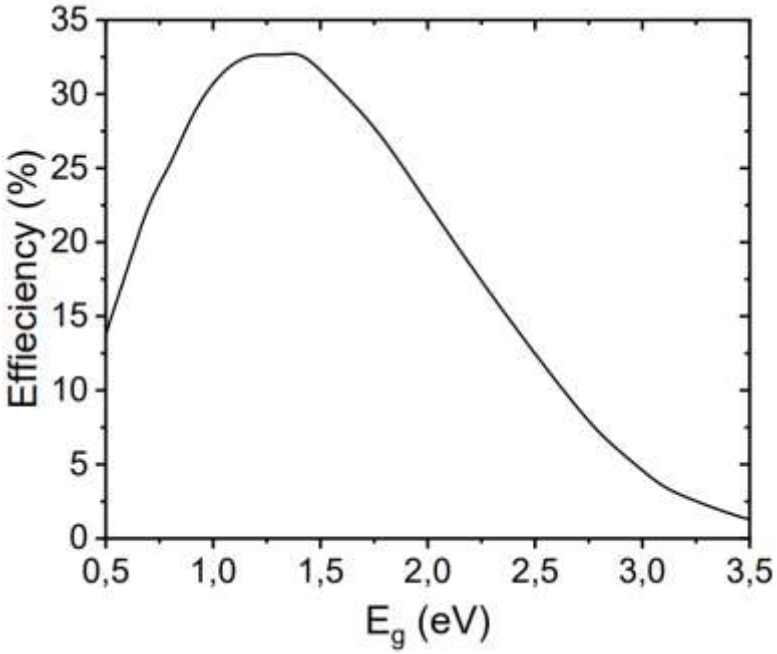

Figure 15 – Efficiency limit depending on the bandgap of the active material used.

1.3.3 Parasitic resistances

In real devices, the power is dissipated through the resistance present in the solar cells. It is possible to identify two characteristic resistances in solar cells in series (R_S) and in parallel also called shunt resistance (R_{SH}).

Series resistances are caused by three factors: firstly, the movement of current through the device; secondly, the contact resistance between the metal contact and the active material; and finally, the resistance of the metal contacts. The R_s reduces the fill factor and modify the JV close to the V_{oc} increasing predominantly the slope in that part of the curve. When this resistance achieves high values is possible to observe a change in the whole JV and a drop in the short-circuit current. Considering this resistance, the equation of the ideal diode became:

$$J = J_L - J_0 \left[exp\left(\frac{q(V + JR_s)}{nkT}\right) - 1 \right] \tag{60}$$

Ideally, this resistance should be as low as possible but of course, is always present since it is not possible to have a resistance equal to zero unless the use of superconductors which no one has done in photovoltaic devices.

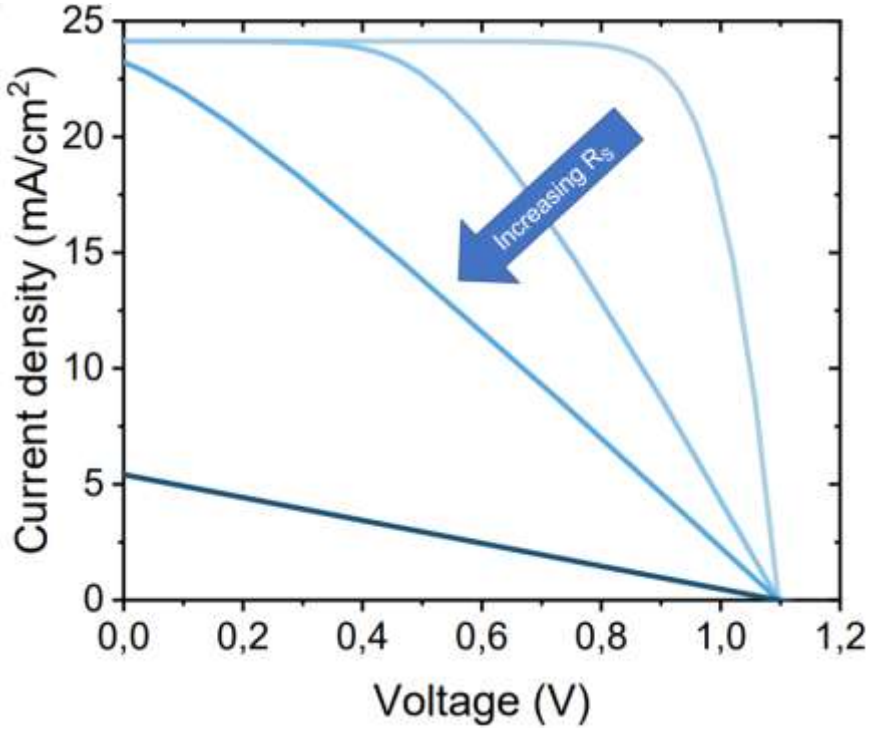

Figure 16 – Effects of the series resistance on the J-V characteristic.

The shunt resistance, R_{SH}, is typically due to defects that happened during the fabrication. This resistance is attributed to leakage of current through the cell, it can happen around the edges or between contacts of different polarity. Since it is related to a preferential pathway for carriers higher the R_{SH} is better it is for the solar cell. This resistance affects the JV close to the J_{SC} changing the slope of the curve in this region lower and when the R_{SH} is remarkably low the V_{OC} get lower. The diode equation became:

$$J = J_L - J_0 \left[exp\left(\frac{qV}{nkT}\right) - 1 \right] - \frac{V}{R_{SH}} \tag{61}$$

Graphically

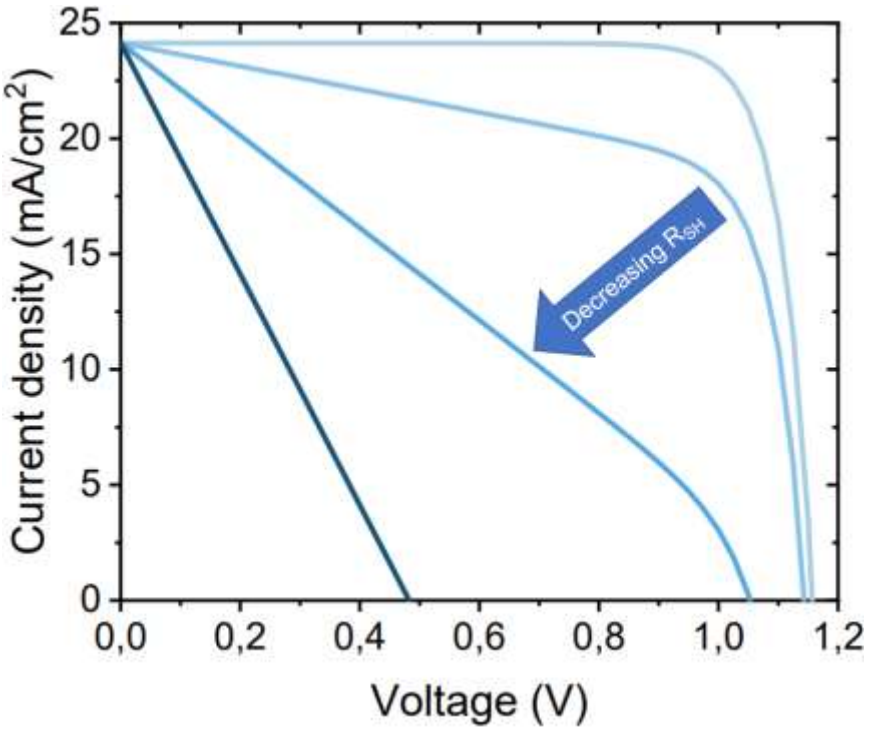

Figure 17 – Effects of the shunt resistance on the J-V characteristic.

In the presence of both series and shunt resistances, the JV curve of the solar cell is given by

$$J = J_L - J_0 \left[exp\left(\frac{q(V + JR_s)}{nkT}\right) - 1 \right] - \frac{V + JR_s}{R_{SH}} \tag{62}$$

When these resistances have low effects they modify just the FF, they can be evaluated graphically from the slope of the JV curve.

1.3.4 Solar cell Technology

The golden triangle in solar energy is a way to represent the ideal conditions for the commercialization of solar technology. At the vertices of the triangle, there are low costs, high efficiency, and high stability. Nowadays silicon is dominating the solar market. Even though silicon solar cells made are efficient and stable, unfortunately, this technology has a high startup manufacturing cost and severe carbon emission. The purification of this material requires high temperature so a huge consumption of energy. The purpose of innovative photovoltaic technologies is to match the global demand with low-cost technology that is adaptable to the global market. The cost is not only the cost of the materials but also the fabrication processes, moreover, is necessary to take into consideration the environmental impact and the possibility of recycling or the cost of the disposal of the device. In this contest, several emerging photovoltaic technologies emerged as dye-sensitized cells (DSSC), organic photovoltaics (OPV), inorganic cells (CZTSSe), quantum dot cells (QD), and perovskite solar cells (PSC). All these technologies have low costs for the material and in the production of solar cells. From the graph efficiency vs year is possible to observe how all the

photovoltaic technologies show an improvement over the years. Perovskite observes an incredible improvement passing from almost 4% in 2010 up to more than 25% in recent years which is close to the efficiency of silicon solar cells record. No other technology observes such improvement together with the low cost of the materials and their abundance leading this technology to be the best candidate to be the game changer in solar technologies[11].

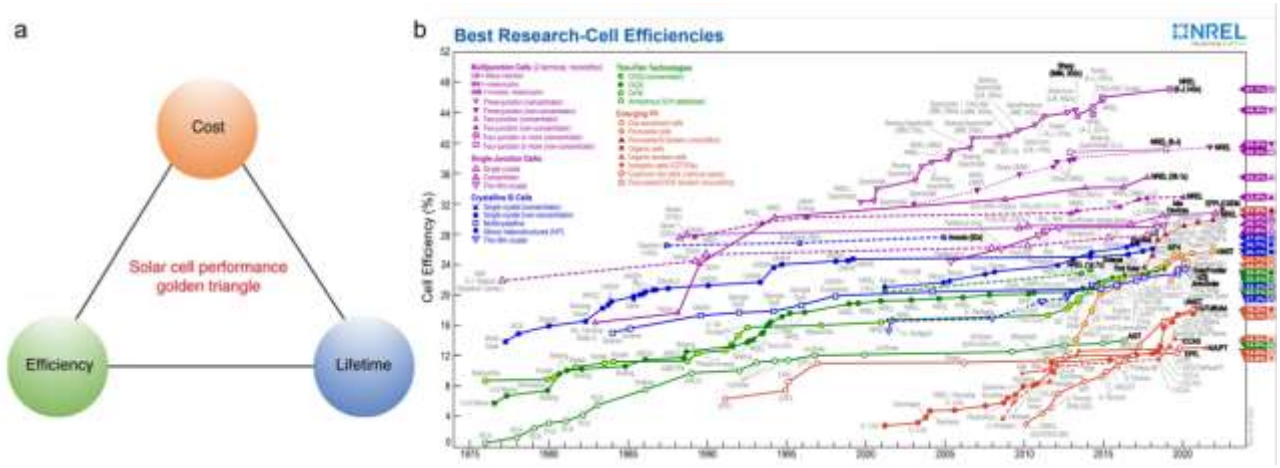

Figure 18 – a) Golden triangle of solar cells bonded with the cost, efficiency and lifetime parameters. b) Reported timeline of solar cell energy conversion efficiencies[11].

1.3.4.1 I generation

Photovoltaic technology started in April 1954 at Bell Laboratories when researchers make the first working solar cell. The device was made by single crystal silicon doped with boron and arsenic making a pn junction this kind of solar cell achieves an efficiency around 6%. The first generation of solar devices is silicon-based; the process used to produce single crystals is known as "Czochralski process". In this process, the silicon is heated at high temperatures to purify the material and form a uniform ingot single crystal. Since this process is intensively energy consuming and at that time very expensive other ways to produce cheaper material were studied multi-crystalline silicon was one solution. The impurities of solar cells made with this other category of silicon are higher and that is reflected in the PCE that were lower with respect to the single crystal. The process used to obtain multi-crystalline silicon is called casting and consists in pouring silicon and leaving it cool down. The result is a material with large grains, but more than just a single crystal so the material has lattices structure randomly oriented considering the entire crystal. In this generation of solar was considered more than the cost to push the efficiency of the devices to exploit the technology, for this reason, were considered silicon that with the band gap of 1.1eV is a good candidate for photovoltaic application according to the Shockley-Queisser limit. It used a relatively thick material to optimally absorb light, achieving high values of efficiency. Even nowadays for the single junction, Si is one of the most efficient solar cell with 26.1%, unfortunately, the thickness of the material doesn't allow the development of flexible devices, and they are fragile and expensive. GaAs is a material between the first and the second-generation solar cells since it uses thin, direct band gap material, but the cost of the material is very high for this reason

is used almost only in space fields where the cost is less relevant, meanwhile global market silicon is more competitive. This material is a III-V semiconductor despite the fabrication used can lower the prices of the panels the cost of the raw material is high since is not so abundant in the hearth[9].

1.3.4.2 II generation

The second-generation solar cells had as purpose to reduce the costs of the process and the use of materials, for this reason, is also known as thin film generation. To achieve these results the active material, require high optical absorption coefficients and advanced light trapping studying. The photoactive materials with these characteristics are Amorphous silicon, cadmium telluride, GaAs, and CIGS. The maximum photocurrent available under the irradiation AM1.5 was achieved using around 1-10% of the thickness concerning the silicon counterpart.

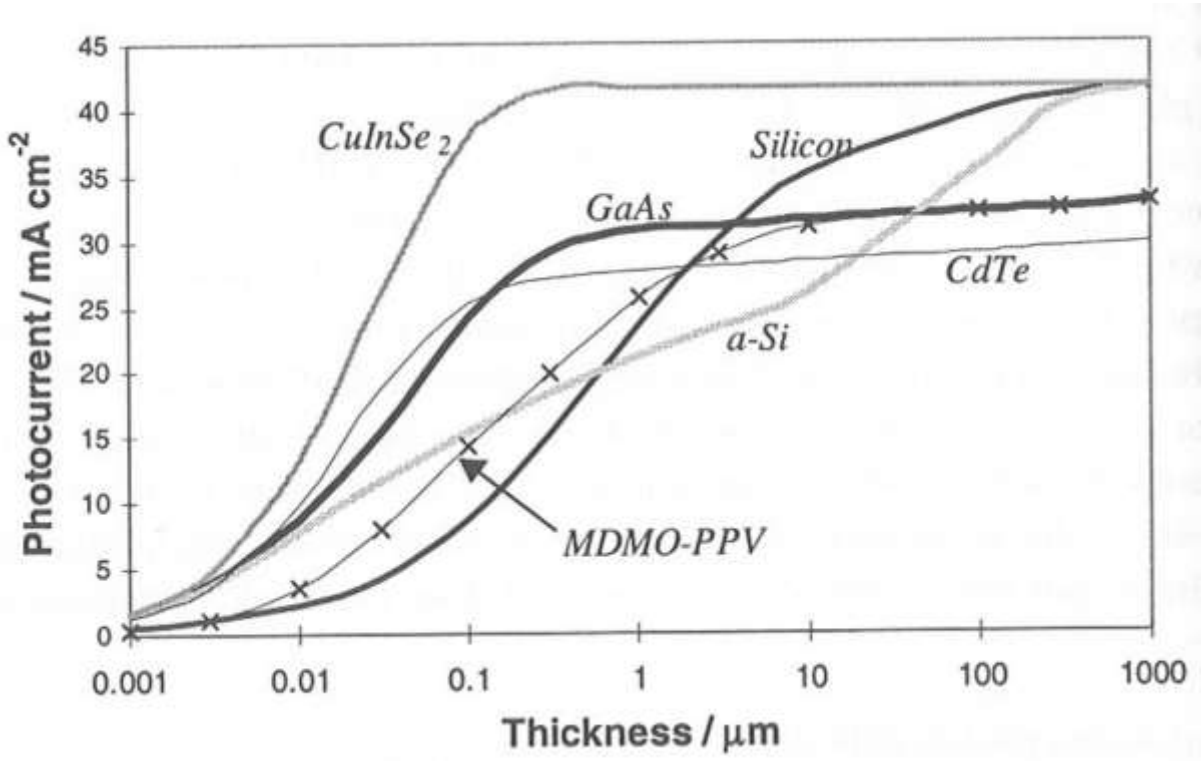

Figure 19 – Absorption spectra of photovoltaic semiconductors[12].

The use of thin layers allows the use of these devices into classic rigid substrates or flexible ones, with a reduction in the cost since the low quantities used, respect the first generation the cost is 50% less. The highest efficiencies of this generation of solar cells are around 20% which is lower than the previous generation. Another difference is that in the semiconductors used in this generation of solar cells the band gap is direct meanwhile silicon has an indirect band gap, the second generation still forms a pn junction. The amorphous silicon was studied since can use the already existing silicon technologies, the lower efficiency of these cells is related to the lower absorption with respect to the crystalline silicon, also over time these cells photodegrade. The CIGS material has a tunable band gap using varying the ratio of indium gallium it can go

from 1 eV with $CuInSe_2$ to 1.7 $CuGaSe_2$. The fabrication of these solar cells is based on physical vapor deposition (PVD) and chemical vapor deposition (CVD). The maximum temperatures required for this technique are 350°C way lower than respect single crystal silicon. CdTe band gap is 1.45eV and can be fabricated using several techniques such as electrodeposition, PVD, spray pyrolysis, or closed-space sublimation (CSS). All these techniques require a maximum temperature of 400°C. Since the purpose of this generation of solar cells is to use thin films increasing the thickness to improve the absorption of light cannot be the solution for this reason new concepts were developed to increase the light trapping. Some examples are nanostructured interfaces (moth-eye) or antireflective coatings (MgF_2). The second generation managed to achieve the goals purposed but the toxicity of the materials of CdTe and CIGS increases the cost of the recycling of the solar cell or their disposal, moreover these materials are not so abundant in the earth, so these technologies cannot be the final solutions. The purpose of the third generation is to overcome these issues with new materials and new strategies[9].

1.3.4.3 III generation

This generation of solar cells emerged to reach the benefits of the two previous generations' low-cost, thin-film abundant materials[13]. In this generation also the design of the cell changed since is no used the pn junction. The principle of these devices is to have an active material that absorbs light generating a pair electron-hole and other materials that extract the charges usually two: one for positive charges and the other one for negative charges. The emerging photovoltaics technologies are DSSC, OP, QD, and PSC. The first also known as Grätzel cells consist in an organometallic dye that absorbs the incident light then the extraction of the charges with the help of an electrolyte for the hole transport meanwhile the electron are extracted at the interface of the dye. The materials to produce these cells are oxides as titanium oxide or zinc oxide as extractor of negative charges; ruthenium complexes as dye and as hole extractor spiro-OMeTAD. These cells are not efficient (actual record around 13%) but the materials and the process to produce them are cheap. Moreover, the process of fabrication is reversible. It is possible to tune the absorption to have also semi-transparent devices and it is possible to use also for flexible technology. Unfortunately, the devices are not stable for long-period use, for this reason, are still under investigation. The OP is characterized by the active material that is organic materials. It is present as a donor and an acceptor they can be a bilayer heterostructure or not (bulk heterostructure), the record achieves for this category of the best cell achieved 18.2%. The active material doesn't generate a proper pair electron-hole but rather forms excitons (usually in the donor material) and separates in the acceptor materials forming the positive and negative charge that then is collected by the cathode and the anode. This technology is cheap and can use technology solution processes like inject printing, and blade coating; adaptable can make flexible and semitransparent devices but suffers from stability problems, so commercialization is still a challenge. The quantum dot cells consist of the use of nanocrystals as active materials of the solar cells. The chemical properties of these nanomaterials can be tuned by using different materials or changing the shape and the size of the nanoparticles, usually,

these materials absorb long wavelengths. The fabrication cost of these materials is low, and the synthesis is relatively easy and cheap since it is possible to use wet-chemistry methods. The record efficiency for these devices is 18.1%. The third generation includes improvement strategies to overcome the physical limits of the solar cells. To overcome the Shickley-Queisser limit the strategy used is to build a tandem solar cell. These kinds of devices consist in build a multi-junction, which means using two or more pn junctions or two or more materials that absorb different ranges in the visible. This strategy increases the efficiency limit from 31% to more than 40% using two materials and up to 68.2% for an infinite stack of solar cells. The actual record with a three-junction solar cell is 39.5%. The last emerging cells are the PSC, which this was intensely studied in recent years. These cells use perovskite as active material, it reached high efficiencies in only one decade almost achieving the silicon-based cells the actual record is 25.7%. The material cost is low, and it is abundant on the earth's surface. The manufacture is also cheap since it is possible to deposit with different techniques for example solution process (blade coater, inkjet printing) but also with other techniques such as evaporation. The tunable band gap allows using this material for single junction, tandem, semi-transparent, or flexible solar cells. Perovskites are the best candidate for the solar revolution the issue that has to be solved before commercialization is long-term stability.

1.4 Perovskite

PSCs are the most promising emerging solar cells technology; the name of the material was given by Gustav Rose in 1839 that discovered the first mineral with the perovskite configuration. Indeed, the name is in honor of the Russian mineralogist Lev Perovski. The first discovered perovskite is calcium titanate ($CaTiO_3$). This material reached the attention for photovoltaic application only after many years when substituting the cations with an organic part and an inorganic making the so-called hybrid halide perovskite, that have interesting properties.

1.4.1 Properties

The hybrid halide perovskite, also called 3D perovskite has the crystal structure ABX_3, where A is occupied by small cations methylammonium (MA^+) and formamidinium (FA^+) that are organic molecules or Cs^+ (inorganic); the B site is occupied by a metal cation Pb or Sn; the X site is occupied by halide atoms I, Br or Cl. This material has good optoelectronic properties for photovoltaic applications as tunable band gap, long carrier lifetime, and low recombination rates. The first hybrid perovskite was $MAPbI_3$, but $FAPbI_3$ has a better band gap (around 1.4eV) for solar cells, so it is possible to make all-inorganic solar cells that still have a perovskite crystal structure like $CsPbI_3$. Despite it’s possible to use different cations and still preserve perovskite crystal structure it is necessary to take into consideration the Goldschmidt rule given by

$$t = \frac{r_A + r_X}{\sqrt{2}(r_B r_X)} \tag{63}$$

Where r_A, r_B and r_C are the ionic radii of A, B, and X sites respectively. This tolerance factor should be between 0.8 and 1 otherwise the perovskite may not form or be unstable. From the previous example, only $MAPbI_3$ is in this gap and is more stable with respect to the other two perovskites: $FAPbI_3$ has a tolerance factor higher than 1, and $CsPbI_3$ lower than 0.8. Another factor to take into consideration is the octahedral factor μ given by

$$\mu = \frac{R_B}{R_X} \tag{64}$$

To have the formation of the characteristic octahedra at the base of perovskite crystalline structure $0.44<\mu<0.90$. To improve the properties and the stability of the material one strategy is to use different atoms, molecules, or a mix of them. For example, $FAPbI_3$ as mentioned above has an ideal band gap for PV application but is unstable, $CsPbBr_3$ instead demonstrates to have good thermal stability but doesn't have the ideal band (1.73eV) gap for photovoltaic application. Moreover, is possible to tune the bandgap using changing the ratio of the cations with this strategy is also possible to use perovskite also for other applications like tandem solar even still using just perovskites (one perovskite will have a large wide bandgap, and the other low bandgap)[14,15].

1.4.2 2D Perovskites

In recent years there has been significantly used in the so-called 2D perovskites in the photovoltaic devices based on perovskite. This family of perovskites has the structure formula R_2PbX_4 where R is a large organic also called spacer that substitutes the small molecules located in the A site. The optoelectronic properties of 2D perovskites are not ideal for photovoltaic application due to the wide bandgap and the directional mobility that can obstacle the charge extraction. On the other side, this material is more stable thanks to the large organic molecules that protect the perovskite. The scientific community tried to mix these two families of perovskite to have the properties from both materials, ideally and efficient (3D perovskite) and stable (2D perovskite) PSC. The strategies used are like the ones used in OP, build a heterostructure bulk or bilayer. In the first case a quasi 2D perovskite is formed according to the precursors used it have the general formula $R_2A_{n-1}Pb_nX_{3n+1}$ with n=1 a pure 2D perovskite is formed meanwhile with n=∞ a pure 3D perovskite is formed. According with the increase of n the efficiencies increase but the stability decrease. The second method consists in the deposition of a 3D layer and, usually, on top a thinner layer of 2D perovskite. These demonstrate to be a good strategy to obtain stable and highly efficient devices[16,17].

1.4.3 Degradation of perovskite

The major problem for the PSC to commercialization is the long-term stability. Perovskite in presence of humidity, oxygen, UV and thermal stress suffer degradation. The moisture penetrates in the crystal structures and the reaction that happens for $MAPbI_3$ is

$$4CH_3NH_3PbI_3 \overset{H_2O}{\Longleftrightarrow} 4CH_3NH_3 \cdot H_2O \overset{H_2O}{\Longleftrightarrow} (CH_3NH_3)_4PbI_6 \cdot 2H_2O + 3PbI_2 \quad (65)$$

Oxygen reaction is

$$4CH_3NH_3PbI_3 \overset{O_2}{\Leftrightarrow} 4CH_3NH_2 + 4HI \overset{O_2}{\Leftrightarrow} 4CH_3NH_2 + 2H_2O + 2I_2 \quad (66)$$

As is possible observe in the last case water is produced this cause the first reaction favoring the degradation of the cell. Also temperature increase the speed of the reactions

$$PbI_3 \overset{Heat}{\Longleftrightarrow} 4CH_3NH_2 + 4HI + 4PbI_2 \quad (67)$$

A similar reaction happens in presence of UV light especially for $MAPbI_3$ that is more sensitive to light respect other perovskites such as $FAPbI_3$. It is important to underline that these factors per se don't cause the degradation of the perovskite in short time is the concomitance of them that increase the rate of degradation.

To solve the degradation issue there are two strategies, increase the stability through intrinsic methods or with extrinsic method. The first method consists in the use of alternative molecules that stabilize the crystal structure in this way the crystal doesn't degrade for the outer agents. Using mixing mix cation for the perovskite is an example of intrinsic method as the use of 2D perovskite. Other examples are the use of polymers, salts that increase the stability of the devices. The second method consists in seal the solar cell with protective layers that don't allow the access to moisture oxygen. As said before it is not necessary to avoid all the degradation factors presented but it is sufficient to exclude some of them to increase the stability of the device. Some examples of this method are flexible compounds as several polymers. Or it is possible to use a more similar method to the one used for silicon-based devices the encapsulated the panel between to rigid glasses like materials[18].

1.4.4 Perovskite Solar Cell

The typical architecture of PSC is a thin film of perovskite sandwiched between two extraction layers, depending on the position of these two layers is possible to distinguish two typologies of PSC nip and pin. Following the direction of the incident light in the device the so-called nip has first a transparent conductive oxide (TCO) electron transport layer (ETL), the perovskite, then a hole transport layer (HTL), and finally the metal contact (the most used are silver and gold). In the pin structure the order of ETL and HTL is switched so the materials present are TCO, HTL, perovskite, ETL and metal contact. Each architecture needs different

material since the requirements are different. As TCO for both structures the most used are indium tin oxide (ITO) and fluoro tin oxide (FTO). For nip as ETL is used transparent oxides like TiO_2, mesoporous TiO_2 and SnO_2, for nip instead the most used is C60 or his polymer 6,6 -Phenyl C61 butyric acid methyl ester (PCBM). For HTL in nip the most used are 2,2',7,7'-Tetrakis[N,N-di(4-methoxyphenyl)amino]-9,9'-spirobifluorene (spiro-OMeTAD) and poly(triaryl amine) (PTAA) both doped for pin is also used PTAA but undoped, and self-assembly monolayers (SAM) as 2-(9H-Carbazol-9-yl)ethyl]phosphonic Acid (2PAC) or 2-(3,6-Dimethoxy-9H-carbazol-9-yl)ethyl]phosphonic Acid (MeO-2PAC). The metals contact for nip is usually gold for pin are used silver, copper and aluminum.

2 Experimental section

In this chapter are presented the experimental methods and techniques used to fabricate and characterize the samples.

2.1 Characterization

The characterization is fundamental to evaluate the fabricated devices and the reasons of different behaviors. Some of these techniques are used to characterize just the perovskite others are used to characterize the solar cell.

2.1.1 X-ray diffraction

X-ray diffraction (XRD) is a non-destructive technique that gives information about the crystal structure, this is possible thanks to the interaction between x-rays and matter. X-rays are electromagnetic radiation with a wavelength between 0.1 and 100 Å this wavelength is comparable with the interatomic distances present in the lattices. A laboratory setup is composed of four elements: a voltage generator, an x-ray tube, a sample chamber, and an x-ray detector. The x-ray tube that is used to produce the x-rays, inside which there is a tungsten cathode and an anode also called target (in the laboratory generally made up of Cu, Co, or Mo). The cathode is heated and emits electrons; these are accelerated towards the anode by a large potential (of the order of ten kV); consequently, the electronics hit the target with a remarkable speed. Beyond a certain energy threshold, the incident electrons can extract the inner electrons of the atoms of the metal anode producing a vacancy. The outermost orbital electrons fill in these vacancies generating characteristic radiation whose wavelength depends on the target, but in the range of x-rays. In the laboratory there are two strong emissions k_β and k_α, It is necessary to use a filter, usually the previous element in the periodic table of the target to have narrower emissions so in this case reduce the k_β peak. Considering the simplest case that is characterized by sheets separated by distance d they produce a constructive interference only at certain angle according to Bragg's law

$$n\lambda = 2d\sin\theta \tag{68}$$

This research used two setups the first is a Bruker Advance D8 diffractometer equipped with a 1.6-kW Cu-Anode (λ = 1.54060 Å) and an LYNXEYE_XE_T detector in 1D mode in parallel beam geometry. All scans (coupled $2\theta/\theta$, 2θ = 5° to 50°, step size 0.05°) were background-corrected using the Bruker Diffrac.Eva software. The second is a Bruker D2 X-Ray diffractometer with a copper X-Ray tube (λ = 1.5418 Å, 300 W, 30 kV) as an X-Ray generator and a Lynxeye (1D mode) detector. All measurements were conducted using a 2theta range of 4°–40°, a step size of 0.02°, and a rate of 1 step/s.

2.1.2 X-ray photoelectron spectroscopy

XPS is no destructive technique that identify the elements on the surfaces of the studied material. The setup is composed by x-ray tube already described in the previous section, a high vacuum chamber similar to the one presented in the previous section and an electron energy analyzer and an electron detector. The technique consists in irradiating the sample with x-rays this will produce electrons from the atoms also called photoelectrons. Measuring the kinetic energy is possible to identify the element that originated it. It is possible to also identify the chemical state according to the position and the intensity from the spectrum.

XPS measurements were performed in using an XR6 monochromated AlKα source (hν = 1486.6 eV) and a pass energy of 20 eV. Argon cluster ion beam etching experiments were performed using a MAGCIS ion gun using a cluster energy of 4000 eV. The etch rate at these conditions was determined to be 1.08 nm/min via reference etching experiments.

2.1.3 Ultraviolet Photoelectron Spectroscopy

UPS is like the previous spectroscopy except to the source that doesn't produce x-rays but UV light. The set-up is the same as XPS in fact they are usually coupled in the same set up the source used to produce the incident radiation is helium discharge lamp. The range of the energy studied is tens of eV so it is possible to study the molecular orbital energies. Usually through this characterization is determined the work function of the sample studied.

UPS measurements were carried out using a He discharge lamp (hν = 21.2 eV) and a pass energy of 2 eV. The etching was performed in the same way as mentioned in the previous section

2.1.4 Scanning Electron Microscopy

This SEM has the purpose of performing morphological analyzes of the surfaces of the samples, with the possibility of obtaining information also on the eventual other layers of the sample if it prepared in the proper way (cross-section). One of the fundamental differences between an electron and an optical microscope consists in the resolution, which is defined as the minimum distance between two points to be still distinguishable; it is inversely proportional to the wavelength λ of the source used. In fact, unlike the optical microscope, the SEM doesn't use photons, but an electron beam to study the sample. So according to the Abbe diffraction limit

$$d = \frac{\lambda}{2nsin\theta} \tag{69}$$

Where d is the minimum resolvable distance, λ is the wavelength used to study the sample, n is the refractive index of the medium and θ is half angle of the cone of focused light. Since electrons have a shorter wavelength than photons, the SEM has a much higher resolving power of 3.5 nm and has a maximum magnification of 300000X (the optical microscope reaches a maximum of 1000X). The electron beam, which can take energy from 2 to 50 kV, and it is generated by the thermionic effect from a heated tungsten wire. The electron beam is not fixed, but is moved in sequence on the sample, point by point, line by line, by electromagnetic lenses which modifies the trajectory of the beam. This instrument usually works with a high degree of vacuum due to the fact that the electrons must have a free path greater than the distance between source and the sample. To do this, two pumps are generally used: a rotary (to reach a vacuum level of 10^{-1} mbar) and a turbomolecular (to reach a vacuum even higher than 10^{-5} mbar). When the electron beam manages to reach the sample, three different types of signals can be detected: X-rays, secondary electrons and backscattered electrons. The backscattered electrons are obtained from the elastic interaction between the electron beam and the sample; it is observed that the number of backscattered electrons is proportional to the atomic number, Z, of the analyzed element. The elements with a higher atomic number are lighter, while those with a lower Z are darker. This analysis is used to obtain information on the crystallography, orientation, phases and microstructure of the sample under examination. The secondary electrons are always generated by the interaction between the beam and the sample, but in this case, we speak of a collision of the inelastic type, which releases one or more electrons from the outermost orbitals. This interaction can go up to 10 nm below the surface, allowing to obtain a very defined three-dimensional image. From the generated image, information on the morphology and topography of the sample can be obtained. The secondary electrons have energy below 50 eV, the number of those that can be detected by the sensor is related to the type of surface being examined. The backscattered electrons, on the other hand, have energies equal to the primary beam (20-30 keV). Moreover, from the interaction between sample and beam, X-rays can be produced. Due to the vacancies left by interactions with the innermost orbitals, the electrons of the outermost shell occupy the gaps created, releasing energy in the form of electromagnetic radiation, in the X-ray frequency region. The measurement of the wavelengths of these photons, typical for each atom, allows to determine the composition of the sample studied. The emitted electrons, if they reach the sample, must be able to return to the emission source. This must happen for two main reasons: the first is the impoverishment of the source; the second, more important, is linked to the absence of an accumulation of charge on the sample. If charge accumulated on the sample, it would no longer be observable (in fact I would have a white image). To overcome these problems, a typical solution involves the use of carbon or metal sample holders that allow the movement of the charges, avoiding accumulation. Similar materials are used for fixing the sample to the sample holder, in fact it is not always possible to use common glues as they are insulating. It is possible to study different materials using SEM, but while for conductors such as metals there are no problems, for organic materials as insulators there are the difficulties mentioned above related to charge accumulation. Even for organic materials it is possible to overcome this complication through the

metallization technique. It is also observed how, to obtain precise measurements, it is necessary to have a beam of constant intensity, otherwise the quantities of electrons involved would be altered.

Surface morphology of the perovskite films was examined using SEM (ZEISS GeminiSEM 500) operated at low voltage (1.5 keV). Cross-sectional images of the layered devices were acquired on the same setup with a 5-keV voltage for the electron beam. Or samples were studied through a field-emission scanning electron microscope (FE-SEM, Merlin) to examine the surface morphology of the films, and cross-sectional view of the devices. An electron beam accelerated to 5 kV was used with an in-lens detector.

2.1.5 UV/vis spectrometer

This instrument is used to measure the absorption, reflection, and transmittance of a sample can be solid or liquid. The setup has three sources a monochromator and a detector. First is necessary to take the first measure without anything in the light path then a second with the desired sample.

UV-vis absorption analyses were performed on a PerkinElmer Lambda 1050+ UV/VIS/NIR spectrometer on thin films deposited on glass through transmittance analysis and measuring the absorption on wavelengths ranging from 200 to 900 nm.UV-vis absorption analysis were performed on a PerkinElmer Lambda 1050+ UV/VIS/NIR spectrometer on thin films deposited on glass through transmittance analysis and measuring the absorption on wavelength ranging from 200 to 900 nm.

2.1.6 JV measurement

This characterization method is one of the most used to characterize the solar cells. it consists: illuminate a device with light that simulates the sun radition and measure the current that produce in function of the voltage. In this way is possible obtain the characteristic curve obtain the JV parameters. The setup is composed by a solar simulator that have the role to simulate the solar spectrum, and a digital multimeter to make the electrical Photovoltaic parameters (PCE, FF, JSC and VOC). Usually on the solar cells is used a shadow mask to be more precise in the active area of the sample.

In this research were performed JV measurement under 1 SUN illumination, solar spectrum AM 1.5G (LED lamp, Wavelab Sinus-70). The voltage is applied with a sourcemeter (Keithley 2401). Before taking the measurements with the solar simulator, the vertical position of the platform is adjusted through calibration with respect to a reference cell (Centronics LCE50 equipped with a KG-3 filter) to match exactly its specification for the current value under illumination. Also another setup was used under simulated AM 1.5 light with an intensity of 100 mW cm^{-2} (Abet Sun 3000 Class AAA Solar Simulator). The intensity was calibrated using a Si reference cell (NIST traceable, VLSI) and corrected by measuring the spectral mismatch between the solar spectrum, reference cell, and the spectral response of the photovoltaic device.

Cells were scanned using a Keithley 2450 source measure unit from 1.2 to 0 V and back, with a step size of 0.025 V and a dwell time of 0.1 s, after light soaking for 2 s at 1.2 V. The pixel area was 3 mm by 1.5 mm. Intensity dependence studies were performed by using neutral density filters. For transient photocurrent measurements, the light of an inorganic light-emitting diode (Thorlabs; TO-1 ¾, λ = 465 nm) was pulsed by a function generator (Agilent/Keysight 33510B; pulse length, 2 ms) and focused on the solar cell. The resulting photocurrent was measured with an oscilloscope (Picoscope 5443A) with a 50-ohm terminator placed across the oscilloscope input. MPP tracking measurements were operated in inert atmosphere (0% relative humidity, 0% H_2O, 0% O_2) with Fluxim- Lithos Lite, employing a scan rate of 10.0 mVs−1 over a range of −0.1 −1.2 V. During measurements, a shadow mask of 1.5 mm^2 area was used to cover the devices.

2.1.7 EQE

The EQE was already presented in the previous chapter, in measuring the conversion of an incident photon to an electron. The setup is composed of a light source usually a Xe lamp with a monochromator that produces a near monochromatic beam. The beam pass through a chopper, a lock-in amplifier, and then the samples; to perform a measurement is necessary to measure first a reference cell usually a calibrated diode is used, then the solar cell is studied.

EQE measurements were performed in ambient air conditions with a Cicci Research Arkeo steady-state tests module. The wavelength scan range was set between 300 and 900 nm.

2.1.8 Atomic Force Microscopy

The AFM is a scanning probe microscope, which means that there is a probe that measures a physical quantity, that depends on the distance between the tip and the sample, such as the Van der Waals forces. Therefore, the probe must "scan" the sample point by point thus allowing it to obtain information on its surface. This instrument, generally, has no chemical specificity, therefore it is necessary to already know the composition of the sample studied, it is not possible to obtain this information using this technique. There are two modes of operation of AFMs: constant signal and constant distance. In the last case, the variation of the physical quantity is measured during the scan to be able to reconstruct the surface based on the variations of this quantity (this mode is precise, but it is also easier to damage the tip). The second method consists in keeping the signal constant and therefore during the scanning the probe moves according to the surface morphology (since the physical size depends on the distance) the probe will move by replicating the surface of the sample. Generally, the probe of these microscopes is constituted by a microlight with a sharp point of nanometric dimensions (in cases where a higher resolution is required, it can reach atomic dimensions). To measure the deflection of the micro-lever, consequently of the probe, an optical lever is used. This method consists in hitting the back of the top with a laser and the reflecting goes to a photodetector. The detector is composed of four photodiodes coupled differentially so that the movements of the micro lift are detected.

The value of "zero" will be detected when the photodiodes with the two differences measure the same number of photons, on the other hand when there is a bending there is an imbalance of this equilibrium and therefore the signal will be different from zero. This technique can be used to study soft matter and also can be used to study samples in different environments, such as aqueous ones, without hindering the images obtained. There are different modes in which this instrument can be used, the first is the contact mode. This mode has the advantage of providing a better resolution but, on the other hand, it has the disadvantage of being quite invasive and therefore not suitable for soft samples or not well adhered to the substrate. The AFM can use other methods to perform measurements such as "no contact" and "intermittent contact" called tapping. This last technique scans the sample with the lever oscillating on the sample, therefore the contacts are intermittent, the contact occurs only at one point, after which the lever rises and moves to another point, which re-executes the operation. and proceed in this way to scan the whole sample. Through this technique the lateral force on the sample is greatly reduced, thus avoiding the dragging of the sample. Depending on the pressure exerted by the lever we can distinguish between hard tapping and soft tapping where in the first case the incision force of the lever is greater. The signal that is monitored with this technique is no longer the deflection, but the amplitude of oscillation kept in motion by a piezoelectric. The stick is kept in oscillation at the frequency close to the resonant one since it is easier to have the oscillation. The higher the oscillation amplitude, the weaker the interaction is with the sample because, with the free amplitude, the sample would be touched only at the extreme point of the oscillation while if the oscillation amplitude is reduced, a strong pressure will apply to the sample, as mentioned above we speak of hard tapping.

AFM measurements were performed using an AFM microscope (APEResearch srl) in contact mode (20 nN with a CSC17/Al BS tip supplied by NanoAndMore GMBH) over a square 5 × 5 μm area.

2.1.9 Transient Photovoltage and Transient Photocurrent

The setup to perform these two measurements is composed of a pulsed light source and an oscilloscope that measures the voltage (TPV) or the current (TPC) in the function of time. TPV gives information about the recombination rate of the material, meanwhile, TPC gives information about the extraction of the carriers.

In this research were used setups to perform TPV/TPC analyses the first one is a homemade setup that uses a blue LED to illuminate the device and to measure the current/voltage of a Picoscope 5000 oscilloscope. The second setup is Cicci Research Arkeo transient tests module. Measurements were conducted under constant 1 Sun illumination and the constant bias was perturbed with short light pulses of 200 μs width. Both measurements were performed in air and ambient conditions.

2.1.10 Photoluminescence

The photoluminescence (PL) is a method of characterization consists in measure the emission under incident light. The setup is composed of a light source such as a laser or a LED and a spectrometer that measures the emission of the sample. To prevent the detection of the reflected incident light a low-pass filter is used. Also, optical elements (mirrors and lenses) are installed to guide the light precisely and collimate the light; an alternative is the use of optical fibers. This characterization method can be coupled with microscopy to obtain maps of the entire sample.

PLQY (photoluminescence quantum yield) measurements were carried out inside an integrating sphere (Labsphere) with excitation by a 405-nm continuous wave (CW) laser (Coherent). The spectra were recorded using a QE65 Pro (Ocean Optics) spectrometer. The PLQY was calculated following the methodology of de Mello et al. a second setup used to perform PLQY measurements was a custom-made setup employing a Labsphere integrating sphere and a 520 nm laser (Thorlabs' Single Mode Pigtailed Laser Diodes, LP520-SF15), using a power of 5 mW. The scan range was set between 480 and 900 nm with 15 nm resolution at central wavelength. PL emission maps were acquired using a wide-field, hyperspectral imaging microscope (Photon, etc. IMA VIS). The maps were detected with a front-illuminated, low-noise charged-coupled device camera that was thermoelectrically cooled down to 0 °C. A power-tunable 405 nm laser with an intensity of 100 mW cm^{-2} (spot size diameter is ≈150 μm) was used as the excitation source for PL. To block the 405 nm laser reflection, a 420 nm long-pass filter was placed in the detection pathway. The hyperspectral imaging system records a luminescence intensity signal along three dimensions {x,y,λ}. The set-up is composed of a home-built microscope with Thorlabs optomechanical elements, a 2D bandpass filtering system from company Photon Etc with 2 nm resolution, and a 1Mpix silicon-based CCD camera PCO1300. The sample was illuminated (λ = 405 nm) through an infinity-corrected ×50 Nikon objective with a numerical aperture of 0.6, and the luminescence is collected through the same objective. The excitation beam and luminescence signals are separated with appropriate Thorlabs dichroic beam splitter (DMLP 495) and filters (FESH 450, FELH 450). The 2D luminescence signal is corrected for each pixel of the sensor from the spectral transmissions along all the optical paths, from the read noise and dark current noise of the camera. The incident photon flux measured was 100 mW/cm^2, corresponding to 1 Sun equivalent photon flux. We obtained this photon flux by dividing the measured power of the LED used for the illumination under the objective over the LED spot size at the working distance of the objective. All the acquisitions were performed in a nitrogen atmosphere. Post-treatment of the data cubes includes a deconvolution and fit to the generalized Planck law, which is realised with a dedicated Matlab routine employing the Levenberg−Marquardt algorithm.

2.1.11 Time Resolved Photoluminescence

It is a technique that investigates the lifetime of the carriers. The setup is composed of a pulsed light it can be a laser, LED coupled eventually with a monochromator and as a detector a Time-Correlated Single Photon Counting (TCSPC) or a Multi-Channel Scaling (MCS) detector. Also in this case it is possible to take images of the decay time coupling with a microscope.

TRPL (time resolved photoluminescence) signals were acquired on a custom-made setup, employing a pulsed 470 nm laser (PicoQuant, LDH-DC-470). The spot diameter was measured to be 10 μm, the repetition rate was set to 10 MHz and energy fluence was determined to be 5.0×10^{-5} Jcm^{-2}. Decays were collected at maximum PL emission wavelength. The TR-FLIM setup records luminescence intensity over an imaging sensor and as a function of time. We used a Princeton Instrument PiMAX4 gated camera. We used 3 ns wide temporal gates that we slid in time to record the local decays of the films. The illumination was performed with a Coherent Laser ($\lambda = 532$ nm, pulse width 15 ps), defocused, and homogenized by a rotating diffuser to obtain a flat and homogenous wide field excitation. The repetition rate of the laser was set to 40 kHz.To estimate the fluences, the wide field illumination was imaged with a portable CCD array to obtain the illumination area while the incident power was also measured. A ×10 objective was used both for excitation and collection, and the laser was filtered out with a DMLP650R beam splitter as well as with a FEL0680 filter. Each acquisition was repeated two times in a row to check for any reproducibility issue (none was found) and to obtain a better average signal-to-noise ratio.

2.1.12 Time of Flight-Secondary Ion Mass Spectroscopy

This technique measures the composition of the samples on the surfaces. The setup has to be in a high vacuum chamber, it is composed of a primary ion source, usually ionized noble gases but also ionized molecules can be used, the instrument can have also more ion sources to perform this characterization to every kind of sample. It is present a mass analyzer, it is possible to separate the secondary ions in different ways mass to charge ratio (sector field mass spectrometer), resonant electric field (quadrupole mass analyzer), and then by their velocity (time of flight mass analyzer). The setup has a detector coupled to an electron multiplier. The principle is to hit the sample with a beam generated by the ion source and measure the secondary ions to know the surface composition. It is possible to couple the instrument with a sputter to studies in the depth of the sample.

ToF-SIMS analyses were performed using a ToF-SIMS 5-100 instrument, with the pulsed primary ions from a Cs^+ (2 keV) liquid–metal ion gun for sputtering and a Bi^+ pulsed primary ion beam for analysis (30 keV), the detection area was 150 × 150 μm.

2.1.13 Electroluminescence

This characterization technique consists in measuring the emission of a device when is stimulated by an electric current. Typically, the setup is composed of a power supply that applies the electric stimulation to the sample and a spectrometer that measure the emission.

ELQE was characterized by directly covering the devices with a calibrated Si photodiode (Thorlabs, FDS10X10). Two source meter units were used for applying a voltage to the device and reading current from the photodiode, respectively, controlled by the SweepMe! software. Another setup used was a Cicci Research Arkeo steady-state tests module, applying 1.05 V to the samples. Spectra were acquired from 325 to 1100 nm, with 5000 ms as integration time.

2.2 Materials

All solvents and chemicals were used as purchased without further purification. Acetone (extra pure, 99+%), isopropanol (IPA, 99.5+%), and chlorobenzene (CB, extra dry, 99.8%) were purchased from Acros Organics. Tin (iv) oxide (SnO_2 15% in H_2O) and N,N-dimethylformamide (DMF, anhydrous, 99.8%) were purchased from Alfa Aesar. Dimethyl sulfoxide (DMSO, anhydrous, ≥99.9%), MACl, N2,N2,N2′,N2′,N7,N7,N7′,N7′-octakis(4-methoxyphenyl)-9,9′-spirobi[9H-fluorene]-2,2′,7,7′-tetramine (Spiro-OMeTAD, 99%, HPLC), Bis(trifluoromethane)sulfonimide lithium salt (Li-salt, 99.95%), acetonitrile (ACN, anhydrous, 99.8%), and 4-tert-butylpyridine (4-tBP,98%) were purchased from Sigma-Aldrich. Lead iodide (PbI_2, >98.0%) was purchased from TCI. Formamidinium iodide (FAI, >99.99%) and 4MePEACl were purchased from GreatCell Solar Materials. Unless otherwise stated, all materials were purchased from Sigma-Aldrich or Alfa Aesar and used as received. Perovskite films and devices were fabricated using PbI_2 and PbBr2 (99.99% purity) purchased from TCI, organic halide salts were purchased from GreatCell Solar, and cesium iodide (99.99% purity) was purchased from Alfa Aesar. The poly(triaryl amine) (PTAA) was purchased from Sigma-Aldrich. The $PC_{61}BM$ was purchased from Solenne. The bathocuproine (BCP; sublimed grade, 99.99% purity) was purchased from Sigma-Aldrich. All the anhydrous solvents were purchased from Acros Organics.

2.3 Device preparation

In this research glass substrates patterned with ITO were used, before the deposition they were cleaned with acetone and IPA consecutively by ultrasonication bath for at least 15 min for each solvent. Substrates were dried with an N_2 gun and treated for 10 min in an oxygen-plasma cleaner (ZEPTO, Diener Electronic), or with a UV-ozone lamp. The last step is to favor the stick of the first layer on the substrate. The devices were prepared by solution process to throw a spin coater and hot plate. The layers were deposited one after the other. The technique used was the spin coating.

2.3.1 Spin coating

The spin coating is a deposition technique with optimized parameters it is possible to fabricate high quality thin layers. The technique is reliable, highly reproducible, and economical in the requirements that have allowed its widespread research use. The concept of this technique is simply a solution is released on a substrate then this substrate starts to rotate at high speed, so the solution spread all over thanks to the centrifugal force and the evaporation of the solution. The thickness of the deposited layer depends on several factors, the spin speed, the acceleration in some cases, the concentration of the solution, the solvent used, the temperature, and the environment. It is possible to write an equation taking into consideration all the parameters but is complex since takes in a differential equation of fluid dynamics. It is possible to condensate them in constants and use just one variable, the most used is the spin speed and the concentration of the solution obtaining for the concentration a linear dependence

$$t \propto [C] \tag{70}$$

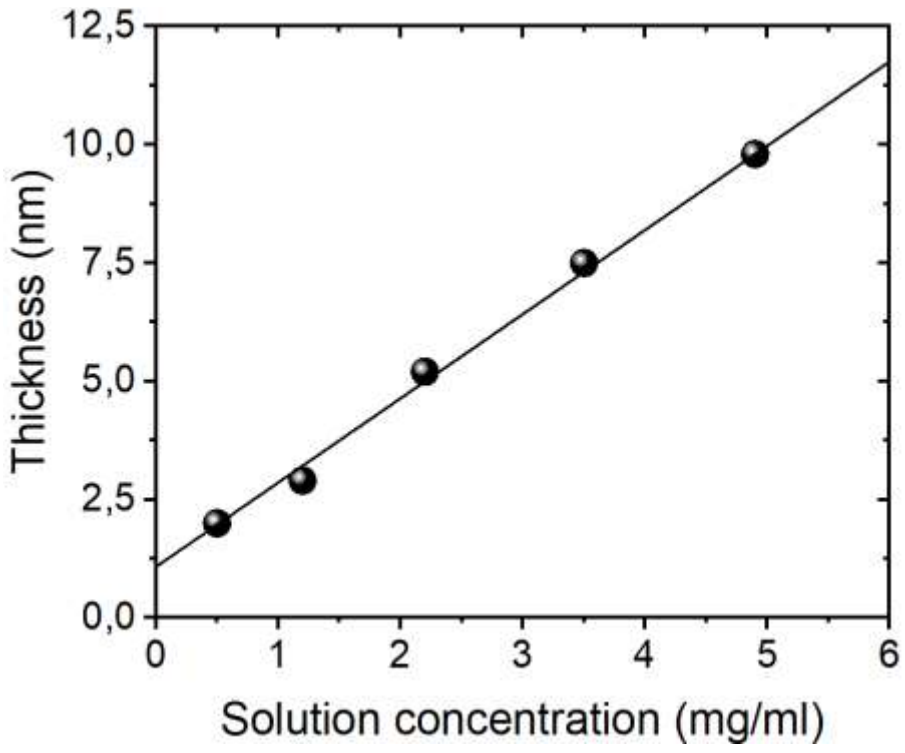

Figure 20 – Film thickness as a function of a concentration of the solution throw spin coating technique.

Meanwhile for the angular velocity

$$t \propto \frac{1}{\sqrt{\omega}} \tag{71}$$

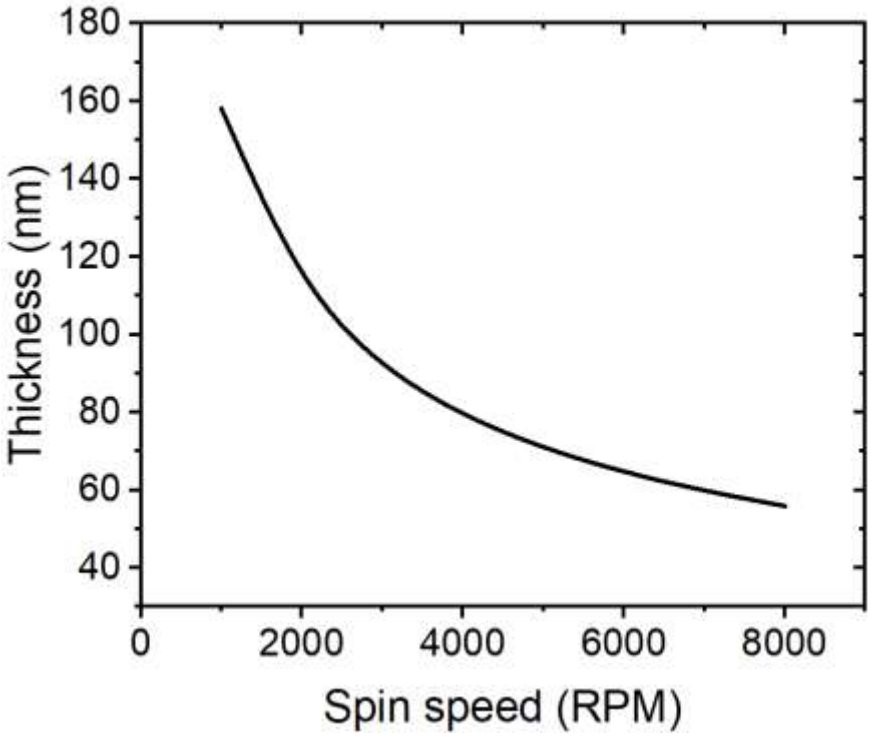

Figure 21 – Film thickness as a function of spin speed of the spin coater

This instrument is composed of a vacuum pump, an electric motor that provides the rotation, and a chuck to hold the sample. The spin coating technique can be used in two ways: the first "static" and the second "dynamic". At the first, the solution is deposited on the substrate to wet the entire surface, then the rotation of the spin coater (previously set) is activated, and an appropriate time is waited (also previously set) for the formation of the layer. The second method consists of the drop of the solutions during the rotation of the substrate. The choice of the method depends on the substrate and the solution since the adhesion forces are different and one technique can be better than the other depending on each case.

2.3.2 Fabrication of N-I-P devices

SnO_2 colloidal dispersion was diluted to 12% in water and 50 µL were spin-coated onto ITO/glass substrates and annealed at 150 °C for 30 min. SnO_2-coated substrates were subjected to UV-ozone treatment for 30 min. All solutions were prepared in an Ar-filled glovebox, while the deposition of each layer of the solar cell was performed in an N_2-filled glovebox.

The perovskite precursor solution (1.1 M) was prepared by dissolving PbI_2 and FAI powders in a DMF/DMSO = 4/1 solution with 1% PbI_2 excess. For bulk treatment, 20 mol% of MACl was added to the solution. 25 µL of the final solution were deposited on the SnO_2-coated substrates and spin-coated with a three-step procedure: in the first step substrates were spun at 1000 rpm for 12 s, the second step proceeded at 5000 rpm for 27 s, while the last step was a speed reduction of 4 s. 10 s after the beginning of the second step, 150 µL of CB were dropped onto the spinning substrate for an antisolvent procedure. Subsequently,

substrates were annealed at 150 °C for 30 min. For the surface passivation of the perovskite, 50 µL of a solution 0.01 M of MePEACl in IPA were dynamically spin-coated onto the perovskite layer at 4000 rpm for 30 s, and substrates were annealed at 100 °C for 10 min.

To fabricate the HTL, Spiro-OMeTAD was dissolved in CB to produce an 80 mg mL^{-1} solution. The solution was doped by adding 17.5 µL of Li-salt dissolved in ACN (500 mg mL^{-1} in ACN) and 28.8 µL of 4-tBP to 1 mL of Spiro-OMeTAD solution in CB. 10 µL of the final solution were spin-coated onto the perovskite layer.

Finally, 80 nm of Au were thermally evaporated on the device with a shadow mask of 0.0825 cm^2 area. The evaporation speed was adjusted to 0.01 nm s^{-1} for the first 5 nm, 0.02 nm s^{-1} from 5 to 15 nm, and 0.08 nm s^{-1} for the rest of the procedure.

J–V curves of the produced PSCs were carried out in ambient air, using a Keithley 2400 sourcemeter and a Wavelabs SINUS-70 solar simulator. The simulated 1Sun AM1.5G illumination was calibrated using a certified Si reference cell (Open RR-1002, KG5 window). The devices were measured both in reverse scan (1.2 V à 0 V, 130 mVs^{-1}) and forward scan (0 à 1.2 V, 130 mVs^{-1}). During every measurement, a metal shadow mask with an aperture area of 0.03 cm^2 was used to cover the active area of the device to avoid the artifacts produced by the scattered light.

2.3.3 P-I-N

The HTL and the perovskite films were fabricated in a drybox (relative humidity (RH) <1%), while the ETL and the contacts were deposited inside a glovebox filled with inert atmosphere N_2. For reference devices, an HTL of ~10-nm thickness made of PTAA with a concentration of 1.5 mg mL^{-1} dissolved in toluene was spin-coated at a speed of 2000 rpm for 40 s and then annealed at 100°C for 10 min. After the annealing step, the samples were washed by DMF by spin-coating it on the prepared PTAA films at 4000 rpm for 30 s. The perovskite precursor solution (1.2 M) contained mixed cations (Pb, Cs, FA, and MA) and halides (I and Br) dissolved in a solvent mixture (DMF/DMSO = 4/1) according to a formula of $Cs_{0.05}(FA_{5/6}MA_{1/6})_{0.95}Pb(I_{0.85}Br_{0.15})_3$ with an excess of PbI_2 of 1%. For devices containing an ionic liquid, a piperidinium salt $[BMP]^+[BF_4]^-$ was dissolved in the perovskite solution at a molar ratio of 0.25 mole percent. The perovskite layer was deposited via a two-step spin-coating procedure with 1000 rpm for 12 s and 5000 rpm for 27 s. A mixture of antisolvents [chlorobenzene (CB)/IPA = 9/1, 150 µl] was dripped on the spinning substrate during the 21 s of the second spin-coating step. Subsequently, the samples were annealed at 100°C for 30 min. The ETLs were dynamically deposited from a $PC_{61}BM$ solution (20 mg/ml in CB) and spin-coated onto the perovskite layer at the speed of 2000 rpm for 30 s (with a ramping speed of 1000 rpm/s) and annealed for 10 min at 100°C. Next, thin layers of BCP (0.5 mg/ml in IPA) were spin-coated at 4000 rpm for 30 s (with a ramping rate of 1000 rpm/s) as hole blocking layers. The small-area devices with an area of 4.5 mm^2 were completed by thermally evaporating of Ag (80 nm). For large-area devices, Ag electrodes

with an area of 70 mm^2 were thermally evaporated. The devices with modified interfaces were prepared by dissolving a small amount of the PEAI-cations in DMF (20 mM) used for washing the PTAA and in the mixture CB/IPA (0.5 mM) used in the antisolvent step. For the fabrication of MA-free perovskite solar cells, a 1.1 M $Cs_{0.1}FA_{0.9}PbI_{2.9}Br_{0.1}$ perovskite solution was prepared by dissolving powders of CsI, FAI, PbI_2, and $PbBr_2$ in the molar ratio of 2:18:19:1 in 4:1 (v/v) DMF/DMSO. All other device fabrication steps were unchanged.

3 Results and discussion

In this chapter are presented the experimental results each section is dedicated to the related publication.

3.1 23.7% Efficient inverted perovskite solar cells by dual interfacial modification

In developing the approach for the dual optimization of the perovskite active layer interfaces, we focused on integrating the modification into deposition steps that are already present in the device fabrication of reference devices. In the case of the HTL/perovskite interface, the highly hydrophobic nature of poly[bis(4-phenyl) (2,4,6-trimethylphenyl) amine] (PTAA)[19,20] HTL makes it necessary to perform a prewashing step before the deposition of the perovskite precursor solution in which the solvent N,N′-dimethylformamide (DMF) is spin-coated atop the PTAA layer[21]. This has been shown to improve the wettability of the perovskite precursor solution on PTAA, allowing for the formation of the perovskite active layer. To modify this interface, we introduce the various PEAI cations (Figure 22A) into the DMF solution used for the prewash step at a 20 mM concentration. Following the prewash step that either contains (HTL-modified) or does not contain (reference) the PEAI cation, the perovskite solution is deposited as previously reported using the solvent engineering approach[22]. To trigger the crystallization of the perovskite layer, an antisolvent is dispensed onto the perovskite solution shortly before the end of the spin-coating step. For the modification of the top surface (ETL-modified), we introduce the PEAI cations into the antisolvent at a low concentration of 0.5 mM and complete the layer fabrication by thermal annealing. These steps are schematically summarized in Figure 22B. Considering that each of the modifications can be introduced on its own, we used this approach to fabricate four types of devices (Figure 22C): reference, HTL-modified, ETL-modified, and dual HTL + ETL–modified, which enable us to study the effect of each interface separately.

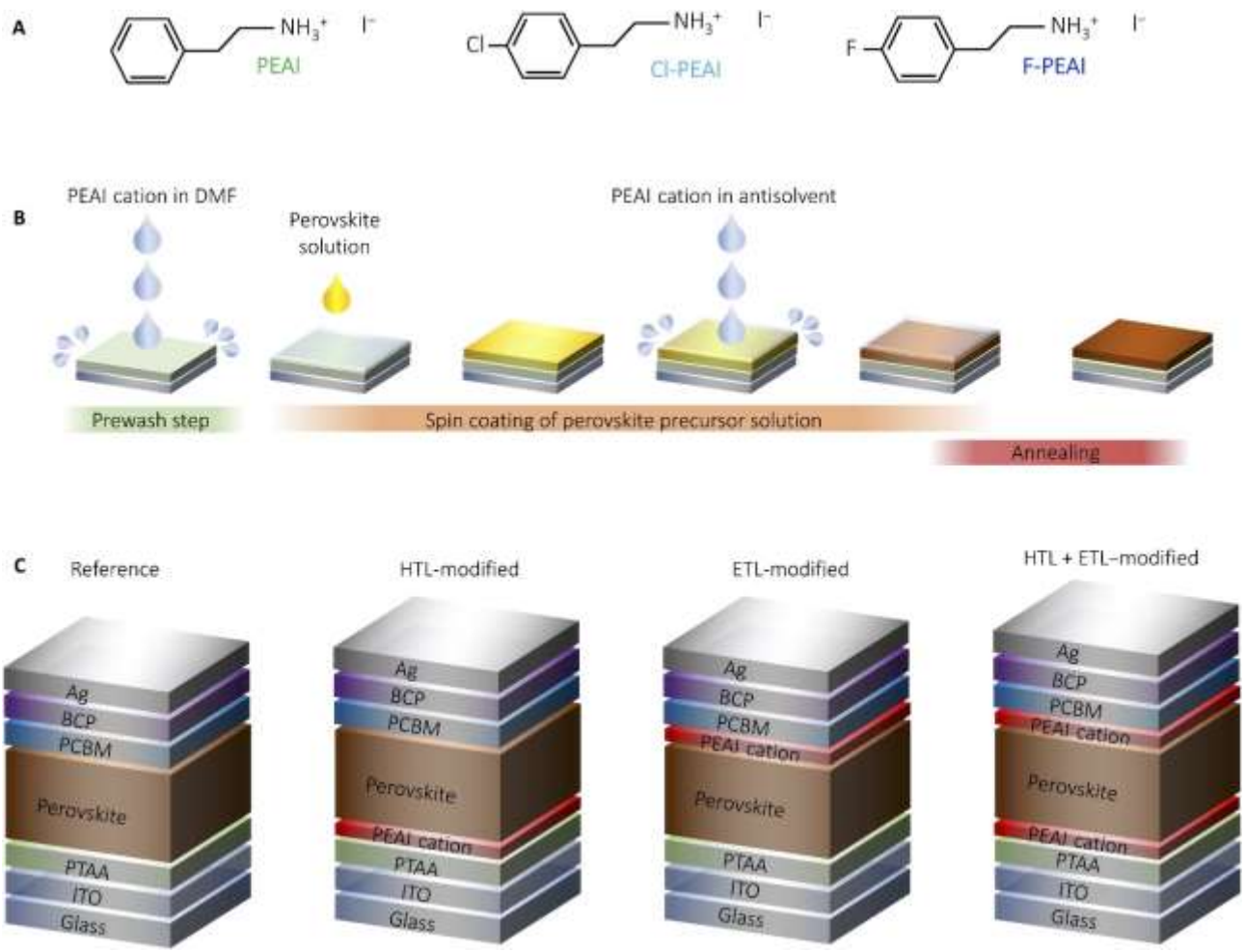

Figure 22 – A) Chemical structure of PEAI cations (PEAI, Cl-PEAI, and F-PEAI). B) Schematics of the fabrication procedure of the perovskite active layer. C) Solar cell device structures with the different combinations of passivated interfaces.

3.1.1 Dual interfacial modification approach

The introduction of the PEAI cations into the DMF wash step leads to an improvement in the photovoltaic performance, which can be seen in Figure 23 (A to D). While no change in the V_{OC} can be observed, a small increase in the J_{SC} is observed and a significant increase in FF. Together, these changes lead to an overall increase in the performance and a narrower distribution of the PCE. To investigate the origin of this increase in FF, we characterized the microstructure of the perovskite layers by scanning electron microscopy (SEM). Top-view SEM images acquired on reference perovskite layers (deposited on DMF-washed PTAA) exhibit a typical microstructure for triple cation perovskites, which consists of perovskite grains in the range of several hundreds of nanometers and small amount of excess lead iodide, which appears brighter in the SEM images (Figure 23E). Nano-sized pinholes (marked in circles) are also visible between some of the grains. Cross-sectional SEM reveals that small voids are also formed at the interface between the perovskite layer and the DMF-washed PTAA. On the other hand, samples that include an PEAI cation in the DMF wash step (Figure 23, F to H) compact layers with no observable pinholes. This is also supported by the cross-sectional SEM images that show a continuous interface between the PTAA and the perovskite layers for the HTL-modified

samples. Such a continuous and more intimate interface is expected to improve the efficiency of interfacial charge extraction and increase the shunt resistance of the photovoltaic devices. A similar effect has been previously observed in standard architecture devices, where the introduction of a self-assembled monolayer at the perovskite/ZnO interface led to a much-improved microstructure and an enhanced charge extraction[23]. Recently, it has also been shown that reducing the voids formed at the buried interfaces of blade-coated perovskites also improves the photovoltaic performance of perovskite modules[24]. Thus, our observation of a small increase in the extracted current density and the significantly enhanced FF of the PEAI cation HTL-modified photovoltaic devices is a result of the improved microstructure of perovskite layers formed on the PEAI cation–treated PTAA.

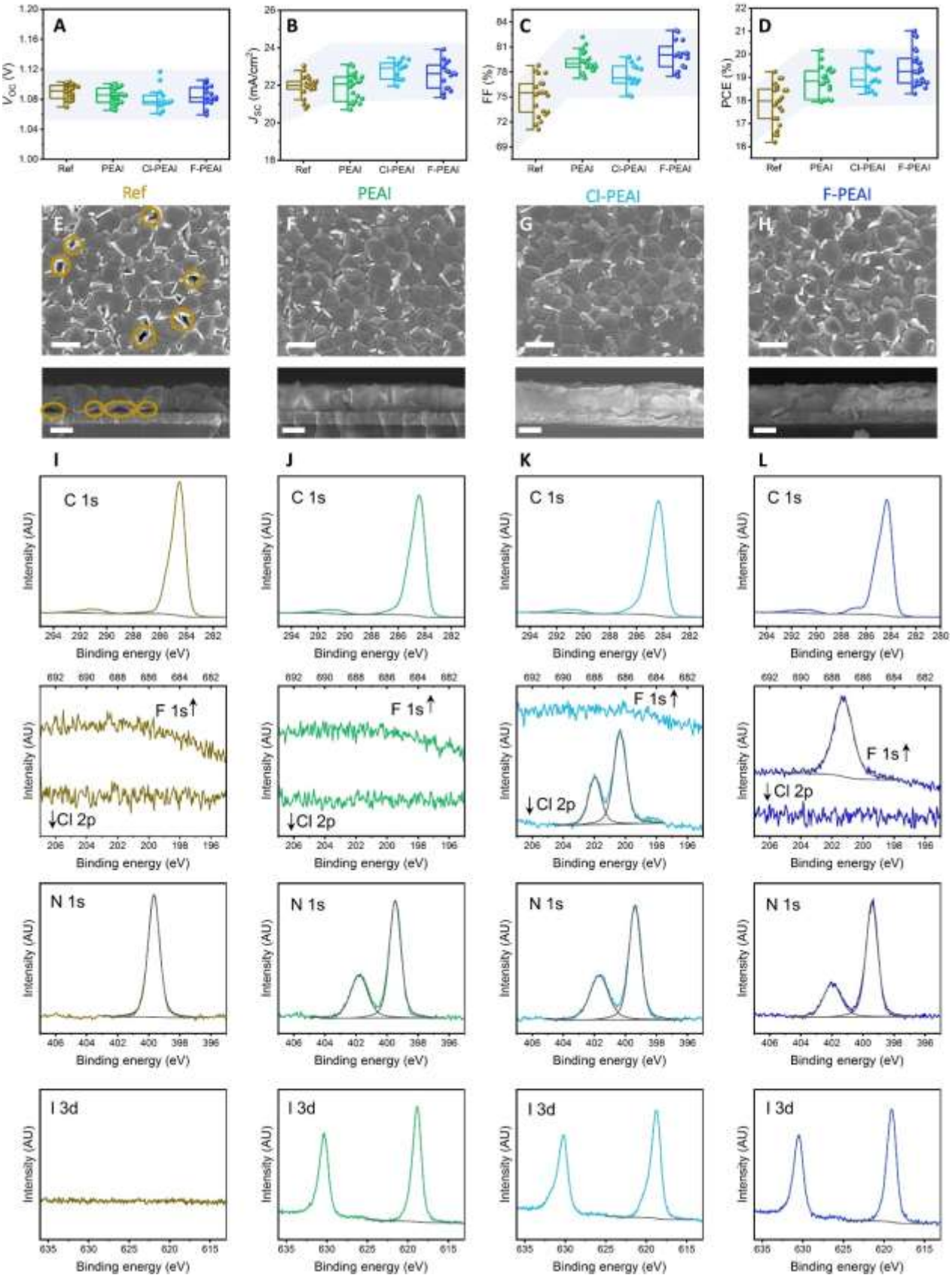

Figure 23 - Photovoltaic performance, microstructure, and interfacial composition of the HTL-modified devices. (A) VOC, (B) JSC, (C) FF, and (D) PCE of HTL-modified photovoltaic devices. Top-view and cross-sectional SEM of perovskite films deposited on (E) reference, (F) PEAI-modified, (G) Cl-PEAI–modified, and (H) F-PEAI–modified PTAA layers. Scale bars in top-view and cross-sectional images are 400 nm. C 1s, F 1s, Cl 2p, N 1s, and I 3d spectra measured on (I) reference, (J) PEAI-modified, (K) Cl-PEAI–modified, and (L) F-PEAI–modified PTAA layers. AU, arbitrary units.

This optimized interface to the PTAA HTL increases the shunt resistance of the solar cells (Figure 24).

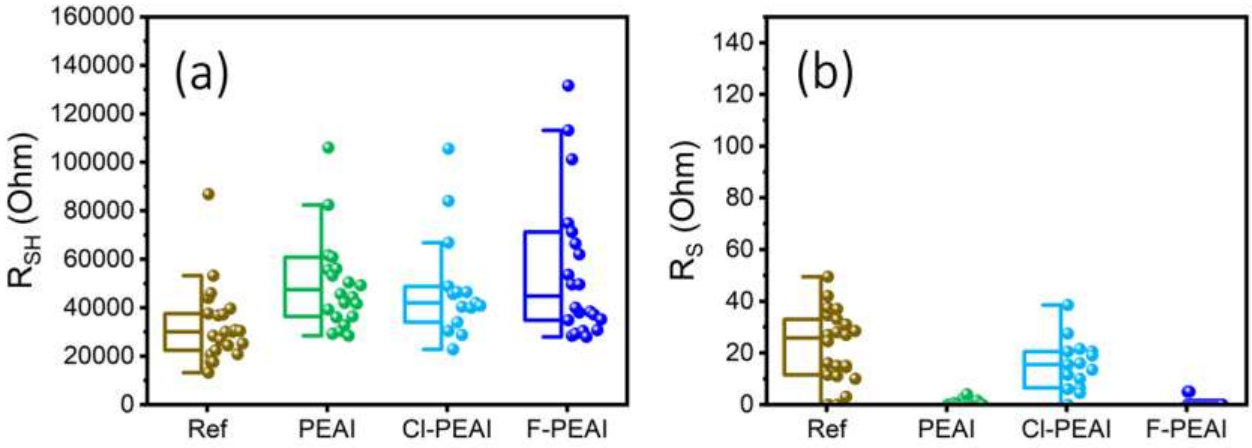

Figure 24 – a) Shunt and b) series resistance of HTL-modified solar cells.

The improvements in the microstructure suggest that the inclusion of the PEAI cations in the DMF wash step leads to a modification of the PTAA surface. This is confirmed by x-ray photoemission spectroscopy (XPS) measurements performed on PTAA and modified PTAA (Fig. 23, I to L). All of the samples show the characteristic C 1s and N 1s peaks associated with the PTAA polymer, the latter appearing at a binding energy of 399.5 eV, as expected from a triarylamine unit[25]. The presence of the PEAI cation on the PTAA after the DMF wash step is confirmed by the appearance of an additional N 1s peak at 401.8 eV, a I 3d doublet, and in the case of Cl-PEAI and F-PEAI, also the Cl 2p and F 1s signals. The atomic concentrations are summarized in table 1. This corroborates that a certain amount of the PEAI cations is left on top of the PTAA layer after the PEAI cation/DMF washing step.

Table 1 – Atomic percentages of PTAA and modified PTAA samples extracted from XPS measurements. C, N, I, F and Cl atomic percentages measured on PTAA washed with DMF or PEAI-cation/DMF

Element / Sample	C *1s*	N *1s* (PTAA)	N *1s* (PEAI-cation)	I *3d*	F *1s*	Cl *2p*
PTAA (DMF-wash)	95.12	4.88	-	-	-	-
PTAA (PEAI/DMF wash)	91.97	3.81	2.10	2.12	-	-
PTAA (Cl-PEAI/DMF wash)	90.09	3.66	2.19	2.27	-	1.79
PTAA (F-PEAI/DMF wash)	90.41	3.94	1.72	1.73	2.21	-

The presence of such organic salts—which are known to be polar—on top of the normally hydrophobic PTAA layer leads to an increase in its surface energy and consequently, a better wetting by the perovskite solution. This can be directly observed during the deposition procedure: The perovskite solution wets better the PEAI cation/DMF-washed PTAA than the pure DMF-washed PTAA (Figure 25). The improved wetting

leads to an improved microstructure of the perovskite layer and the elimination of nanovoids at the perovskite/HTL interface.

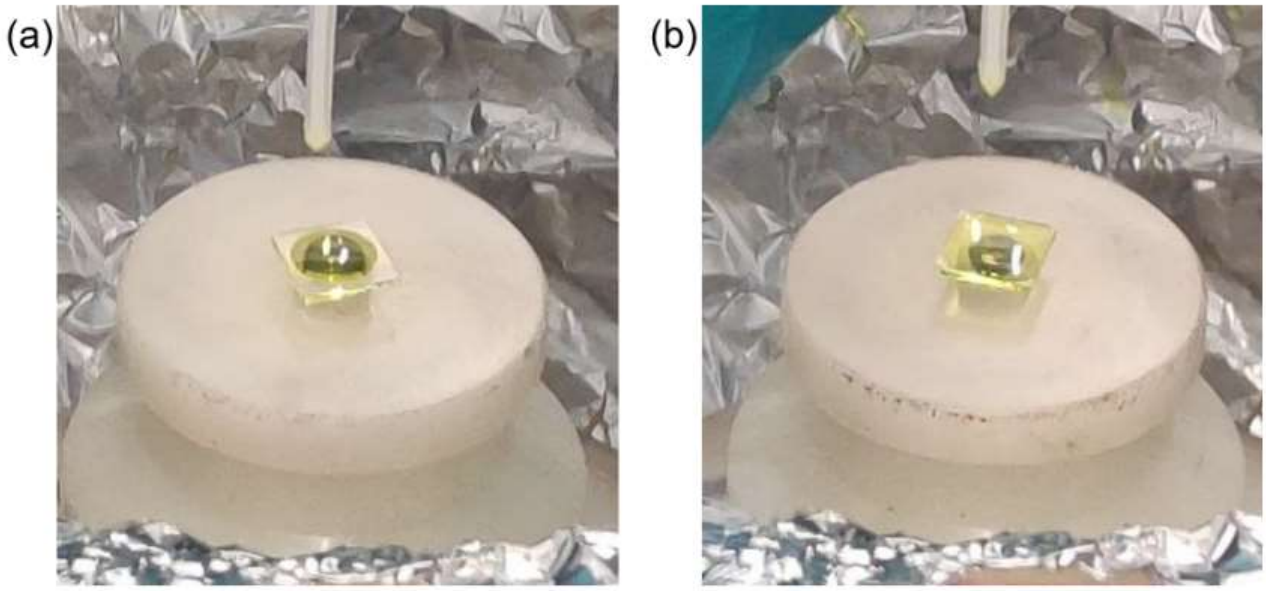

Figure 25 – Photographs of perovskite solution deposited on unmodified and F-PEAI-modified PTAA layer. Wettability of the substrates after the DMF wash. Drop of 40 ul of perovskite solution after the HTL treatment with (a) pure DMF, (b) solution of F-PEAI-cation in DMF

We note that the presence of the PEAI cations at the PTAA/perovskite interface does not change the energetic alignment at this interface, as is confirmed by ultraviolet (UV) photoemission spectroscopy (UPS) measurements (Figure 26).

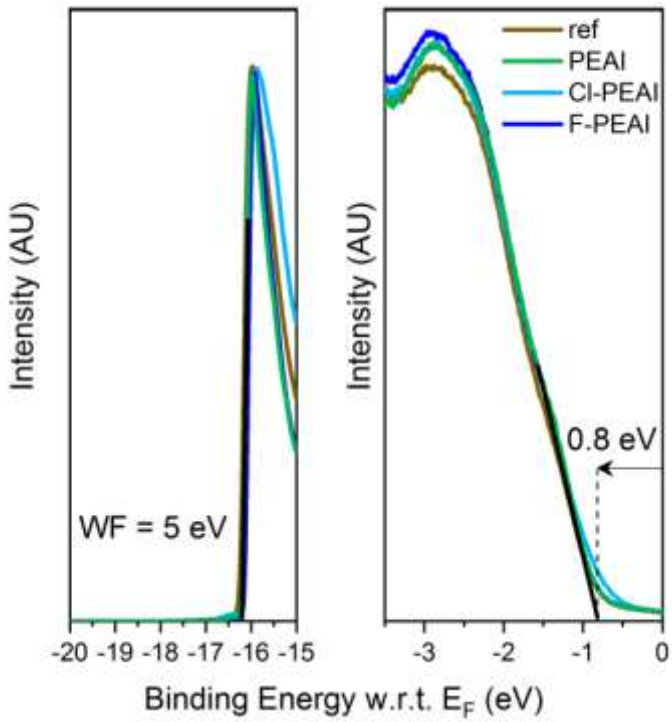

Figure 26 – UPS of perovskite/PTAA and PEAI-cation modified perovskite/PTAA thin films. Secondary photoemission and valence band region of reference and ETL modified perovskite films

The fact that the perovskite layer is deposited from a solution of DMF and dimethyl sulfoxide (DMSO) mixture—which can dissolve the PEAI cations—raises the question of whether any cations are left at that interface after the deposition of the perovskite layer. To simulate this scenario, but still have excess to probe the PTAA surface via XPS, we rinsed the halogenated PEAI-modified PTAA layers with a solvent mixture of DMF:DMSO (4:1) without the perovskite precursors. As can be seen in Figure 27, a small I 3d and Cl 2p/F 1s signal is observed in the rinsed samples, which demonstrates that a small fraction of PEAI cations remains on the surface and is not washed away.

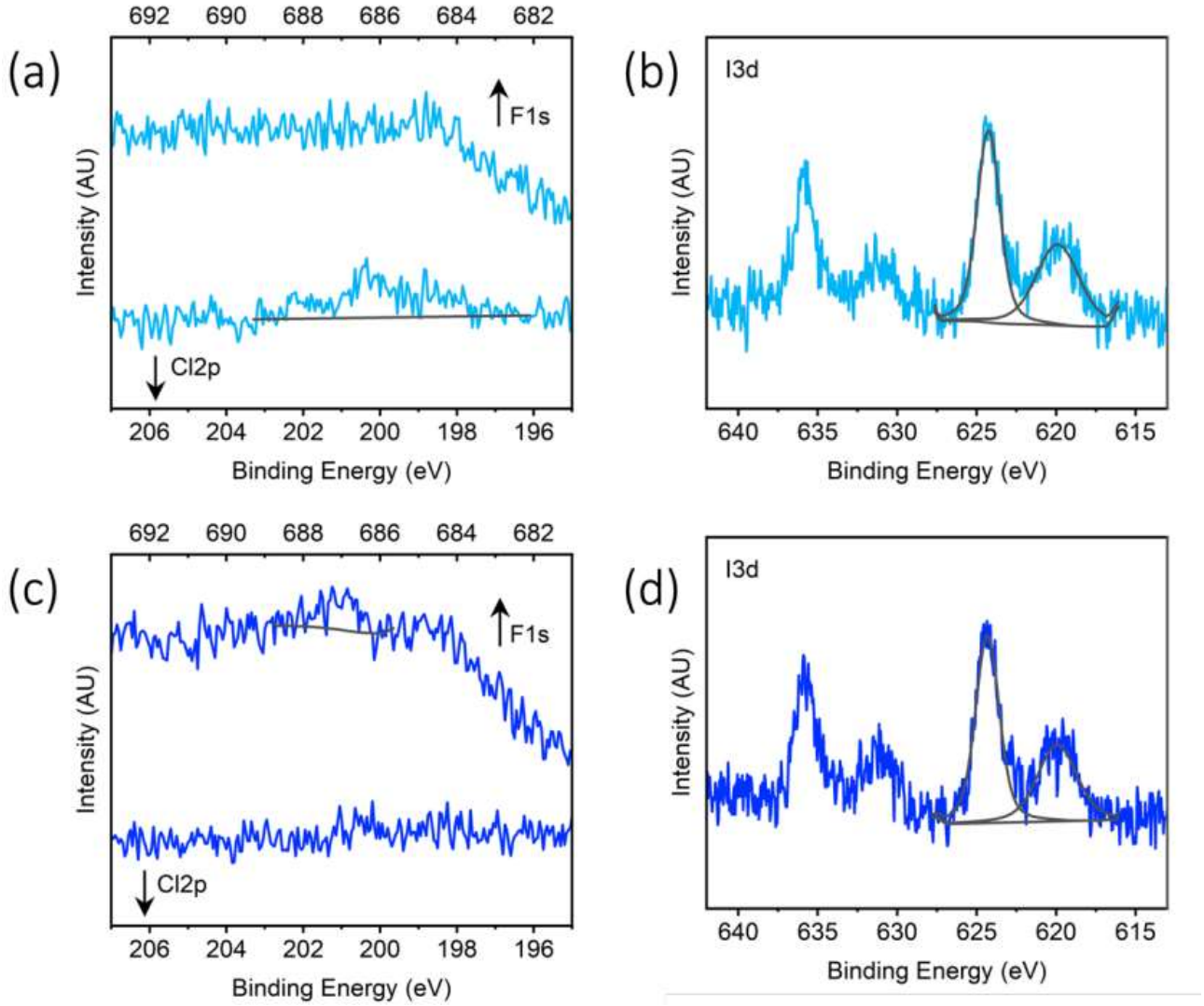

Figure 27 – XPS spectra of DMF:DMSO rinsed halogenated PEAI-modified PTAA samples. (a) F 1s and Cl 2p spectra and (b) I 3d spectrum collected on a DMF:DMSO rinsed Cl-PEAI modified PTAA sample. (c) F 1s and Cl 2p spectra and (d) I 3d spectrum collected on a DMF:DMSO rinsed F-PEAI modified PTAA sample.

We note that the second, high binding energy species of iodine is associated with a small amount of elemental iodine at the surface of the sample. To estimate the fraction of remaining PEAI cations, we compare the atomic % of the marker F and Cl elements in the rinsed samples as compared to the data collected on the samples before the rinsing (Table 1).

-We find that the atomic % is reduced from approximately 2 to 0.2% suggesting that only 10% of the PEAI cations remain on the PTAA surface after the rinsing with DMF:DMSO. We note that this experiment differs slightly from the case in which a perovskite layer is deposited atop the modified PTAA since, in that case, the perovskite precursors are available to react with the PEAI cations and potentially a slightly larger fraction of these cations will remain at that buried interface, so our estimate represents a lower boundary to the amount of PEAI cations at that interface. However, we highlight that the role of PEAI cations at the bottom interface is related to their impact on the wettability of the PTAA layer, which is greatly improved due to their polar nature. The improved wettability prevents the formation of nanovoids and results in a more uniform and homogeneous interface between the perovskite and the PTAA layer. Even if most of the cations are dissolved in DMF and washed away during the spin-coating, their function was already achieved by improving the perovskite film formation process. leading to an enhanced FF.

3.1.2 Perovskite/ETL interface modification by PEAI cations

To examine the effect of introducing the PEAI cations into the antisolvent step, we fabricated devices in which the HTL was left unmodified. Figure 28 (A to D) displays the photovoltaic performance parameters of the devices that clearly demonstrate that the modification leads to a significant increase in V_{OC} and FF. Such an improvement is typically associated with a passivation of the three-dimensional (3D) perovskite interface by a two-dimensional (2D) perovskite formed upon the introduction of large organic spacer cations[26–28]. To investigate whether a separate 2D perovskite layer is formed, we performed x-ray diffraction (XRD) experiments on the reference and PEAI cation–modified perovskite layers (Fig. 28E).

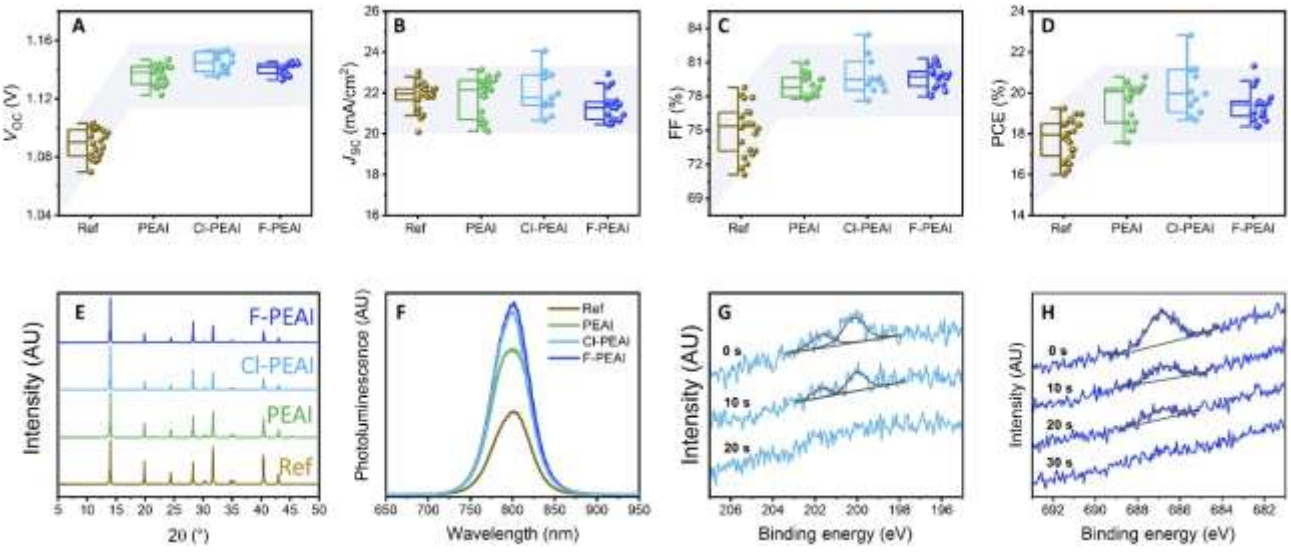

Figure 28 - Photovoltaic performance, crystalline structure, photoluminescence, and compositional depth profiling of perovskite layers made by PEAI cations containing antisolvent. (A) VOC, (B) JSC, (C) FF, and (D) PCE of photovoltaic devices where the perovskite was deposited by antisolvent containing PEAI, Cl-PEAI, and F-PEAI. (E) X-ray diffractograms and (F) Photoluminescence (PL) spectra measured on reference perovskite films and perovskite films deposited by antisolvent containing PEAI, Cl-PEAI, and F-PEAI. (G) Cl 2p and (H) F 1s spectra collected upon etching the perovskite layers for up to 30 s using an argon cluster ion source.

Indexing the diffraction reflections (Figure 29) reveals that only contributions from the 3D perovskites are observed.

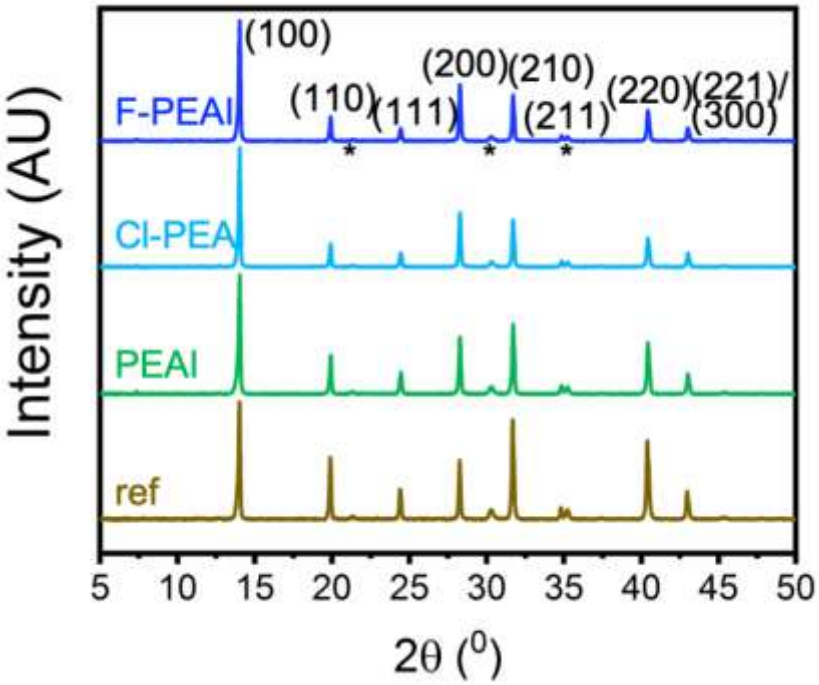

*Figure 29 – XRD of perovskite/PTAA and PEAI-cation modified perovskite/PTAA thin films. Indexed diffractograms of perovskite layers formed by using either a bare antisolvent (reference) or PEAIcontaining antisolvent. Reflections associated with the ITO substrate are indexed with a *.*

Since we observe no diffraction reflections that are associated with a 2D perovskite, it suggests that either no 2D perovskite layers are formed or it is below the detection limit of XRD. Similarly, no evidence of 2D perovskite is observed in UV-visible absorption measurements (Figure 30).

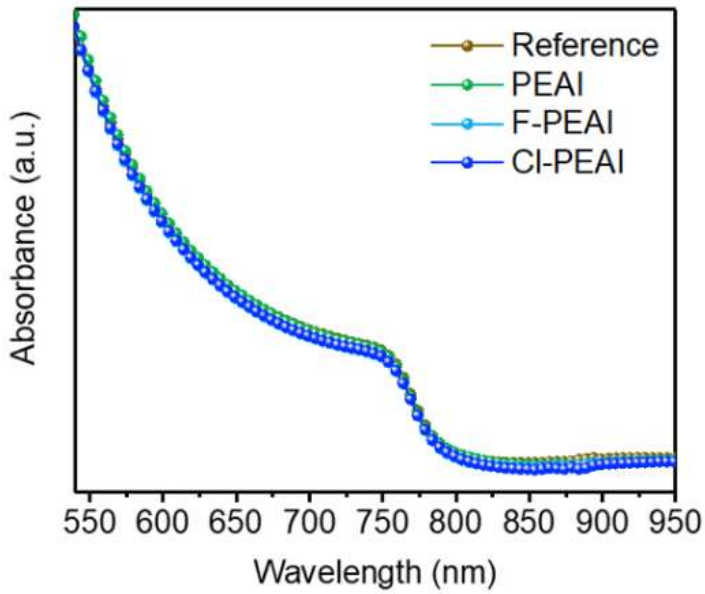

Figure 30 – Absorption spectra of perovskite/PTAA and PEAI-cation modified perovskite/PTAA thin films. UV-Vis absorption spectra for the reference and the ETL modified layer deposited on glass.

Surface and cross-sectional SEM images (Figure 31) also do not display any evidence supporting the formation of a surface 2D perovskite layer. Moreover, should a 2D perovskite layer were to form at the perovskite/ETL interface, its low electron affinity would hinder the electron extraction into the [6,6]-phenyl-C60-butyric acid methyl ester (PCBM) ETL; however, no such effect is observed since the JSC remains largely unchanged (Fig. 28B).

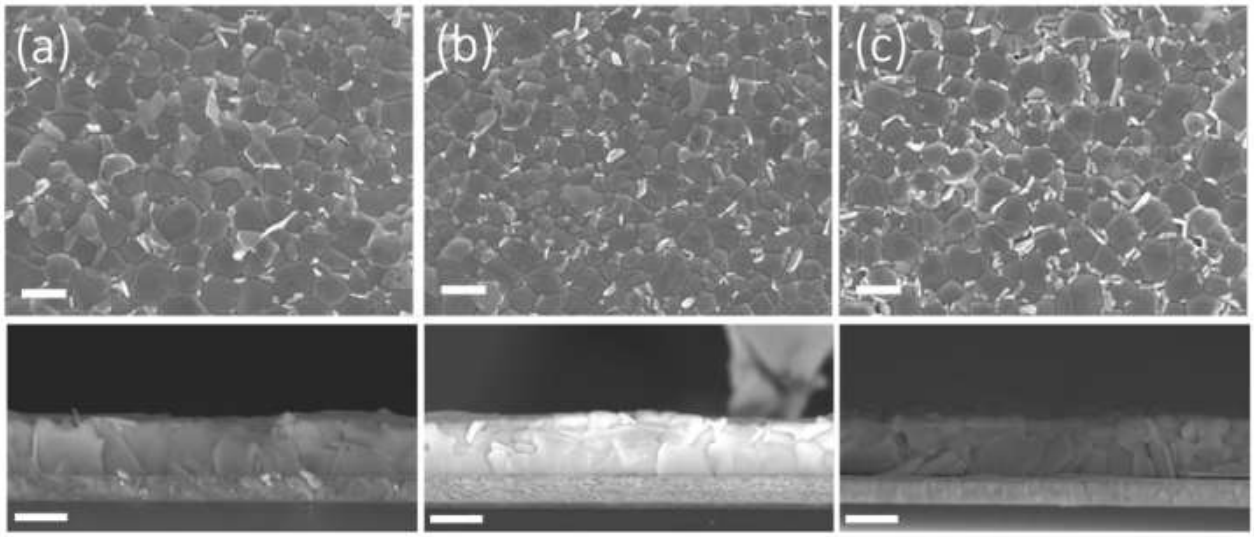

Figure 31 – Microstructure of dual-modified perovskite layers. Top-view and cross-sectional scanning electron microscopy images of HTL+ETL modified perovskite films using (a) PEAI, (b) F-PEAI and (c) Cl PEAI. Scale bar in top view and cross-sectional images is 400 nm, respectively.

These results, together with the fact that only a very small amount of PEAI cations is introduced during the antisolvent step, suggest that it is insufficient to form a separate 2D perovskite layer. We note that the concentration of PEAI cations in the antisolvent step can be easily controlled. In Figure 32, we show the performance of photovoltaic devices fabricated with varying amounts of F-PEAI (0.01, 0.25, 0.5, and 1 mg/ml). We find that the concentration (0.5 mg/ml) resulted in the optimal performance, which is why we selected to use it throughout the study. Increasing the concentration to 1 mg/ml led to a decreased performance, with a significant drop in both the J_{SC} and FF. We believe that at this concentration, a thin layer of 2D could form atop the 3D perovskite layer, which would lead to a reduced electron extraction due to the high bandgap of the 2D perovskite layer.

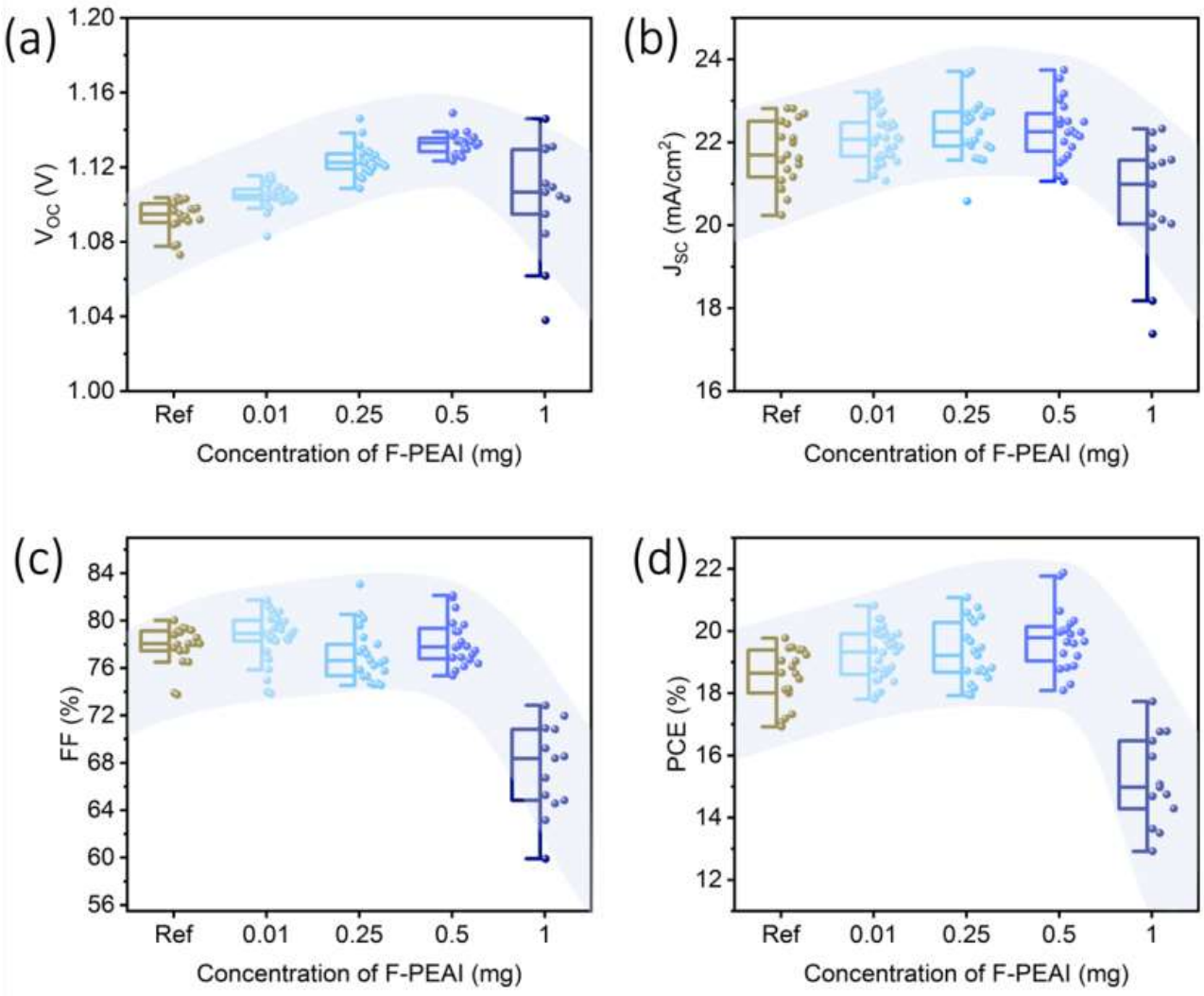

Figure 32 – Photovoltaic performance of solar cells fabricated with varying concentration of F-PEAI. (a) VOC (b) JSC (c) FF and (d) PCE of photovoltaic devices in which the concentration of F-PEAI in the antisolvent was varied

A possible reason for the increase in VOC can be a change in the energetic alignment at the perovskite/PCBM interface by the presence of PEAI cations[29]. UPS measurements show, however, that no changes in the energetic levels of PEAI-modified perovskite layers occur (Figure 33).

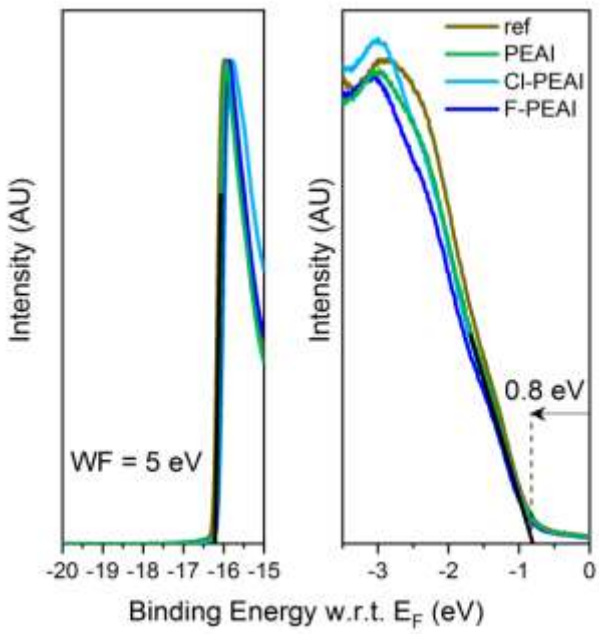

Figure 33 – UPS of reference and PEAI-cation dual modified perovskite/PTAA thin films. Secondary photoemission and valence band region of reference and dual modified perovskite films.

These results and the absence of a 2D perovskite layer suggest that the increase in VOC is associated with a passivation of the interface to the ETL by the PEAI cations[30]. Photoluminescence (PL) measurements confirm that the PL quantum efficiency (PLQE) of the perovskite films is significantly enhanced in films that were modified by including the PEAI cations in the antisolvent (Figure 28F). The PLQE of the reference film is 7%, while that of the modified films is more than doubled at 14 to 16% (Figure 34). This increase in PLQE suggests that the modified perovskite films exhibit suppressed nonradiative losses, leading to an increase in their V_{OC}.

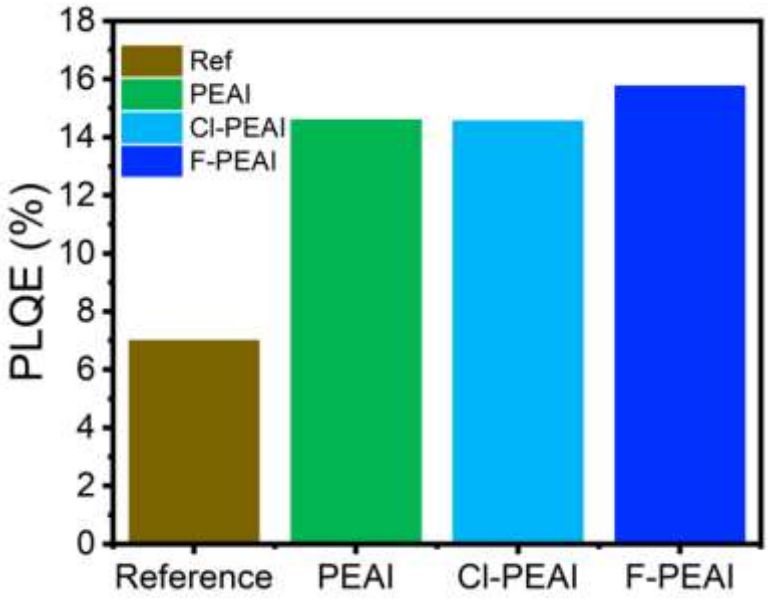

Figure 34 – PLQE values of PEAI-modified perovskite thin films. PLQE measurements for the reference and the ETL-modified perovskite layers deposited on glass

The incorporation of the PEAI cations via the antisolvent quenching step raises an important question regarding their distribution in the perovskite layer. XPS measurements performed on the reference and modified perovskite films confirmed that the PEAI cations are present in the modified perovskite layers (Table 2).

Table 2 – Atomic percentages of reference perovskite and PEAI-cations modified perovskite samples as extracted from XPS measurements. Br, Pb, C, N, I, Cs, F and Cl atomic percentages measured on perovskite layers formed by either a bare antisolvent or PEAI-cations containing antisolvent.

Element / Sample	Br *3d*	Pb *4f*	C *1s*	N *1s*	I *3d*	Cs *3d*	F *1s*	Cl *2p*
Perovskite (reference)	3.79	13.07	24.2	17.37	41.14	0.43	-	-
Perovskite (PEAI in the antisolvent)	4.09	13.57	21.02	17.56	43.32	0.44	-	-
Perovskite (Cl-PEAI in the antisolvent)	4.04	12.69	24.09	17.33	40.61	0.47	-	0.77
Perovskite (F-PEAI in the antisolvent)	4.01	12.73	23.95	17.11	40.46	0.46	1.28	-

To investigate whether the PEAI cations are located exclusively at the surface of the films or also in their bulk, we monitored the amounts of Cl and F in the Cl-PEAI– and F-PEAI–containing samples via XPS depth profiling (Figure 28, G and H). It can be seen that already after 20 to 30 s of etching using an argon cluster ion beam, the Cl 2p and F 1s signals are diminished. Considering the slow etching rate by the argon clusters (1.08 nm/min), a 30-s etching duration would remove less than 1 nm from the surface, thus confirming that the PEAI cations are exclusively located at the surface of the perovskite layers and there passivate the perovskite surface defects at the interface to the ETL.

3.1.3 Combined interfacial modification of both interfaces

Having examined the effects on each interface separately, it is important to explore wether both modifications can be combined in a single device. To test this, dual modified perovskite solar cells were fabricated and characterized (Figure 35).

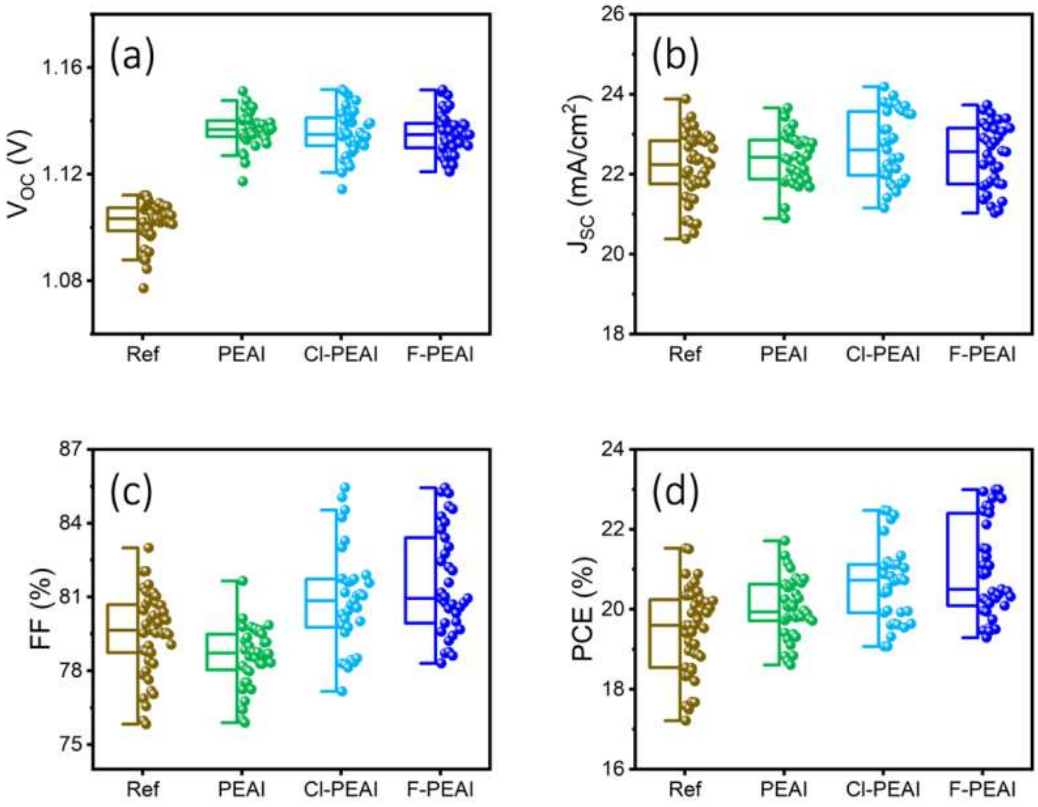

Figure 35 – Photovoltaic performance of dual modified photovoltaic devices. (a) VOC (b) JSC (c) FF and (d) PCE of photovoltaic devices where the both the HTL and ETL interfaces are modified by PEAI, Cl-PEAI and F-PEAI.

We observe that dual modified devices combine the improvements observed at each interface, resulting in a number of devices with PCE above 22% and a maximum value of 23%. Moreover, for such a dual interfacial modification to find broad use in inverted architecture solar cells, its efficacy needs to be examined in combination with a modification of the bulk of the perovskite layer[31,32]. For example, recent reports suggest that the introduction of ionic liquids into the perovskite active layer can significantly increase their stability[33–35]. To explore this, we fabricated photovoltaic devices that combine both interfacial optimizations shown above along with the introduction of an ionic liquid (piperidinium salt $[BMP]^+[BF4]^-$) into the perovskite active layer. Figure 36 (A to D) displays the photovoltaic parameters of the devices. In addition, in this case, we observe that both interfacial modifications can be successfully combined to increase simultaneously the V_{OC}, J_{SC}, and FF of the devices. The V_{OC} of the F-PEAI and Cl-PEAI devices was particularly high, reaching a maximum of 1.184 V. Similarly, the FF of these devices was also higher, reaching a maximum of 85%. Together, these improvements have led to high PCE reaching a maximum of 23.7% for the F-PEAI–modified device (Figure 35E).

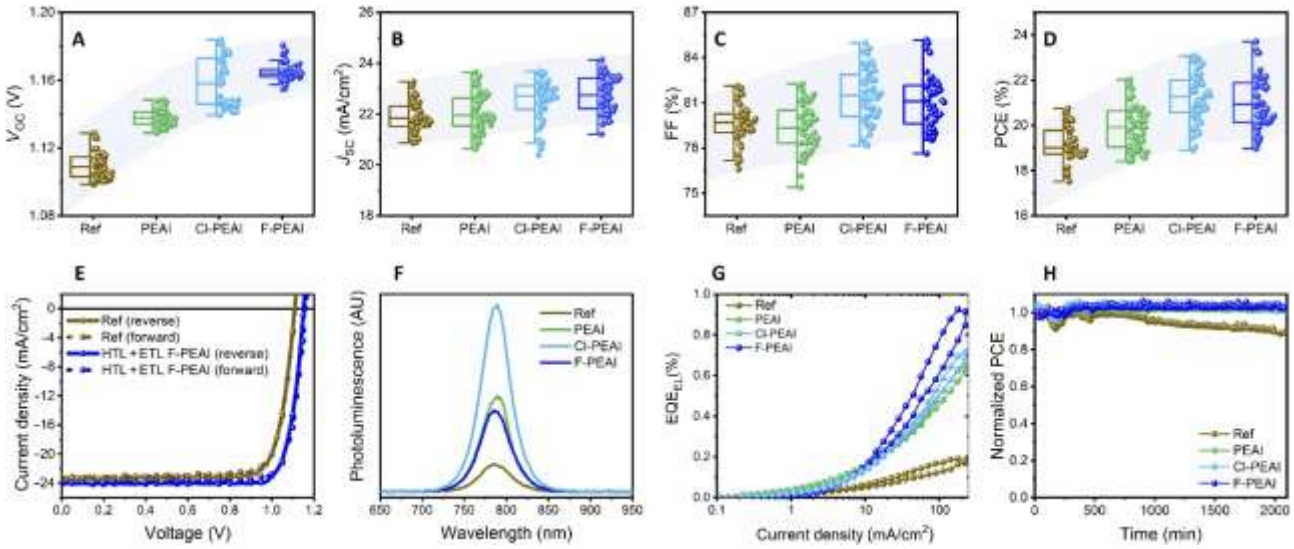

Figure 36 – Photovoltaic performance, photo- and electroluminescence, and stability of dual modified ionic liquid containing solar cells.(A) VOC, (B) JSC, (C) FF, and (D) PCE of photovoltaic devices in which both interfaces were modified by PEAI, Cl-PEAI, and F-PEAI. (E) J-V characteristics of champion reference and F-PEAI–modified device. (F) PL and (G) electroluminescence measured on reference and dual modified solar cells. (H) Evolution of the PCE of the reference and dual modified solar cells over 2100 min under continuous illumination in N2.

The photovoltaic performance of the champion devices of each type is summarized in Table 3. Devices fabricated using F-PEAI cations consistently outperformed those made using the other derivatives. We believe that this is associated with the fact that a larger quantity of F-PEAI remains at both the HTL and ETL interface as evidenced, for example, by the higher atomic % of F at both these interfaces as compared to Cl. We propose that this is associated with differences in the solubility of the PEAI cations.

Table 3 – V_{OC}, J_{SC}, FF, and PCE of highest performing photovoltaic devices in which both interfaces were modified by PEAI, F-PEAI, and Cl-PEAI in comparison to reference devices. Photovoltaic parameters for both reverse and forward directions scans are provided.

	V_{OC} (V)	**J_{SC} (mA/cm^2)**	**FF (%)**	**PCE (%)**
Ref	1.055	18.58	49.50	9.7
PEAI	1.098	19.53	65.72	14.09
Cl-PEAI	1.144	21.03	62.48	15.03
F-PEAI	1.122	19.66	67.46	14.88

We observe that F-PEAI cations are less soluble in the antisolvent (Figure 37), thus they will precipitate of solution earlier during the drying process of the antisolvent, thus resulting in a larger overall amount remaining on the surface.

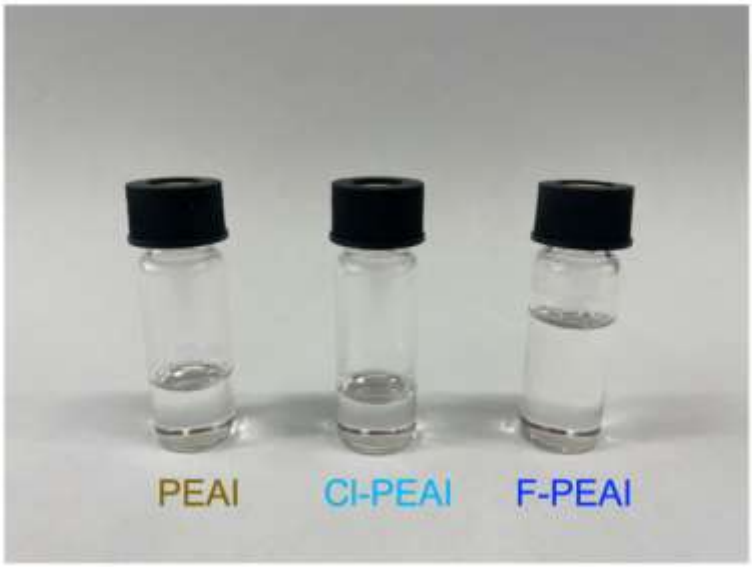

Figure 37 – Solubility tests of PEAI-cations in the antisolvent. The amount of antisolvent required to dissolve 10 mg of each PEAI-cation.

We note that the biggest contribution to the increased performance comes from the increase in V_{OC}. This is also evident from PLQE and electroluminescence QE (ELQE) measurements performed on representative solar cells (Figure 36, F and G). The PLQE of reference devices is very low at 0.14%. On the other hand, F-PEAI–modified devices reach a value of ~1%. Similarly, the ELQE of the devices is increased by a factor of ~4 at current injection equivalent to JSC, confirming a significant decrease in nonradiative losses in the dual modified devices (see Figure 38 for J-V-L measurements).

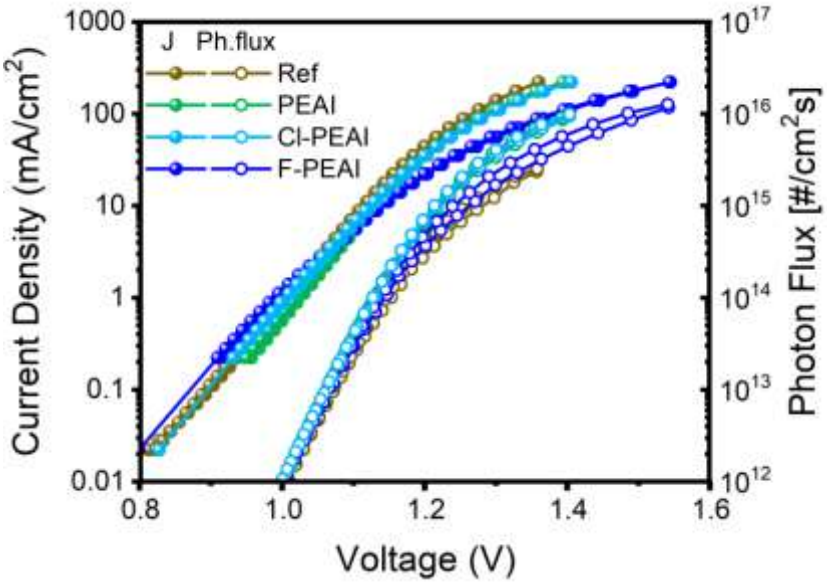

Figure 38 – J-V-L measurements of dual modified solar cells. Current density-luminescence (J-V-L) characteristics of ETL+HTL modified solar cells.

The minor increase in JSC is consistent with an improved charge extraction due to the more homogeneous, void-free perovskite/PTAA interface. This is also supported by our observation that the dependence of V_{OC}

and J_{SC} on light intensity is not affected by the dual interfacial modification, as both the reference and the modified device (Figure 39, A and B) display the same slope, thus suggesting that the bulk recombination in both cases is very similar. However, examining the photocurrent decay (Figure 39C) shows that it is faster in the case of the modified device, suggesting an improved charge extraction.

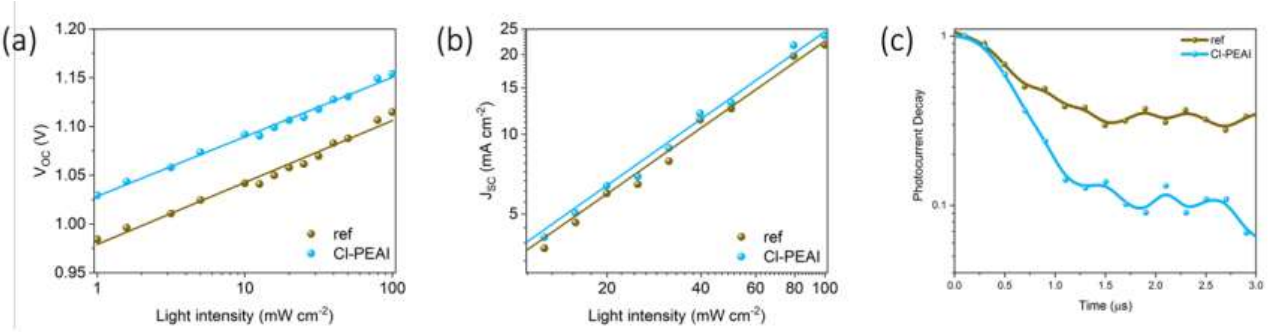

Figure 39 – Light intensity dependence and photocurrent decay of reference and Cl-PEAI devices. Light intensity dependence of (a) VOC and (b) JSC of reference and Cl-PEAI modified devices. (c) Photocurrent decay of reference and Cl-PEAI modified devices

The integration of ionic liquids into the active layer leads to an excellent stability of the dual passivated devices. For example, Figure 36H displays the evolution of the PCE of both the reference and PEAI cation dual modified devices under continuous illumination in N_2. It can be seen that the reference device is very stable, maintaining 90% of its initial performance after 2000 min of continuous illumination. The dual passivated devices, however, are even more stable, maintaining their original performance for the entire duration of the experiment. Examining the evolution of all the photovoltaic parameters (Figure 40) reveals that the loss in the performance of the reference device originates from a loss in JSC, possibly as a result of degradation at the perovskite/HTL interface mediated by the presence of nanovoids at that interface[22]. No deterioration in any of the photovoltaic parameters is observed for any of the dual modified devices. The observation that the dual interfacial modification approach developed here is fully compatible with the integration of ionic liquids into the perovskite active layer is highly promising for the application of this methodology for further development of efficient and stable perovskite solar cells in an inverted architecture.

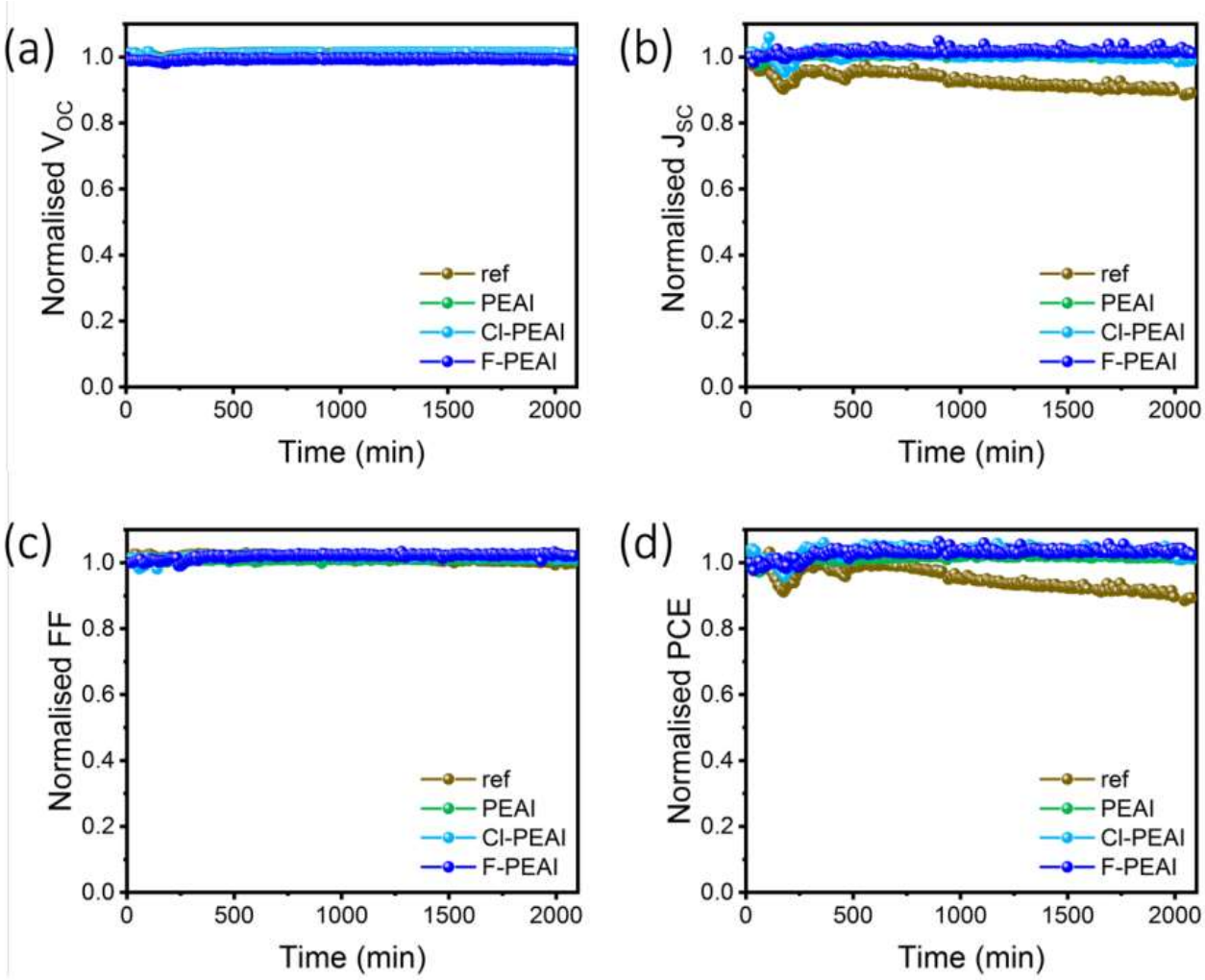

Figure 40 – Stability characterisation of reference and dual modified solar cells. Performance evolution of (a) VOC (b) JSC (c) FF and (d) PCE of ionic liquid containing photovoltaic devices where both the HTL and ETL interfaces were modified by PEAI, Cl-PEAI and F-PEAI.

It is important to explore the applicability of the dual modification approach for the fabrication of other types of inverted architecture solar cells. The increasing recent interest in methylammonium (MA)–free perovskite compositions[36–38] motivated us to examine whether the performance of $Cs_{0.1}FA_{0.9}PbI_{2.9}Br_{0.1}$ inverted architecture solar cells can also be enhanced by dual modification with PEAI cations. Figure 41 displays the photovoltaic performance of the devices, which, similar to the results on triple cation perovskite solar cells, exhibit a significant improvement in all of their photovoltaic parameters. These results confirm that the approach can be easily translated to the fabrication of inverted architecture solar cells based on other perovskite compositions.

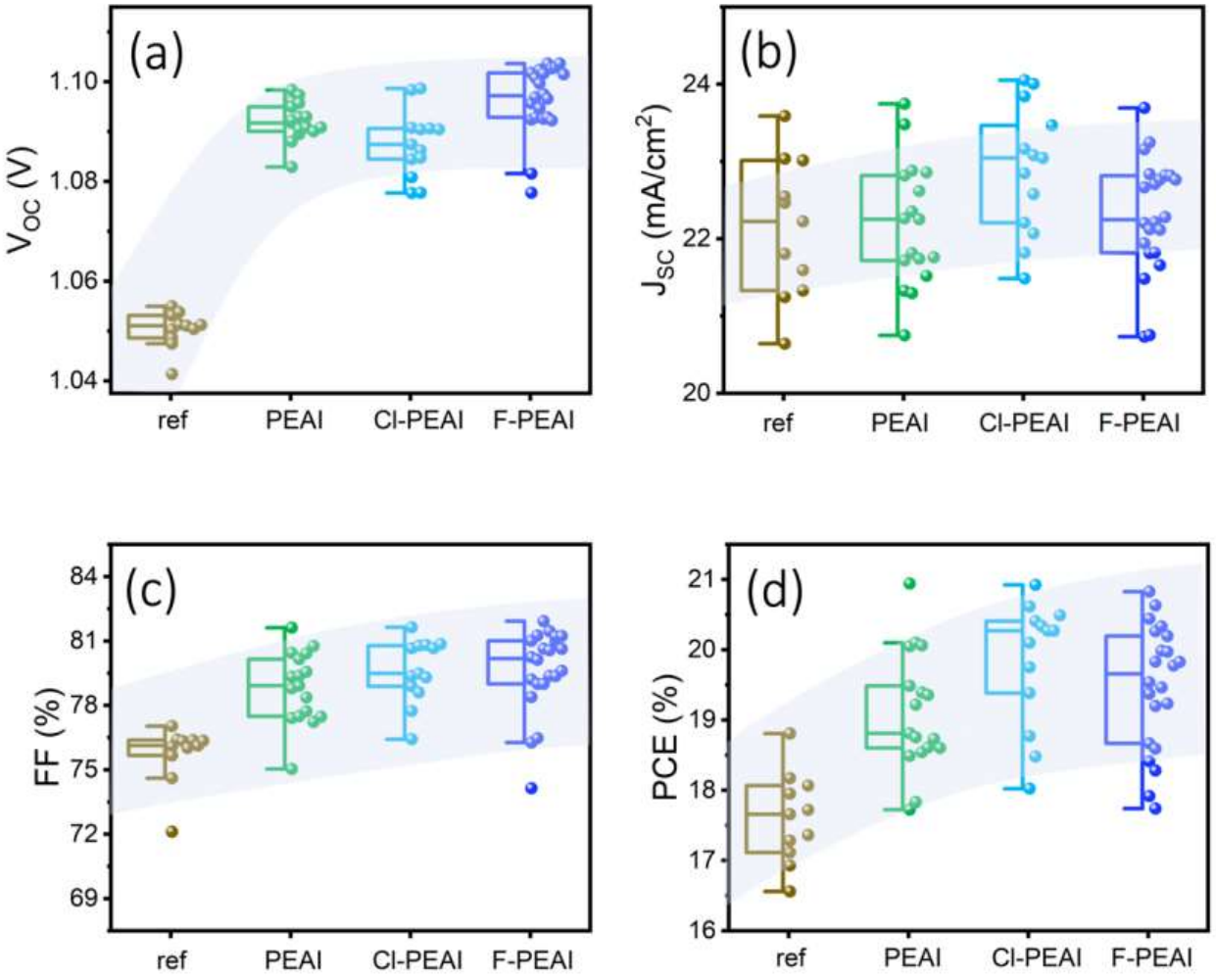

Figure 41 – Photovoltaic performance of dual modified MA-free photovoltaic devices. (a) VOC (b) JSC (c) FF and (d) PCE of MA-free photovoltaic devices in which both interfaces were modified by PEAI, Cl-PEAI and F-PEAI.

It is of potential interest to investigate whether the dual modification approach can be applied also to standard architecture photovoltaic devices. To preliminarily examine this, we fabricated devices with the architecture glass/indium tin oxide (ITO)/SnO_2/perovskite/SpiroOMeTAD/Au and performed the same interfacial modification procedure as described above with the PEAI cation. The photovoltaic results show that, while not fully optimized, the dual modified device performs significantly better than the reference ones (Figure 42), particularly due to an enhancement in their V_{OC} and FF. This suggests that our approach can be applicable also to standard architecture solar cells.

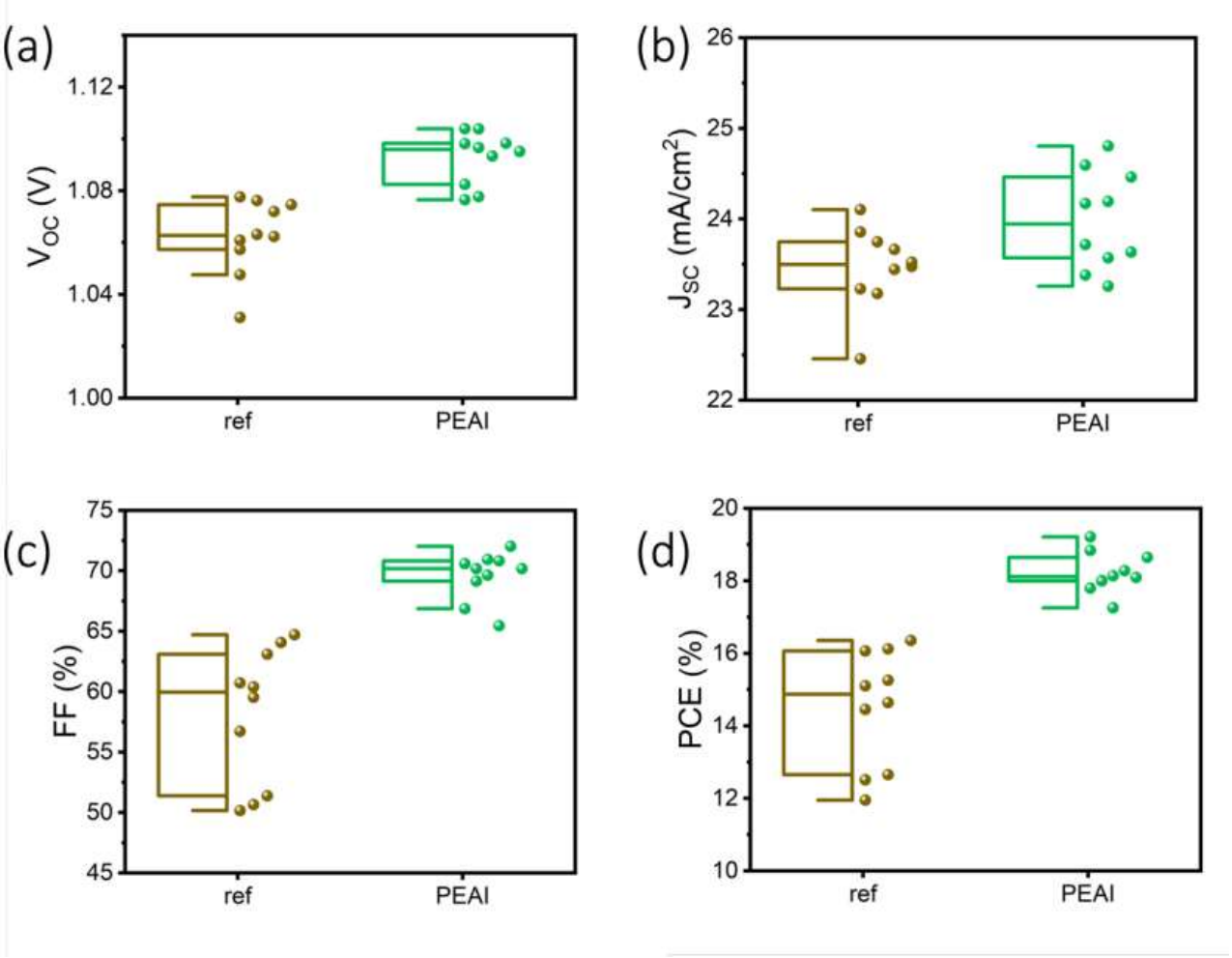

Figure 42 – Photovoltaic performance of dual modified MA-free photovoltaic devices. (a) VOC (b) JSC (c) FF and (d) PCE of MA-free photovoltaic devices in which both interfaces were modified by PEAI, Cl-PEAI and F-PEAI.

The observation that the dual modification approach can significantly increase the FF of the devices can be particularly useful in the case of large-area solar cells, which are known to suffer from low FFs[39]. To investigate this, we fabricated devices with an area of 70 mm^2, significantly larger than the small-area devices shown above (4.5 mm^2). We find that the dual modification approach is entirely applicable to large-area devices, with significant enhancements observed in all the photovoltaic parameters as compared to the reference device (Figure 43). We observe a major increase in the FF of the devices, suggesting that our approach can be used also for the fabrication of large-area solar cells.

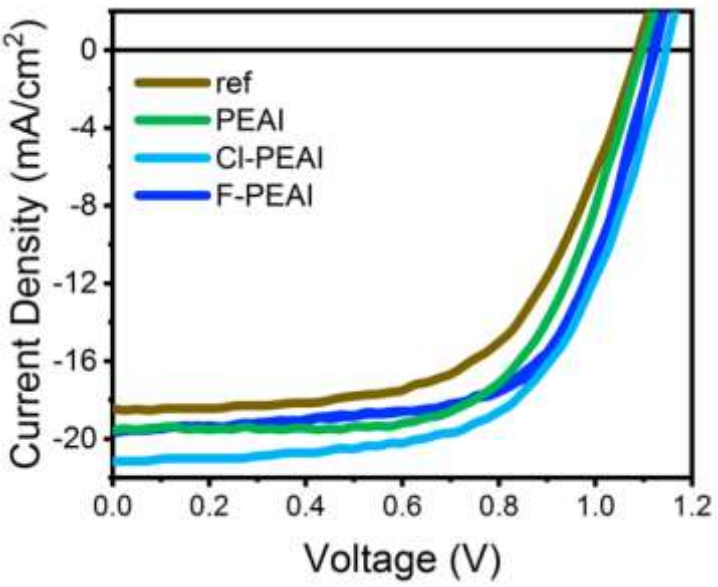

Figure 43 – Photovoltaic performance of large area devices. J-V curves of reference and dual modified solar cells with device area of 70 mm2 .

3.1.4 Discussion

In summary, we present a dual interfacial modification approach by integrating large organic cations at both the electron and HTL interfaces. We find that modification of the bottom interface leads to an improved wettability, which eliminates the formation of nanovoids at the interface with the HTL. The modification of the top perovskite surface leads to its efficient passivation and a reduction in nonradiative recombination losses. These two different mechanisms for improved photovoltaic performance can be combined to achieve a simultaneous improvement in all the photovoltaic parameters. Moreover, the dual modification approach can be easily combined with the incorporation of ionic liquids into the perovskite active layer, thus leading to both efficient and stable devices, reaching a maximum power conversion efficiency of 23.7%.

3.2 Surface Imaging and quantifying non-radiative losses at 23% efficient inverted perovskite solar cells interfaces

In this work is studied a p-i-n solar cells, previously reported[40], despite the PV improvement, questions regarding the physics behind the modified interfaces are still open[41]. Issues regarding the completeness of the coverage of the passivating layer[42], whether a 2D perovskite is formed or not[26], and the possible effects on carrier extraction remain not fully understood. In a more general way, several studies focused on the recombination dynamics at the perovskite/selective interfaces by tracking the photoluminescence signal and its intensity[43–45]. For instance, the contributions of bulk and interfacial recombination currents were decoupled through the measurements of the quasi-Fermi level splitting (QFLS) of the individual layer by all-optical techniques[46]. Stolterfoht and co-workers used transient and absolute photoluminescence (PL) imaging to visualize non-radiative recombination pathways at modified perovskite/C60[47] electron transport layer. Here, we combine steady-state and time-resolved multidimensional photoluminescence imaging techniques to probe the main optoelectronic and transport properties of the optimized p-i-n devices. First, our results demonstrate that the Cl-PEAI and F-PEAI cations deposition result in a homogenous coverage of the perovskite surface. Second, we verify that no layered perovskite is formed. Moreover, we identify that interfacial passivation is the main mechanism driving the improvement of the device open circuit voltage (Voc), as the boost of QFLS and the reduction of surface recombination rate are observed only after PCBM (ETL) deposition. Instead, the introduction of the cations at the perovskite bottom interface (HTL/perovskite) helps in the perovskite crystallization process but does not significantly reduce the losses at that specific device interface, as demonstrated by the quantitative analysis of the QFLS.

3.2.1 Dual interfacial modified devices

The devices under investigation follow a *p-i-n* structure, as shown in Figure 44. The full stack includes: glass/Indium Tin Oxide (ITO)/Poly[bis(4-phenyl)(2,4,6-trimethylphenyl)amine (PTAA)/A-cation/perovskite/A-cation/[6,6]-phenyl-C_{61}-butyric acid methyl ester (PCBM)/Bathocuproine (BCP)/silver. Ionic salts, namely piperidinium salt $[BMP]^+[BF_4]^-$[34], were added to the mixed cation double halide composition ($Cs_{0.05}(FA_{5/6}MA_{1/6})_{0.95}Pb(I_{0.9}Br_{0.1})_3$). Three different types of cells were fabricated: a reference cell (Figure 44a) and devices with dual interfacial modification by F-PEAI and Cl-PEAI cations (Figure 44d).

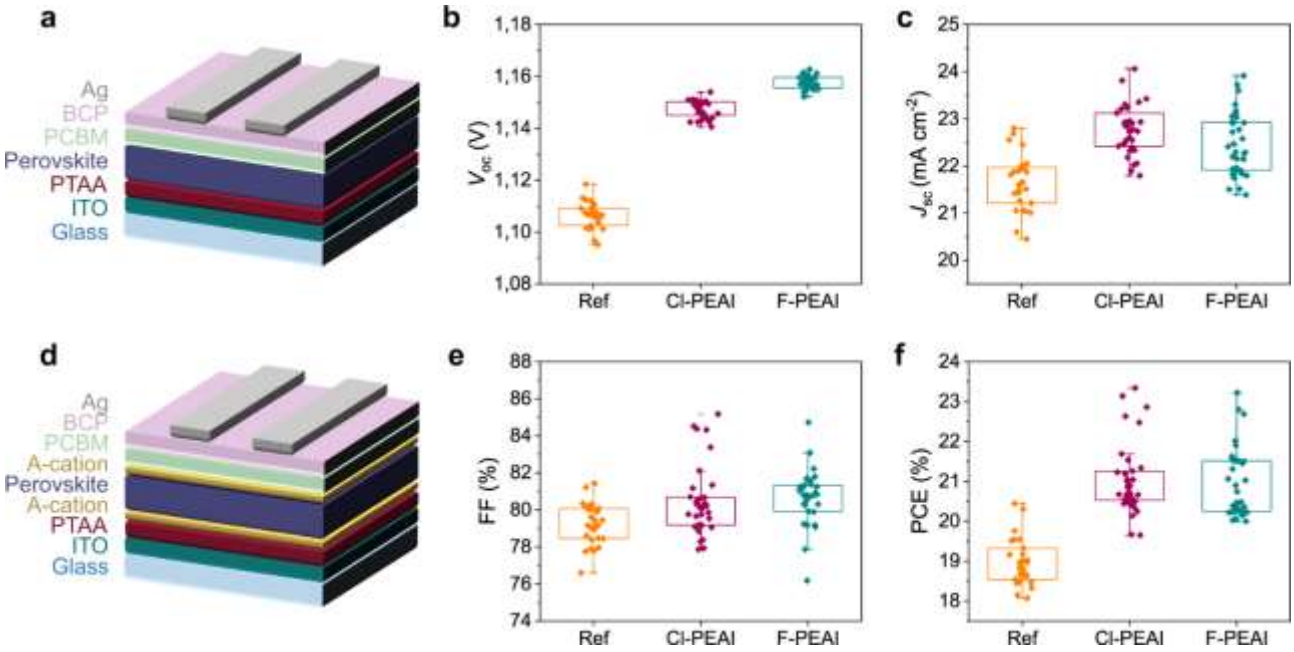

Figure 44 – a) Schematic of the reference samples d) Schematic of the A-cation p-i-n devices with dual interfacial modification. Photovoltaic characteristics of reference (orange), Cl-PEAI (purple) and F-PEAI (teal blue) devices. b Open circuit voltage (Voc). c Short circuit current (Jsc). e Fill Factor (FF). f Power conversion Efficiency (PCE).

The cations, commonly used as precursor for 2D perovskite formation, were added in very low concentrations (of 0.5 mM) at the top interface, meanwhile 20 mM were added at the bottom interface. The use of such low concentrations did not lead to the formation of a 2D Ruddlesden-Popper (RP) phase[40], as confirmed by XRD analysis reported in Figure 45, showing the characteristic perovskite reference peaks. However, as recently reported by Gharibzadeh et al[36], 2D organic cations can be also employed to passivate both grain boundaries and interfacial defects in *p-i-n* configuration devices, allowing to achieve a substantial enhancement of the device performances.

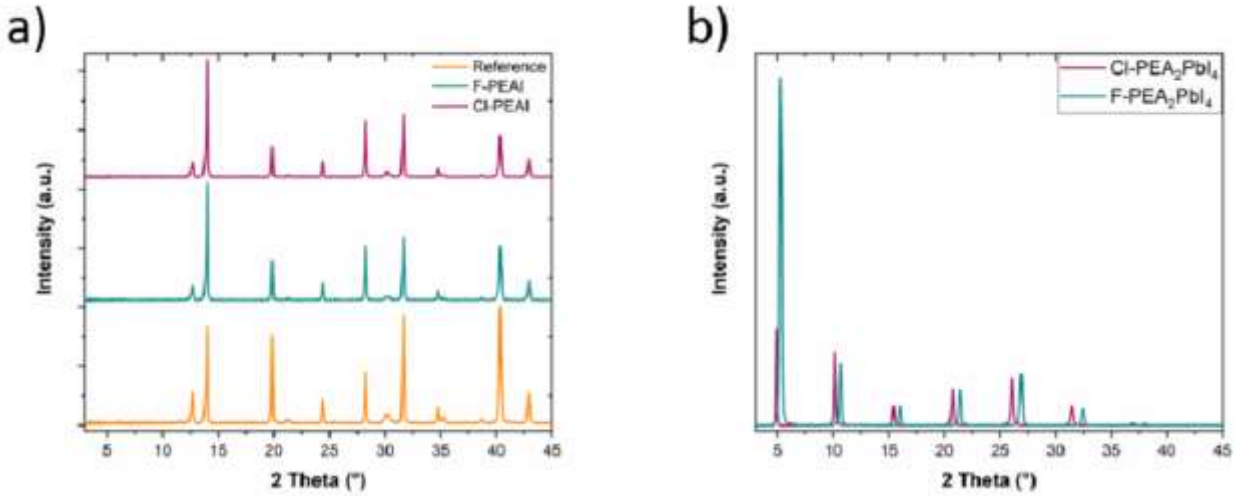

Figure 45 – a) XRD spectra of 3D perovskite thin films thin film deposited on ITO/PTAA/Cation substrates for reference and after Cl-PEAI and F-PEAI addition on top of the 3D and b) pure 2D perovskite Cl-PEA$_2$PbI$_4$ and F-PEA$_2$PbI$_4$

In this case the use of the top and bottom modification with the large organic cations is meant to improve the interfaces between the perovskite and the selective charge transport layers by simultaneously reducing the defect density and therefore the non-radiative recombination. The main photovoltaic characteristic parameters for the reference cell and the A-cations devices are reported in Figure 44b, c, e and f. The addition of the cations induced an increase of all the main photovoltaic characteristics. The PCE of the devices in which both absorber interfaces were modified by A-cations is clearly enhanced, exhibiting values up to 23.34% for the Cl-PEAI and 23.22% for the F-PEAI. In particular, we can note a clear increase of the V_{OC} from 1.10 V for the reference to 1.15 V using Cl-PEAI and exceeding 1.16 V using F-PEAI, which corresponds to a tenfold decrease of the dark current, i.e. of the carrier recombination rate. The current also slightly improved, in contrast with some previous observations in the literature, where the full formation of a 2D perovskite layer was acting as a blocking layer[26]. Remarkably, fill factor reached values up to 85 % on the Cl-PEAI and F-PEAI devices, within the highest ever reported for halide perovskite solar cells. Also, the devices do not show any hysteretic behavior, as is shown in Figure 46.

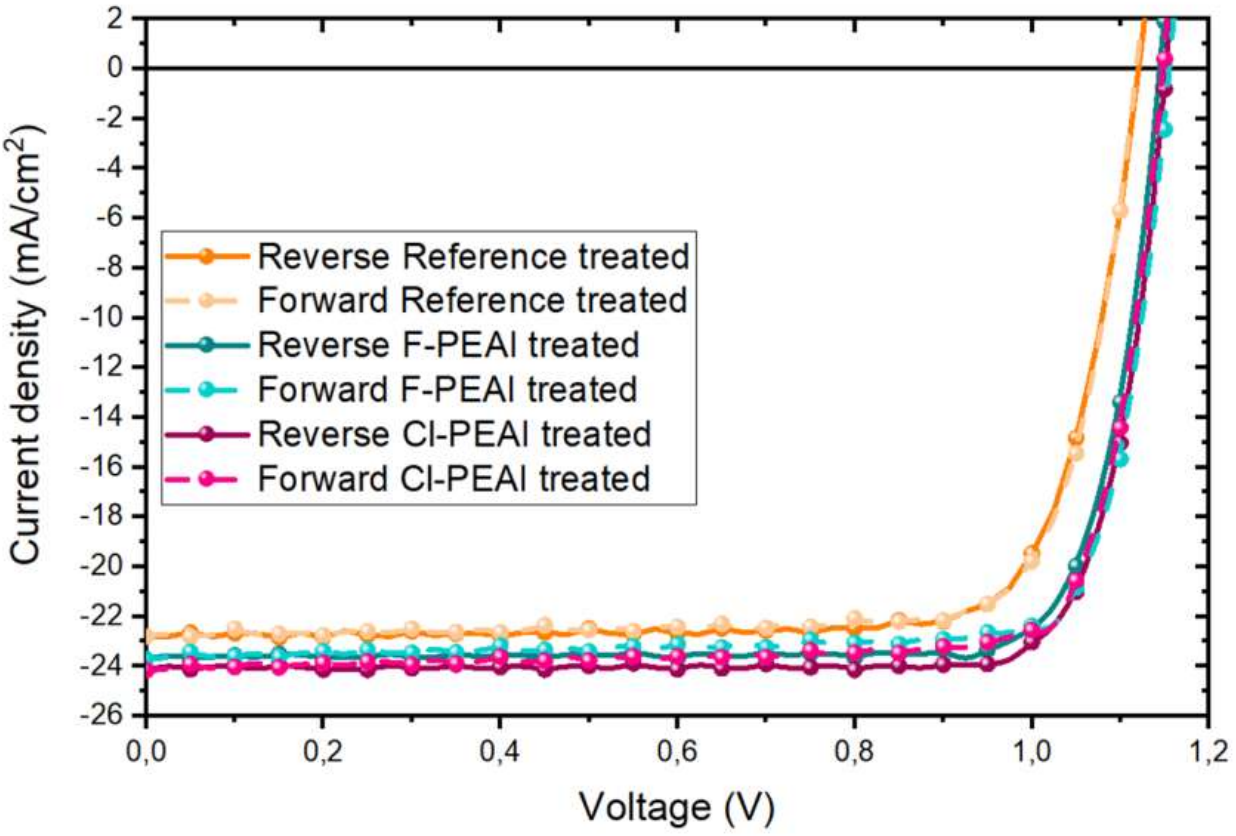

Figure 46 – J/V curve of the reference device and Cl-PEAI and F-PEAI passivated devices.

Table 4 – PV parameters of the reference, F-PEAI treated and Cl-PEAI treated devices

	Jsc (mA/cm^2)	Voc (V)	FF (%)	$FF_{pseudoIV}$ (%)	FF_{id} (%)	η(%)	$\eta_{pseudoIV}$ (%)	η_{id} (%)	$\Delta FF_{pseudoIV}$ (%)	ΔFF_{id} (%)	Rs (Ohm*cm^2)	Rsh (Ohm*cm2)
Reference	21.78	1.11	80.71	84.84	90.17	19.51	20.51	2179	4.13	9.46	0.608	3760
F-PEAI treated	23.42	1.17	83.23	86. 61	90.17	22.81	23.73	24.69	3.38	6.94	0.064	3200
Cl-PEAI treated	23.79	1.15	83.55	86.22	90.17	22.86	23.59	24.66	3.06	6.62	0.182	3600

3.2.2 Quantification of non-radiative losses at the interfaces

To better understand the origin of this evident improvement in terms of device performances we employed multi-dimensional photoluminescence and analyzed the datasets by employing physical models to quantify the key parameters governing the carrier recombination and transport. Specifically, we used two different set-ups to investigate both steady-state and transient regimes, namely a Hyperspectral Imager (HI)[48] and a Time Resolved Fluorescence Imaging (TR-FLIM)[49] set-up. Photoluminescence (PL) spectrum images were acquired by using a blue laser (405 nm) and illuminating the samples from the thin films side to avoid optical artefacts induced by the glass. We acquired a series of PL calibrated maps of neat perovskite thin films deposited on glass, half devices (glass/ITO/PTAA/perovskite) and full devices without the silver top electrode (glass/ITO/PTAA/perovskite/PCBM/BCP) of reference and Cl-PEAI or F-PEAI samples. Notably, the A-cations samples do not exhibit any 2D perovskite emission peak, as shown in Figure 47.

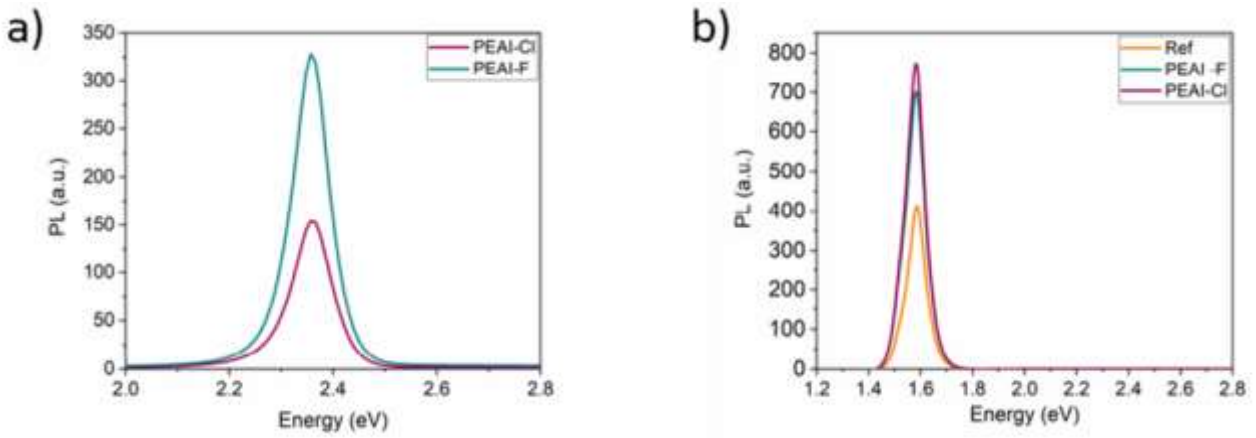

Figure 47 – a) PL spectra of 2D perovskite thin films showing an emission peak at approximately 2.35 eV. b) PL spectra for neat perovskite thin films deposited on glass. The spectra were recorder in the range going from 1.4 eV to 2.8 eV. No characteristic peak from 2D perovskite can be observed in the range 2.0 – 2.6 eV when F-PEAI and Cl-PEAI were added at the absorber interfaces.

The lack of a 2D perovskite formation is thus further confirmed, corroborating the XRD measurements. The spatially averaged and absolutely calibrated values of each map were fitted by using a model based on Planck's law[50,51,52] (see Figure 48 for PL spectra and fits of full devices), allowing to determine the QFLS values for eac set of samples, reported in Figure 48b and in Table 5. In Table 5 we also report the radiative quasi–Fermi level splitting ($\Delta\mu_{rad}$) and the radiative open circuit voltage (V_{OCrad}). The $\Delta\mu_{rad}$ is defined as:

$$\Delta\mu^{rad} = kT \cdot ln\left(\frac{I_{ph}}{q\Phi_{em}}\right) \quad (72)$$

where I_{ph} is the photocurrent due to the considered illumination and kT the thermal energy of the charge carriers and q is the elementary charge. The term ϕ_{em} is the PL emission of the absorber in thermal equilibrium with its surrounding at 300 K. It means that only the thermal photons emitted in the dark by the surrounding excite the device, which in return emits the very minimum PL photons flux possible. This PL flux depends on the bang gap energy, the temperature, and the absorption coefficient, which is affected by the defect density.

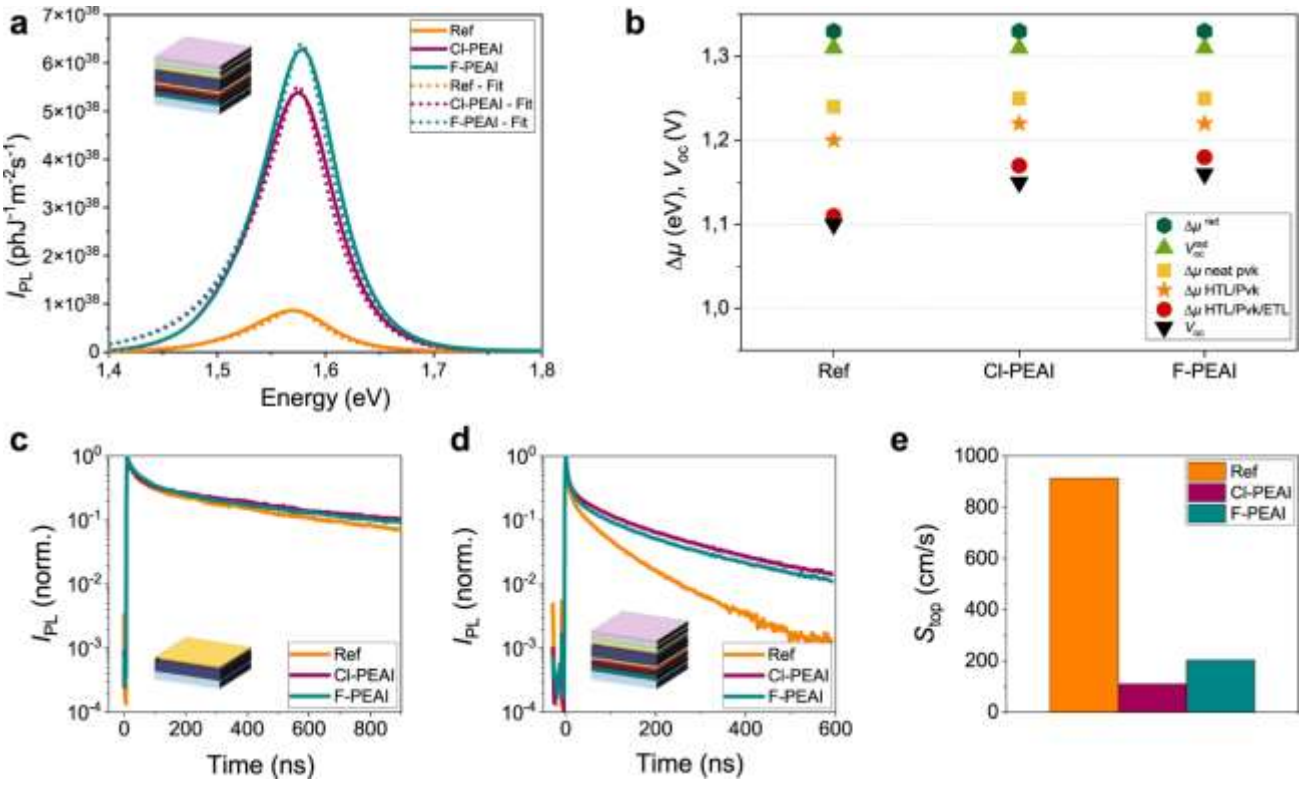

Figure 48 – Spatially averaged photoluminescence analysis in the continuous wave and time-resolved regime. a Photoluminescence average spectra and corresponding fits acquired on the stack glass/ITO/PTAA/perovskite/PCBM/BCP samples. PL spectra were acquired on reference (orange), Cl-PEAI (purple) and F-PEAI samples (teal blue). b QFLS values extracted from PL spectra for neat perovskite, half cells and full devices compared with radiative QFLS Δμrad, open circuit voltage Voc and radiative open circuit voltage Vocrad. TR-FLIM (spatially integrated) decays acquired at 1011 ph.cm−2 fluence for c perovskite layers deposited on glass, top illumination and d full cells without top bottom electrode, top illumination. e Comparison of the fitted top surface recombination rate on full devices

Table 5 – Values of radiative QFLS Δμrad; QFLS Δμ for the different stacks (neat perovskite (pvk), half cells (glass/ITO/PTAA/ pvk) and full stacks (glass/ITO/PTAA/pvk/PCBM/BCP)); Vocrad and Voc for reference, Cl-PEAI and F-PEAI samples.

Sample	$\Delta\mu^{rad}$ (eV)	Δμ pvk (eV)	Δμ HTL/pvk (eV)	Δμ HTL/pvk/ETL (eV)	V_{oc}^{rad} (V)	V_{oc} (V)
Reference	1.33	1.24	1.20	1.11	1.31	1.10
Cl-PEAI	1.33	1.25	1.22	1.17	1.31	1.15
F-PEAI	1.33	1.25	1.22	1.18	1.31	1.16

Moreover, we defined the radiative open circuit voltage V_{OC}^{rad} as:

$$V_{OC}^{rad} = \frac{kT}{q} \cdot ln\left(\frac{J_{SC}}{J_{0rad}}\right) \quad (73)$$

Where kT is the thermal energy of the charge carriers, q is the elementary charge, Jsc is the short-circuit current density of the solar cell and J_{0rad} is the radiative current[53,54].

$$J_{0rad} = q \int EQE(E)\, \Phi_{BB}^{300K} \frac{kT}{q} dE \quad (74)$$

with EQE being the external quantum efficiency of the full devices.

We considered the radiative QFLS ($\Delta\mu_{rad}$) as the radiative limit for the optical measurements and the V_{OCrad} as the upper limit for the open-circuit voltage measured by electrical characterization. The small difference of the values determined for the two limits arises from the fact that the V_{OCrad} depends not only on optical properties of the absorber and the radiative recombination but also from the collection and the injection of carriers.

We obtained values of QFLS for neat perovskite thin films equal to 1.24 eV for the reference sample and 1.25 eV for the two A-cations samples, corresponding to 80–90 meV losses if compared to the radiative QFLS ($\Delta\mu_{rad}$) that is equal to 1.33 eV in all cases. Interestingly, the main impact of the organic cation passivation is observed for full devices. In this case, the difference between reference and A-cations containing samples is in the range of 60–70 meV, proving that the cations have drastically reduced the non-radiative recombination at the interface absorber/ETL. Conversely, when considering neat perovskite or half devices the addition of the cations resulted in an improvement of only 10–20 meV. Therefore, the main passivation mechanism acting relates to the interfacial passivation at the interface absorber/ ETL. The introduction of the organic cations at the interface HTL/absorber favored the perovskite crystallization on the PTAA surface but did not drastically reduce the losses at that interface. It is worth noting that the interface perovskite/PCBM appears to be particularly critical for device optimization. The fast recombination observed at this specific interface represents a major loss mechanism for solar cell operation[55]. Moreover, we linked the QFLS of full devices to the V_{OC} measured on full devices[56] by finding a good agreement between the two values, thus confirming the direct relationship between optical and electrical measurements. A similar approach to evaluate the recombination processes of 3D-2D interfaces in a n-i-p architecture was performed by Sutanto et al.[26], where the interfacial passivation was considered as the main process affecting the losses. However, cation interfacial passivation, not only reduce the non-radiative recombination, but also favour the carrier extraction that, on the contrary, is limited in the case of full 2D perovskite formation at the interfaces, acting as a barrier for the photo-generated carriers[26]. Finally, we determine the total losses due to non-radiative recombination in full devices by comparing the radiative voltage radiative voltage V_{OC} rad with the measured V_{OC} ($\Delta V = V_{OCrad} - V_{OC}$). In the reference sample ΔV_{ref} is equal to 0.21 eV, while in the A-

cations devices ΔV corresponds to 0.16 eV in the case of Cl-PEAI and to 0.15 eV in the case of F-PEAI, thus confirming the beneficial role played by the addition of the cations on the charge losses.

To gain further insights regarding the carrier dynamics, we performed TR-FLIM analysis on two sets of samples: (i) thin films on glass and (ii) full cell devices (without the Ag metallic layer to allow for illumination from both sides). For both sets of samples, we analyzed a reference sample with only bulk perovskite as well as Cl-PEAI and F-PEAI samples. The experiments were performed using a wide field illumination via a pulsed 532 nm laser with repetition rate of 40 kHz. For each sample, the fluence of the laser was varied from low (~1011 ph.cm^{-2}) to high level (~1.5 × 1012 ph.cm^{-2}) and all the samples were measured with both top and bottom illumination (and light collection).

Decays averaged over the image for low fluence (~1011 ph.cm^{-2}) by illuminating the samples from the thin films side are presented in Fig. 48c (neat perovskite) and 48d (full devices). In the case of bare absorbers, the three decays are very similar, whereas for the full devices, the samples with the added A-cation layers show slower decay than the reference. We estimate that the slightly higher PL level obtained for the Cl-PEAI bare absorbers is not discriminating enough to conclude that this cation has a better passivation effect than its F-PEAI counterpart. Slower decays of multilayer samples do not necessarily imply better devices as passivation layers could hinder the amplitude of the current of charges flowing out of the cell. In this case, considering also that the short-circuit currents slightly increased upon modification with the A-cations (see Figure 44c), we can conclude that this passivation approach allows to reduce non-radiative recombination at the perovskite-charge transport layer interfaces while allowing for high currents to flow. Transient measurements thus confirmed that the passivation plays a key role only at the perovskite-charge transport layer interface, as also observed in the steady-state study. Importantly, the time-resolved analysis also proves that high non-radiative recombination is responsible for the fast decay of the reference cell of Figure 48d, that therefore cannot be attributed to carrier extraction as sometimes reported in the literature[57,58].

Next, we treated the datasets by using drift-diffusion model in order to quantify the induced passivation. However, fitting decays of multilayer samples remains challenging, as an incorrect modelling of the layer stack, of the band alignment or of the boundary conditions can easily lead to data misinterpretation[44,59]. To overcome this issue, we chose to fit the simplest model possible, that is based on a thin film without the neighboring extracting layers. Figure 49 represents the fitting results of the cells' decays, the green dotted line is the fitted model, while the colored curves correspond to the experimental data.

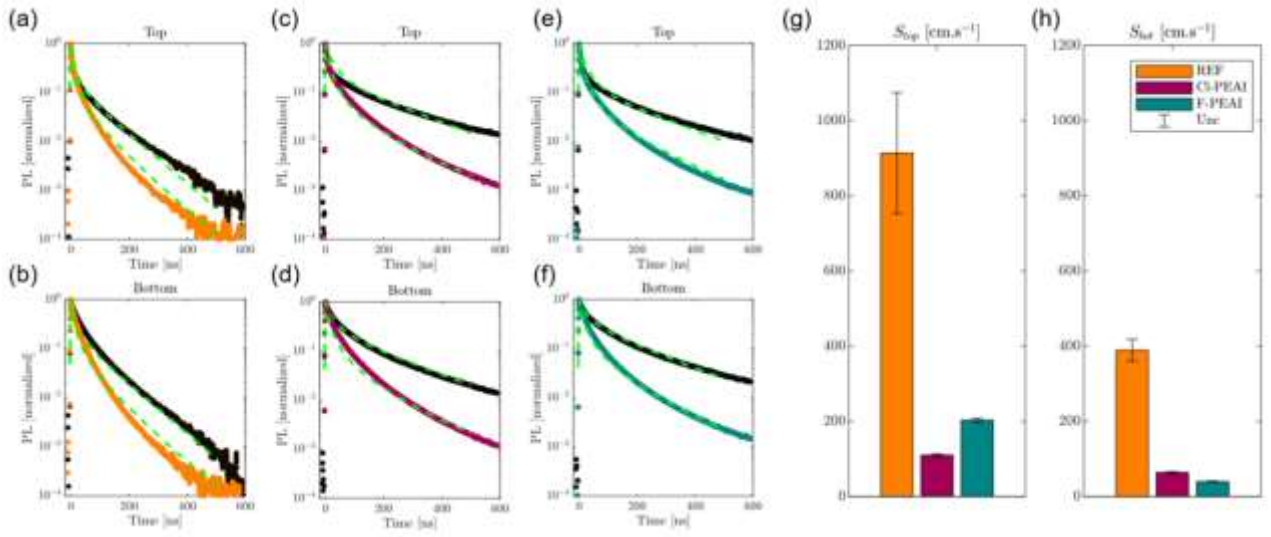

Figure 49 – Fitting result of the decays obtained on full-cells. Green dotted line, fitting model. Colored dots, experimental data. The dark curves is the low fluence one, while the bright one corresponds to high fluence. (a-b) Reference cell (with no passivation), top and bottom sides (c-d) Cell with added Cl-PEAI passivation (e-f) Cell with added F-PEAI passivation. For the 3 samples, only one model represents the whole dataset (2 fluences, 2 sides). (g) Fitted value of top surface recombination velocity (h) Fitted value of bottom surface recombination velocity.

We fit a unique drift-diffusion model to represent simultaneously four curves, i.e. decays acquired in bottom and top configuration at low and high fluence. The fitted parameters are the top and bottom surface recombination velocities – all the other parameters are fixed. We consider the bulk non-radiative recombination to be negligible as compared to surface recombination and assign all non-radiative recombination to the surfaces. The fitting results for bottom surface recombination velocity on full devices are presented in Fig. 48d. We observe a drastic reduction of the recombination velocities at the top surface (S_{top}) for the two passivation strategies. In particular, S_{top} was reduced by a factor varying from nine to five going from ~900 cm/s for the reference to ~110 cm/s and ~200 cm/s for the Cl-PEAI and F-PEAI samples respectively, as shown in Table 6. For unpassivated classical semiconductors, surface recombination velocities are of the order of 10^5–10^6 cm/s [60–62], while passivated surfaces may reach low values in the range of 10–10^2 cm/s[60,63,64]. For perovskite films, even unpassivated, wecaco[65,66] and others[60,67] have found surface recombination velocities of the order of 10^3 cm/s which are fully compatible with our present analysis. Again, the TR-FLIM results are consistent with those obtained via the hyperspectral studies, showing that the passivation mainly takes place at the perovskite/ETL interface.

Table 6 – Top and bottom fitted interface recombination velocity for reference and A-cations full cells.

Device (fuel cells)	**S_{top} (cm/s)**	**S_{bot} (cm/s)**
Reference	914 ± 160	389 ± 29
Cl-PEAI	110 ± 160	64 ± 2
F-PEAI	203 ± 160	39 ± 2

3.2.3 Quantitative optical microscopy analysis

It is noteworthy that the passivation of the top surface is achieved by incorporating the A-cations into the antisolvent used for triggering the perovskite layer crystallization, thus raising the question regarding the homogeneity of passivation obtained by this method. In order to better assess the homogeneity of the passivation over the samples surface, we mapped the optoelectronic properties by spectrally and temporally resolved photoluminescence imaging analysis on the full stack without the silver rear electrode. We first fitted the PL spectra pixel-by-pixel[65,68] by using the model proposed by Katahara and Hillhouse[69,70] to extract key physical parameters like the bandgap energy (Eg), the quasi-Fermi levels splitting (Δμ or QFLS) and the Urbach energy (Eu) from absolutely calibrated spectral images. The maps of the QFLS are shown in Figure 50a–c. All the samples, reference and most importantly cation modified samples, show a good homogeneity with a standard deviation in the order of 0.006 eV. Moreover, no areas with values of QFLS comparable to pure 3D cells, i.e. in the range of 1.110 ± 0.013 eV, can be observed on the Cl-PEAI and F-PEAI samples, proving the uniformity of the passivation effect induced by the cations. The introduction of the large cations has thus produced a clear reduction of non-radiative losses and importantly we demonstrate that the passivating agents act uniformly on the whole surface of the solar cell. However, in the three cases, small spatial fluctuations in the order of few meV in the 10 μm range are distinguishable. These minor inhomogeneities may be due to the spin-coating process. In Figure 50d–f we investigate the variations of the Eu which again exhibits a good homogeneity. The determined values are in line with Eu values reported in the literature and measured by different characterization methods[71].

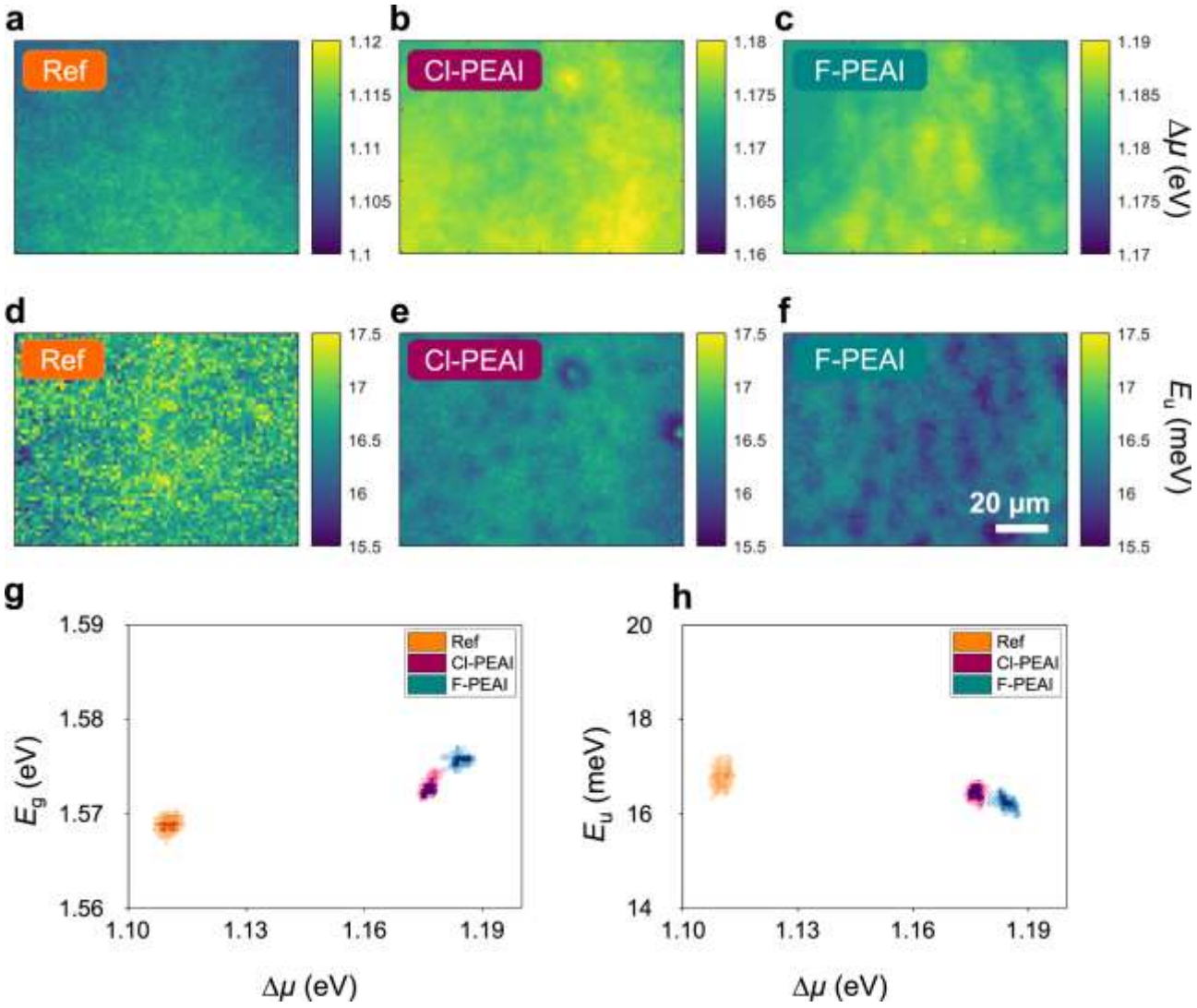

Figure 50 – Continuous wave photoluminescence imaging analysis. Hyperspectral measurements on the stack glass/ITO/PTAA/perovskite/BCP/PCBM. quasi-Fermi level splitting (Δμ) maps for a reference sample, b Cl-PEAI and c F-PEAI samples. Urbach Energy maps for d reference sample, e Cl-PEAI and f F-PEAI samples. g Correlation between energy gap and QFLS. h correlation between Urbach Energy and QFLS. The scalebar applies to all images.

To highlight the correlations between the different optoelectronic properties, as well as the statistic distribution of the determined parameters over the maps, we report the correlation between Eg and QFLS and between Eu and QFLS measured at each pixel, as shown in Figure 50g, h. All the physical parameters, namely Eg, QFLS and Eu, have a small statistical dispersion. The introduction of the A-cations results in a minimal increase of the gap of the material in the order of few meV but significantly impacts the QFLS that shows a substantial raise of its average value from 1.11 eV up to 1.18 eV. A very small variation of Eu of ~1 meV is observed when comparing the reference to the A-cations passivated devices. Moreover, this analysis suggests that the addition of the cations does not significantly affect the bulk recombination kinetics of the absorber as QFLS (in the case of bare absorbers), Eg and the Eu, do not vary significantly after the A-cations addition.

Finally, we wanted to further confirm the homogeneity of the A-cation deposition as well as their role in the interface physics. To do so, we used TR-FLIM acquisitions to map the local decay times, often called

"lifetime", for the three full stacks (glass/ITO/PTAA/perovskite/BCP/PCBM), as shown in Figure 51a–d. In general, the definition of "lifetime" is ambiguous, as it does not represent an intrinsic property of the material (e.g. it is dependent on the excitation conditions), and does not always correlate well with the electrical figures of merit, such as the open circuit voltage[43]. For these reasons we employ here the term decay time. If we place ourselves in the correct setting - after the carrier distribution has homogenized in depth and with low radiative recombination - the decay time of PL is a measure of the non-radiative recombination. In the case of triple cation mixed halide perovskite thin films this corresponds to a few tens to one hundred nanoseconds after the laser pulse[72]. We use then the decay times to map the non-radiative recombination in our devices. To get a high signal to noise ratio for the images we used the high fluence (1.5×10^{12} ph.cm^{-2}) acquisitions, as reported in Figure 51a–d. Here the decay time is defined as the inverse slope of the logarithm of the local decay fitted between 90 ns and 500 ns after the laser pulse. Figure 51a–c are thus representative of the non-radiative recombination in the devices. Overall, an excellent homogeneity was achieved at the 1 mm^2 scale for the F-PEAI and Cl-PEAI samples. The histograms of Fig. 51d display that the difference between reference and modified samples in terms of non-radiative recombination is statistically significant. The mean decay time on the maps extracted from the high fluence acquisitions are found to be 84.6 ns for the reference, 107.9 ns for the F-PEAI and 117.35 ns for Cl-PEAI. The images of the passivated layers show a slightly wider distribution of decay time, compared to the reference sample with a standard deviation of 6.7 ns for the reference and 8.7 ns and 8.2 ns for the F-PEAI and Cl-PEAI, respectively. This analysis provides us with an approximate estimate for the uncertainty and noise level on the images. The decay time maps thus show the homogeneity of the interfacial cation addition treatment resulting in a uniform improvement of decay times for the A-cation modified devices, further confirming the reduction of non-radiative recombination.

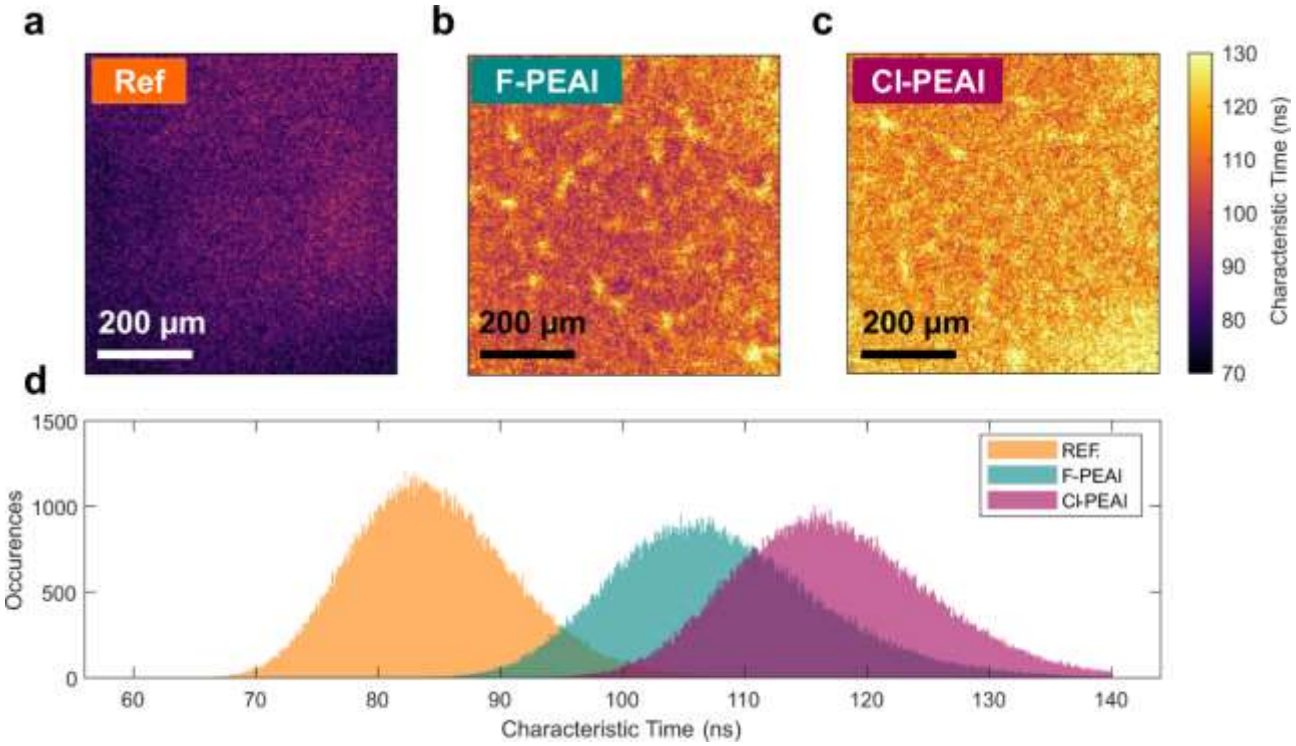

Figure 51 – Time-resolved photoluminescence imaging analysis. a–c Map of decay time obtained on full-stacks (glass/ITO/PTAA/perovskite/BCP/PCBM) for the high fluence (1.5 × 10^{12} ph.cm^{-2}) acquisition. The homogeneity of the A-cations devices is comparable to the neat reference cell. d Histogram of the maps, showing the passivation effect of the layers.

Moreover, we provide the decay times for the full stacks when the carrier density of the transient experiment is ~10^{15} cm^{-3}, which is the order of magnitude of carrier density expected at 1 Sun continuous illumination condition for perovskite devices close to the radiative limit[73]. To obtain these values of decay time, we used a procedure for the low fluence (10^{11} ph.cm^{-2}) acquisitions that yields decay times of 102 ns (±7%) for the reference cell, 254 ns ±(3%) for the Cl-PEAI cell and 261 ns (±3%) for the F-PEAI cell. For the low fluence dataset, the local signal to noise ratio of the maps is too low for the local determination of the decay time and therefore we do not show maps for this illumination condition.

3.2.4 Conclusion

In conclusion, we have investigated the interface recombination dynamics related to an emergent passivation approach in the field of perovskite solar cells based on the introduction of large cations at the absorber interfaces by coupling electrical and optoelectronic characterization methods and modelling. In particular, we demonstrated that the introduction of large organic cations such as Cl-PEAI and F-PEAI resulted in a drastic reduction of interfacial recombination processes leading to PCE up to 23.34%, one of the highest ever reported for a p-i-n architecture. Importantly, we proved that this passivation approach does not significantly act on the surface defects of the absorber layer but drastically reduce the non-radiative recombination at the interface perovskite/PCBM. Indeed, the major improvement in terms of QFLS was observed after the deposition of the ETL, with an increment from 1.11 eV to 1.18 eV for passivated devices. Conversely, in the case of neat perovskite thin films the QFLS remained almost constant after the two cations deposition. The same behaviour was also observed for transient measurements that showed identical decays in the three

cases. Finally, photoluminescence maps and decay times maps of full devices proved that the cations were uniformly deposited over the perovskite surface at the micrometer scale and that the main bulk optoelectronic properties of the absorber such as the energy gap and the Urbach energy were homogenous at a local level. This work provides insights into the processes occurring at the interfaces of highly efficient perovskite solar cells, which are fundamental for further progress in the field and makes this passivation method extremely promising to approach the theoretical limit of perovskite devices.

3.3 Accelerated Thermal Aging Effects on Carbon-Based Perovskite Solar Cells: A Joint Experimental and Theoretical Analysis

In this work, we address this issue, monitoring the effect of thermal aging on state-of -the-art C-PSCs by imposing a prolonged (27 days) temperature cycling stress, with the intent to mimic outdoor conditions. The measured device current–voltage characteristics are modeled by an advanced iterative fitting method based on the single-diode equation with series (R_S) and shunt (R_{SH}) resistances. Below 50°C the C-PSCs are stable, and switching to 80°C a slow device degradation takes place. The fitting model suggests the reason behind this is a net decrease of the device R_{SH}, whereas the R_S is unaltered. This suggests that deterioration starts from interfacial contacts, while further structural and morphological analysis reveal no degradation of the perovskite bulk layer.

3.3.1 Result and discussion

A series of semi encapsulated C-PSCs (sandwiched between two sheets of glass and an encapsulant but without an edge sealant) was measured under a defined aging protocol consisting of a temperature cycle between 50 and 80 °C, keeping a relative humidity (RH) = 72%. The temperature regimes chosen are respectively below and above the phase transition temperature of the active material, which occurs around 54 °C and it is fully reversible. The test was run for 648 h (27 continuous days) alternating between stress and recovering periods, as indicated by the red and blue slots in Figure 52a.

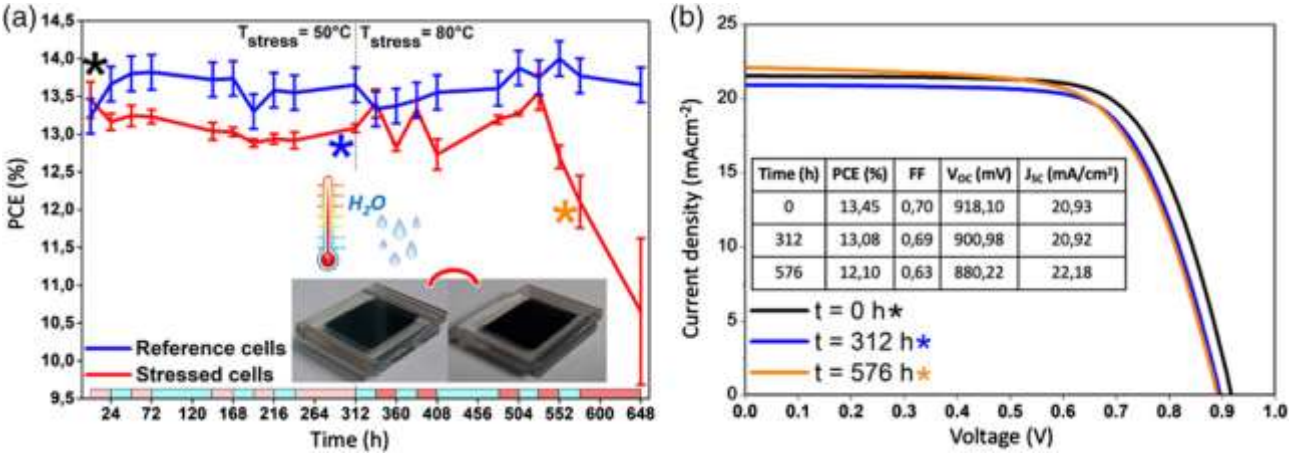

Figure 52 – a) Stability measurements monitoring the PCE versus time for a solar cell under thermal and humidity cycling (red line) compared to a reference cell kept in dark and ambient conditions (blue line). Note that the J–V measurements were done immediately after the aging. Red sections at the bottom indicate stress periods (light red at 50 ° C and dark red 80 ° C) and light blue sections indicate recovery periods. Humidity was kept constant at 72% RH. Three samples with the same architecture were measured each day; the differences in the PCE are indicated by error bars. The inset pictures are of cells before (left) and after (right) stress. b) Experimental current–voltage (J–V) curves measured at 1 sun illumination (AM 1.5 G spectrum) at t = 0 h (fresh) and after t = 312 h and t = 576 h of aging as indicated by the asterisks. In the inset are solar cell parameters (PCE, fill factor (FF), VOC, and JSC) of the device for the J–V curves.

During the recovering time, the cell was kept in dark and in ambient conditions (RH = 72%). At first glance, during the overall aging, the C-PSCs show an average decrease in PCE from an average value of 13.5% to

10.6%. On closer inspection, two behaviors were revealed. If the devices are kept at 50 °C, the PCE is stable. After switching to 80 °C, the PCE remains stable for 230 h and then abruptly reduces to 20% of the initial values. On the contrary, reference cells, kept in ambient conditions and in the dark, are stable for the whole time window, further confirming the high stability of this device architecture even in relatively high-humidity conditions. Figure 52b shows the corresponding current–voltage (J–V) characteristics of the solar cells at 0 h and after 312 and 576 h testing times, in forward scan. Upon aging, a remarkable reduction of the FF and of the open circuit voltage (VOC) is observed, as summarized by the device parameters listed in the table in the inset (see also Table 7 and Figure 53).

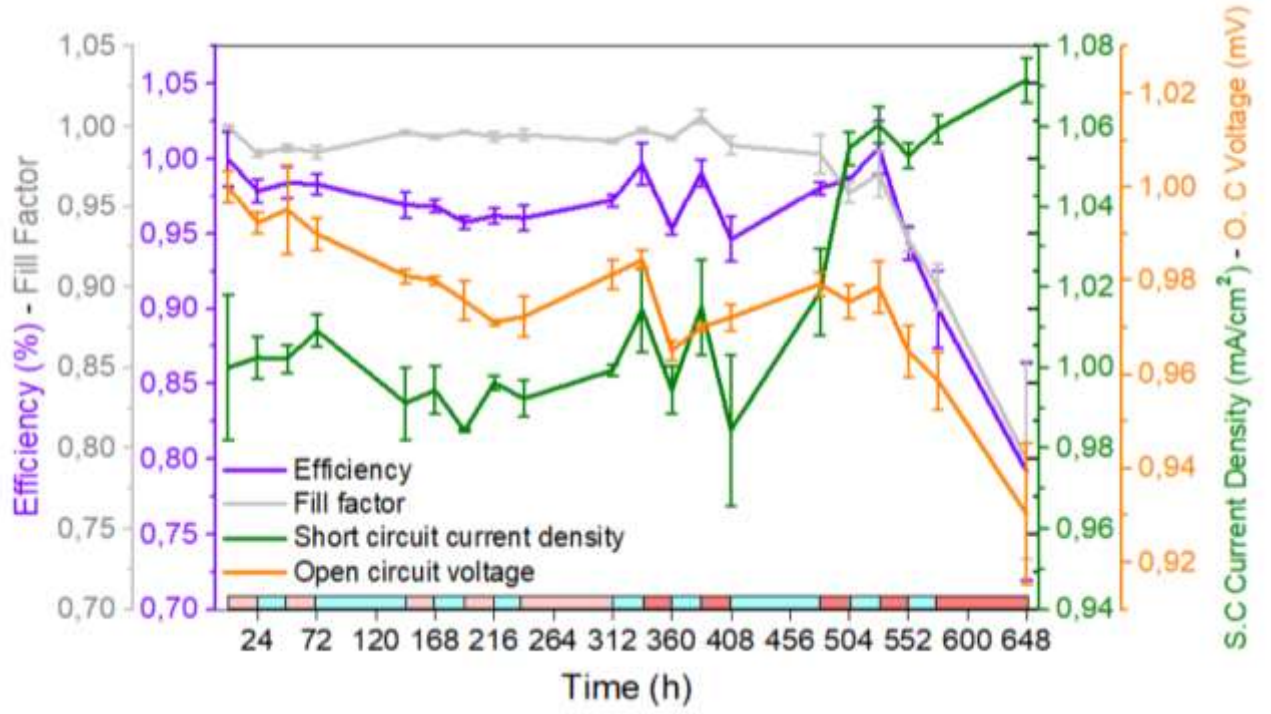

Figure 53 – Solar cell parameters (PCE, FF, VOC and JSC) normalized to their initial value and relative uncertainty (standard deviation) of the device for the J-V curves of Figure. 52b

Table 7 – Solar cell parameters (PCE, FF, VOC and JSC) and relative uncertainty (standard deviation) of the device for the J-V curves of Figure 52b

Time (h)	PCE (%)	σ (%)	Fill factor	σ	V_{OC} (mV)	σ (mV)	J_{SC} (mAcm^{-2})	σ (mAcm^{-2})
0	13,4543	0,23801	0,70014	0,00118	918,09668	3,047	20,93128	0,37795
312	13,08202	0,05461	0,69409	0,00072	900,9797	2,90887	20,91898	0,02821
576	12,10456	0,34812	0,63032	0,00987	880,22198	5,65219	22,17667	0,07232

The trend of the FF mirrors that of the PCE, being constant for the first half of the cycle and decreasing in the second, whereas the reduction of the VOC is uniform through all of the aging cycle. To understand which device parameters could be most affected by thermal stress, we tracked and modeled device operation and parameters by developing a customized advanced fitting procedure. The equivalent circuit is based on a

single-diode model. At a given illumination, the current/voltage relationship is given by Equation (62) derived from the Shockley equation where I_L, I_0, R_S, R_{SH}, q, n, k_B, and T are the photocurrent, the saturation current of the diode, the series resistance, the shunt resistance, the electron charge, the ideality factor, the Boltzmann constant, and the temperature, respectively. It is worth recalling that the R_{SH} is usually related to the leakage current across the surfaces involving pinholes, grain boundaries, and charge recombination processes,[74] and the R_S is reflected in the voltage drops and related to the conductivity of the layers and interfaces[75,76].The ideality factor is related to interfacial layers, transport, and recombination processes, directly affecting the R_{SH} and V_{OC}[77]. Ideality factors for PSCs are usually between 1 and 2 (closer to 2 if severe trap-assisted recombination under dark condition happens)[78,79]. To fit the J–V characteristics, the modeling program was implemented as schematized in Figure 54.

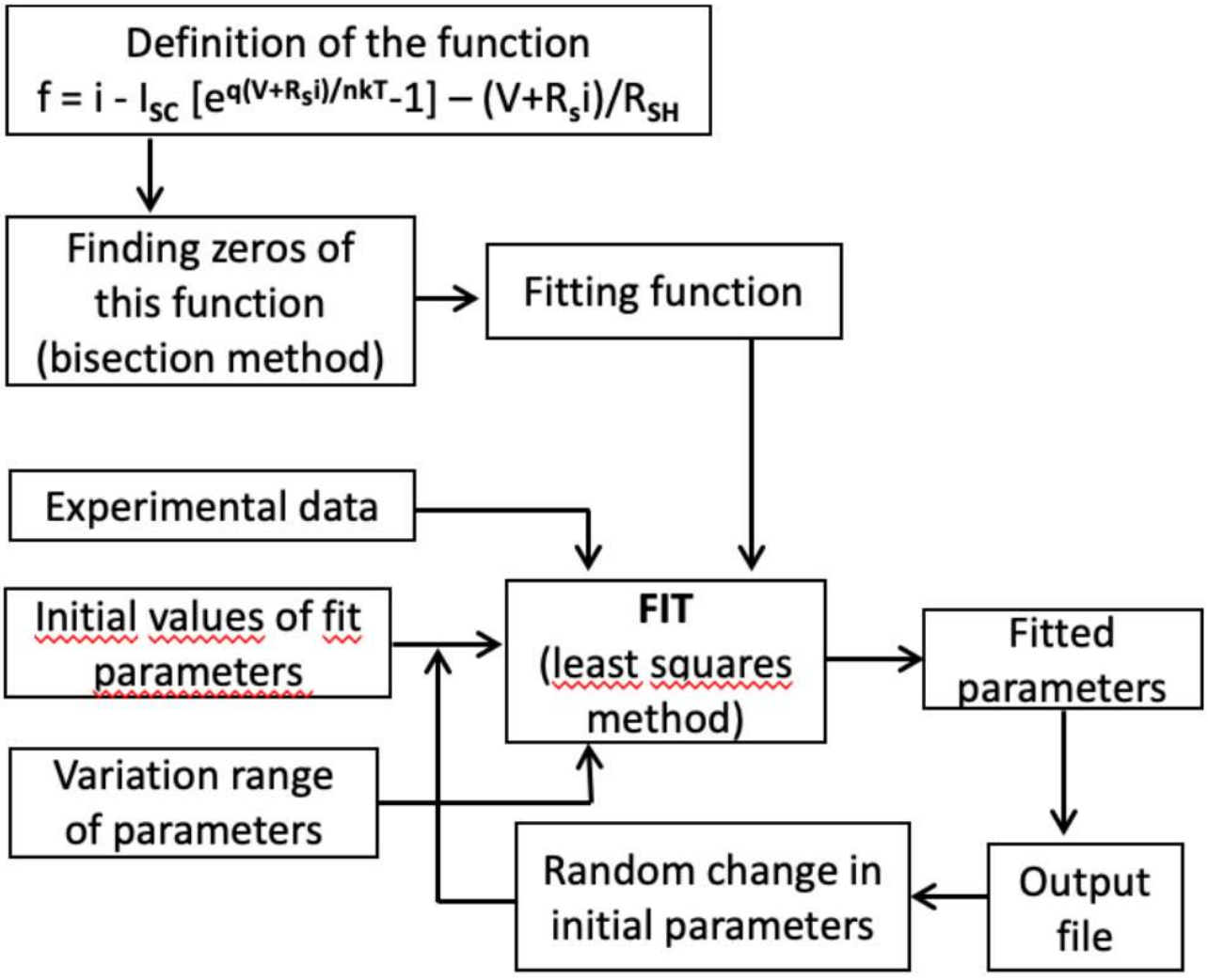

Figure 54 – Block diagram of the fitting procedure of the programme developed in Python.

First, due to the particular dependence on the current of Equation (62), we found zeros of the function (Equation (74)) using the bisection method.

$$f = J - J_L + J_0\left[exp\left(\frac{q(V + JR_s)}{nkT}\right) - 1\right] - \frac{V + JR_s}{R_{SH}} \quad (74)$$

Then, we properly chose the initial values of the fitting parameters and their variation range, determining the final values for the least-squares method. Notably, we could also randomly change the initial values of the parameters to leverage possible biasing throughout all the cycle, and to estimate the overall uncertainty in the final parameters. The estimated parameters for each cell are reliable and unbiased. From performing a "4-parameter fit"—i.e., a procedure in which all the parameters (n, I_0, R_S, R_{SH}) are fitted—we conclude that the reverse saturation current is the most variable parameter as it varies over an exponential scale (see also Figure 55c).

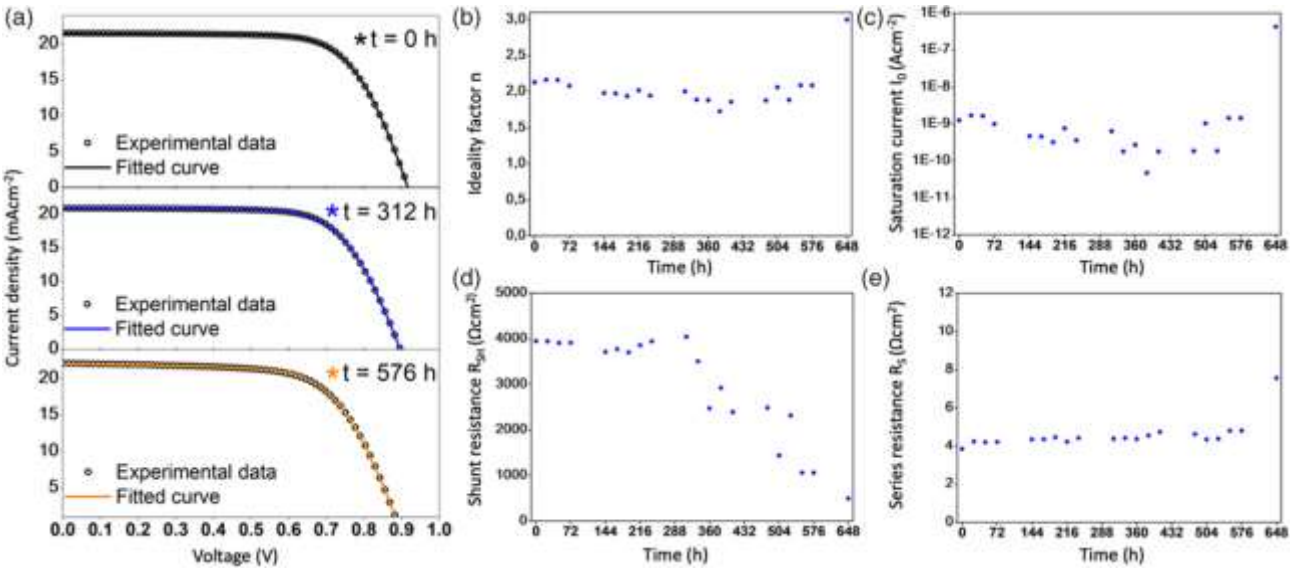

Figure 55 – a) Current–voltage characteristics curves at selected times (as in Figure 52b), superimposed with the fit. b–e) Parameters extracted from data fitting using the model described in the text showing (b) the ideality factor (n), (c) the reverse saturation current, (d) the shunt resistance, and (e) the series resistance. Note that the last point in the time window, corresponding to t = 648 h, is not at full convergence, probably due to the excessive degradation of the device.

To validate the robustness of the fit, we implemented an advanced version of the fitting procedure, consisting of a "three-parameter fit" or a "four-parameter fit." For the three-parameter fit (see Figure 56) we choose a fixed value for I0 and retrieve the remaining parameters (n, R_S, R_{SH}).

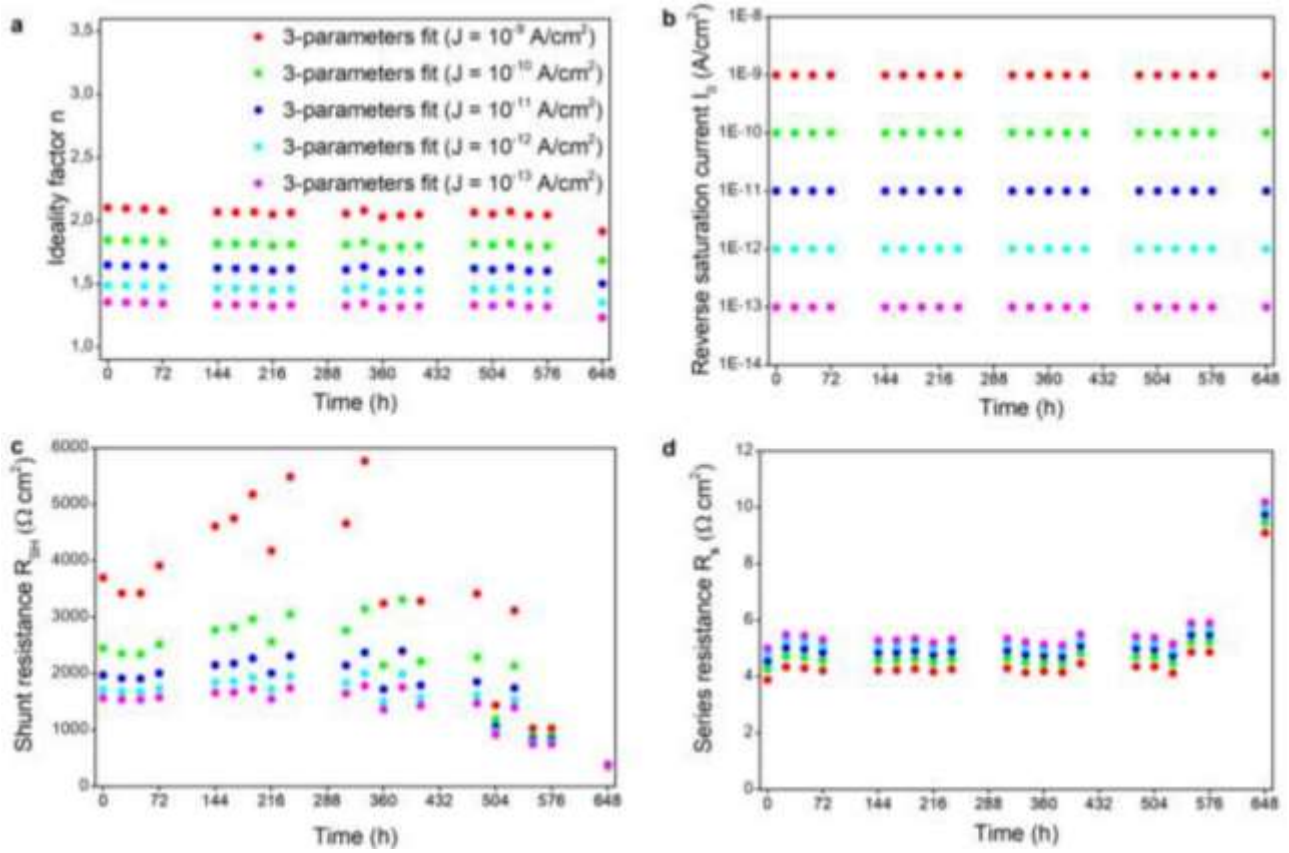

Figure 56 – Parameters extracted from data fitting using a 3-parameters fitting procedure (with J0 fixed): a. ideality factor (n), b. reverse saturation current, c. shunt resistance and d. series resistance.

As Figure 57, shows, the fitted curves match fairly well the experimental points, but the slight deviations are minimized when I_0 is fixed to the value determined from the four-parameter fit ($J_0 = 10^{-11}$ A cm^{-2}, Figure 57c).

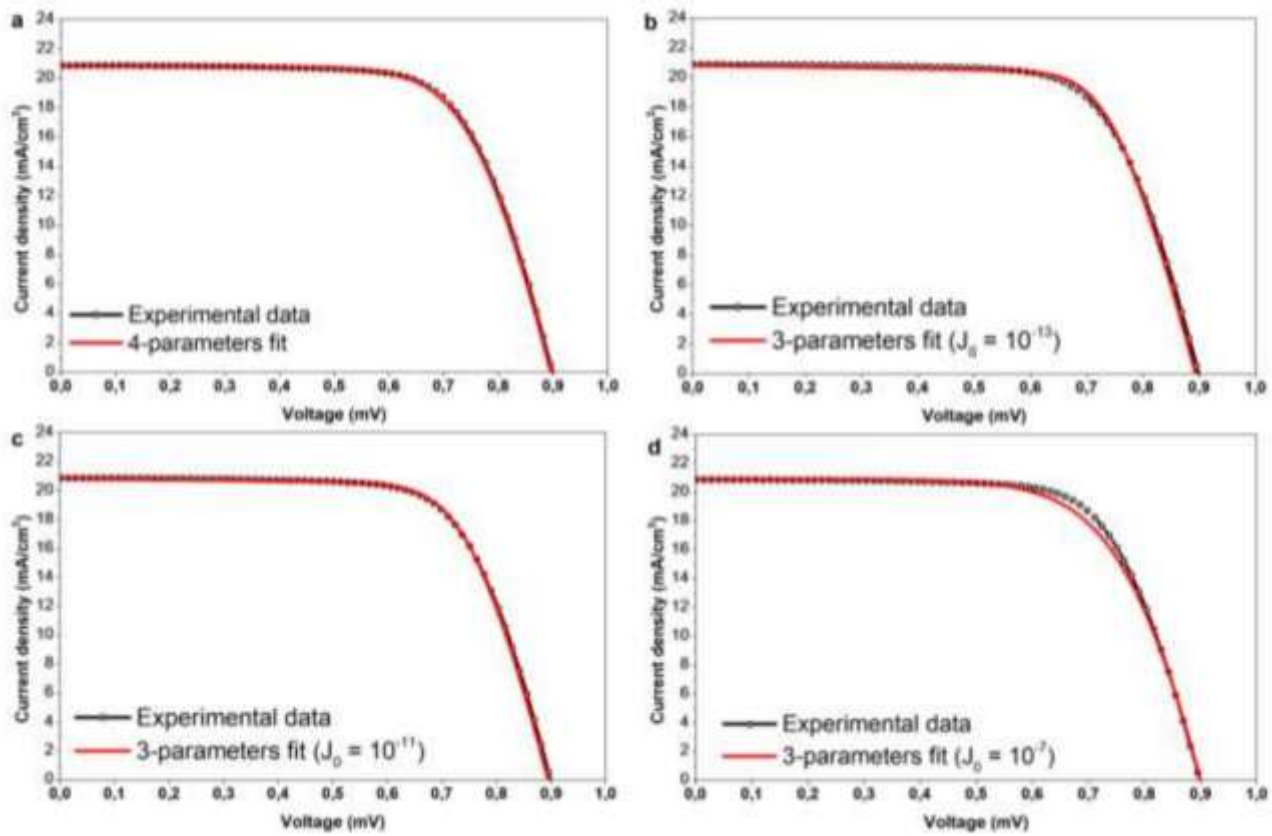

Figure 57 – Comparison beetween 4 (a) and 3-parameters fit (b-c-d) for a single J-V curve

Figure 55a shows the J–V characteristics curves at selected times (as in Figure 52b), superimposed with the fitted curves resulting from the four-parameter fit. We observe that the fit is in very good match with the experimental data, reproducing the whole set of data. Figure 55b–e shows the trend of the extracted parameters at different aging times in terms of (b) n, (c) I_0, (d) R_{SH}, and (e) R_S. From the fitting results we can observe that 1) the ideality factor varies between 1.7 and 2.2, in agreement with Tress et al.[78]; 2) the reverse saturation current varies from 10^{-11} to 10^{-9} (due to the strong sensitivity of I_0 to recombination processes), as shown in Figure 55c; 3) R_{SH} is stable for the first part of the cycle and then decreases by two orders of magnitude; and 4) R_S is barely affected throughout the entire cycle. The results point to a significant decrease in shunt resistance as the dominant factor responsible for device degradation. This suggests a minor effect of the aging on the bulk, while it indicates a severe impact on the device interfaces. Hereafter, we combine structural (X-ray Diffraction (XRD)), morphological (scanning electron microscopy (SEM)), and optical investigation to further elucidate the material properties before and after the aging test.

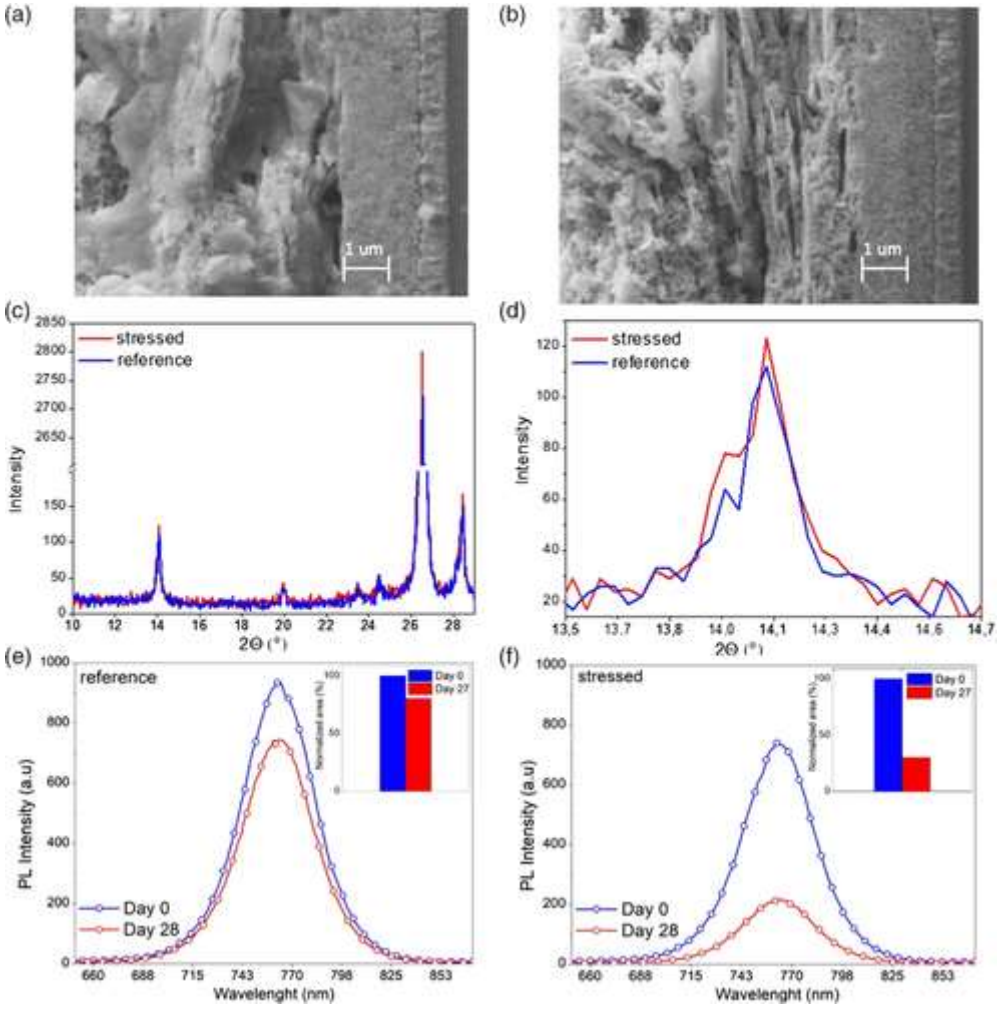

Figure 58 – SEM images for the a) reference and b) stressed cell. c) XRD pattern for the reference (blue line) and stressed (red line) cell, and d) zoom-in of the peak at 14°. Comparison between photoluminescence spectra at t = 0 (blue line) and at t = 648 h (red line) for the e) reference and f) stressed cell. Excitation wavelength at 460 nm. The measurement is taken on the whole cell upon illumination from the bottom glass side.

Figure 58a,b show the SEM images of the reference and stressed cells. From analyzing the SEM images in cross-section, the perovskite bulk looks unchanged. Figure 58c,d show the XRD patterns for the reference and the aged cell and a zoom-in of the region around 14°. At first glance, the XRD trace of the aged device reveals no structural changes of the perovskite crystal structure. Remarkably, we can note the absence of the peak at 12.4° related to the PbI_2 phase (which would give a clear indication of material degradation). More in detail, it is fair to recall that the perovskite active layer is made of methylammonium (MA) cation with the addition of 5-amino valeric acid (5-AVA) additive. It has been demonstrated (see Grancini et al.[80]) that 5-AVA templates the crystallization of the perovskite in the pores of mesoporous TiO_2 while its -COOH and -NH_2 groups interact with TiO_2 through hydrogen bonding, ensuring a better interfacial contact with the anode. In addition, it induces the formation of an oriented interface where the $MAPbI_3$ phase has a marked preferential growth direction. This is evident from the increased reflections along the (110) and (220) directions speaking in favor of a preferred orientation along the (hk0) direction. Zooming in on the XRD peak (see Figure 58d), indeed, it is evident that the relative intensity of the main peak at 14.13° with respect to the peak at 14° changes. More in detail, in the stressed cell both (002) and (004) increase in intensity,

whereas the intensity of the (110) and (220) reflections decreases, losing the preferred orientation along the 0hk direction typical of the reference sample (see Grancini et al.[80]). This suggests that thermal degradation affects the perovskite/TiO_2 contact by changing the crystal orientation at the very interface, reducing the marked preferential orientation and possibly influencing the quality of the interface itself (i.e., the trapping/detrapping). Overall, this observation enables us to assess that the thermal stress modifies the interface crystal orientation, enabling us to disentangle the contributions of the bulk versus interfaces.

To get a further understanding, we also measured the reference and aged devices at time zero and after running the test, monitoring their photoluminescence (PL) signal. As such, PL offers a fingerprint of the quality of the perovskite layer and enables a qualitative prediction of the recombination mechanism.

Figure 58e,f show the PL spectra of the cell at day 0 (blue line) compared to the signal registered for the same cell at day 28 (red line) for both the reference and the stressed solar cells, respectively. The reference cell shows a slight reduction of the PL intensity (19.6%), whereas the aged cell displays a more severe PL quenching (with a reduction of 69.9%). Although the decrease in the PL signal could hide several concomitant effects, we suggest that it is associated with the reduced shunt resistance. This indicates an effect of the interfaces, rather than of the bulk. This is related to the fact that the PL experiment has been performed upon illuminating the device from the glass side. Considering that at 460 nm excitation wavelength the penetration depth is a few hundred nanometers, we are mainly interrogating the perovskite layer which is infiltrated within the TiO_2 scaffold (500 nm thick; see Experimental Section). Therefore, the change in the PL is mainly due to perovskite/TiO_2 interface, excluding the bulk or the perovskite/top contact interface. The interpretation of degradation occurring at the perovskite/TiO_2 interface is in line with the results of the fitting and of combined PL/XRD/SEM measurements; nevertheless, a more complex scenario cannot be excluded at this stage. Associating degradation of solar cell efficiency to specific spatial locations will require more extended studies, including PL with excitation from both sides and simultaneous fitting of illuminated and dark I–V.

3.3.2 Conclusion

In conclusion, our work sheds light on the degradation mechanisms of C-PSCs under thermal stress. C-PSCs are stable at temperature below 50° and up to 80° with limited operating time. Upon prolonged thermal stress, degradation takes place. From combined modeling, device data, and optical characterization, we can conclude that the main effect of thermal stress leads to a reduction of the shunt resistance. Although this can be associated with both degradation of bulk perovskite and perovskite/contacts, PL and XRD analyses demonstrate that it is the perovskite/TiO_2 interface which is mostly affected—mainly through a rearrangement of the interface orientation and interface crystallization. It is thus imperative to focus further work on the interface optimization as an effective strategy to overcome the instability issue and to bring this technology closer to marketability requirements.

3.4 From Bulk to Surface Passivation: Double Role of Chlorine-Doping for Boosting Efficiency of FAPbI3-rich Perovskite Solar Cells preparation

In this work, we take a step forward and demonstrate the use of a combined bulk and surface passivation including MACl in the bulk and depositing MePEACl on the surface. The latter reacts in situ with the excess of PbI_2 present in our active layer, forming an LDP phase at the perovskite/hole transporting material interface. This leads to simultaneous reduction of bulk and interfacial losses resulting in a sequential improvement in the device efficiency with a champion PCE of 21.4%. X-Ray diffraction (XRD) analysis and in-depth time-of-flight secondary ion mass spectroscopy (ToF-SIMS) reveal that Cl^- diffuses in the bulk and concomitantly aggregates at the top perovskite surface, forming a mixed-phase LDP in the form of $MePEA_2(MA_xFA_{1-x})_{n-1}Pbn(I_{1-y}Cl_y)_{3n+1}$. In addition, we use hyperspectral photoluminescence (PL) imaging to probe the spatial distribution of the LDP, combined with photoluminescence quantum yield (PLQY) and electroluminescence (EL) measurements, to reveal an overall much higher and more spatially uniform radiative recombination signal which we associate to effective defect passivation.

3.4.1 Experimental Results: Device Engineering

To reveal the role of the different Cl-based passivation, we fabricated $FAPbI_3$-based PSCs in standard n-i-p architecture where the active layer is sandwiched between tin oxide and, Spiro-OMeTAD, functioning as electron and hole transporting layer (ETL/HTL), respectively. In Figure 59a, a scheme of the device structures is depicted highlighting the three different configurations of the active layer, namely: 1) pure $FAPbI_3$; 2) $FAPbI_3$(MACl), i.e., $FAPbI_3$ with 20% MACl addition in the precursor solution; and 3) $FAPbI_3$(MACl) treated with MePEACl. For the last case, we used the "layer by layer" deposition approach to form an LDP phase on the surface of the bulk perovskite by in-situ reaction of the $MePEA^+$ cation dissolved in isopropyl alcohol (IPA) with the excess of lead iodide, according to established protocols[81,82]. The current density–voltage (J–V) curves of the related best-performing devices are shown in Figure 59b and the PV parameters are presented in Table 8. Notably, the PCE increases with the MACl addition in the bulk film and further boosts with the surface-layer, reaching a champion device of 21.4%, which is due to a concomitant enhancement of the short-circuit current density (J_{SC}), V_{OC}, and fill factor (FF), as shown in the statistics reported in Figure 59c. The incident photon-to-current efficiency (IPCE) and the integrated current density of the champion devices are reported in Figure 59d. IPCE shows that the cells are active over the whole visible and near-infrared regions. All the curves increase in intensity from 300 to 450 nm and drop at 822, 824, and 827 nm, which correspond to 1.508, 1.505, and 1.499 eV bandgap, for cells fabricated with $FAPbI_3$, $FAPbI_3$(MACl), and $FAPbI_3$(MACl) + MePEACl, respectively. IPCE maximum intensities increment progressively, firstly with MACl addition and then with MePEACl surface treatment, which reaches 90% IPCE. Integrated current densities are calculated to be 19.46, 21.55, and 22.79 $mAcm^{-2}$ for PSCs fabricated

with FAPbI3, $FAPbI_3$(MACl), and $FAPbI_3$(MACl) + MePEACl, respectively, in fair matching with the J–V curves.

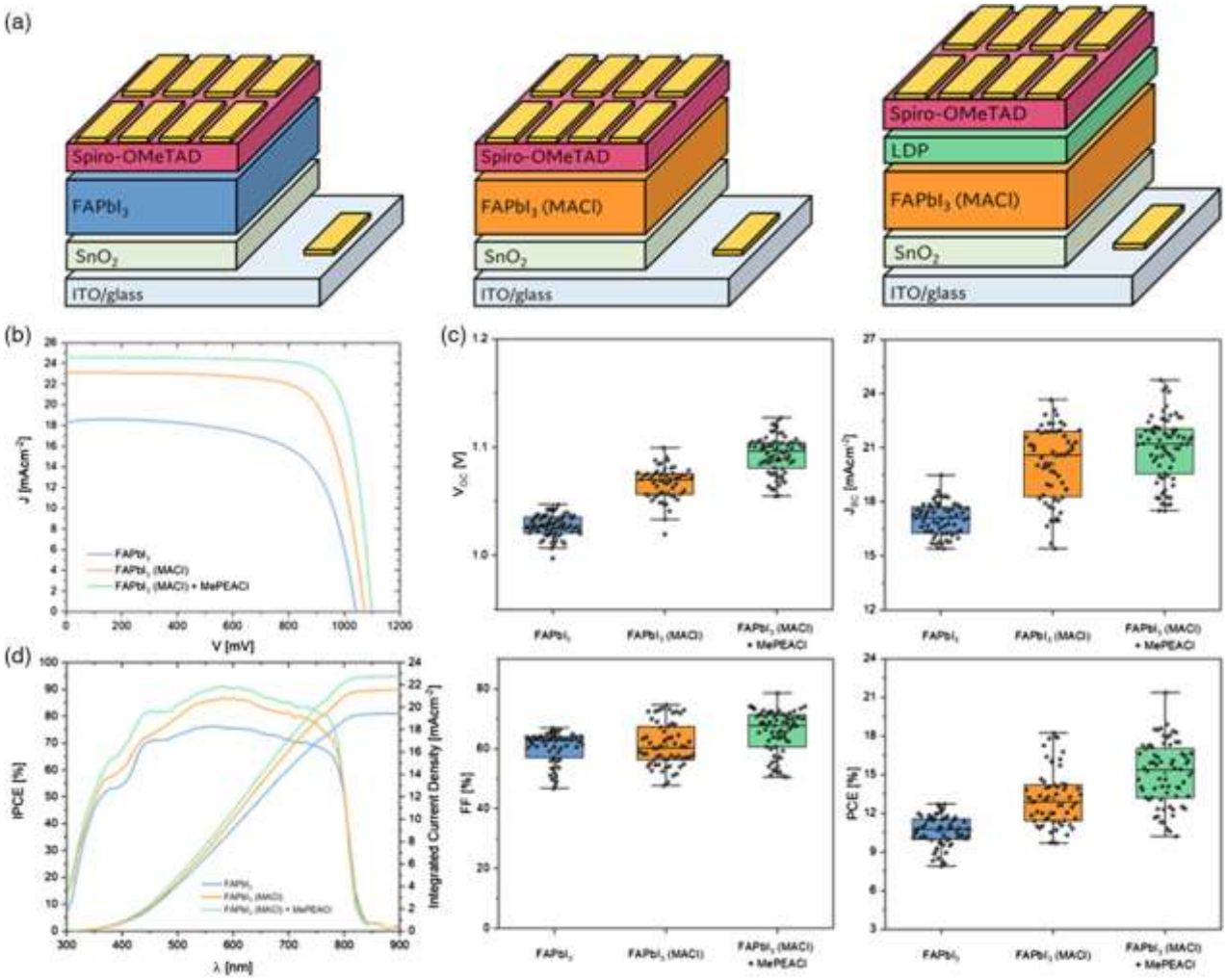

Figure 59 – a) Schematic illustration of the stack of n-i-p perovskite solar cell (PSCs) produced employing FAPbI3, FAPbI3(methylammonium chloride(MACl)), and FAPbI3(MACl)þ4-methylphenethylammonium chloride (MePEACl) as active materials. The perovskites were sandwiched between SnO2electron-transporting layer (ETL) and Spiro-OMeTAD HTL. ITO-coated glass and Au were elected as electrodes of the cells. b)J–Vcharacteristics of thechampion devices produced with FAPbI3(blue line), FAPbI3(MACl) (orange line), and FAPbI3(MACl)þMePEACl (green line) as active materials. Therelated photovoltaic parameters are reported in Table 1. c) Box charts of the photovoltaic parameters displayed by PSCs produced with the three differentconfigurations. d) Incident photon-to-current efficiency (IPCE) and integrated current density of the champion devices fabricated with FAPbI3(blue line),FAPbI3(MACl) (orange line), and FAPbI3(MACl)þMePEACl (green line) as active layers.

Table 8 – Photovoltaic parameters displayed by champion devicesfabricated with FAPbI3, FAPbI3(MACl), and FAPbI3(MACl)þMePEAClas active materials

Perovskite	V_{oc} (V)	J_{sc} (mA/cm^2)	FF (%)	PCE (%)
$FAPbI_3$	1.042	18.30	66.7	12.7
$FAPbI_3$ (MACl)	1.072	23.10	73.6	18.2
$FAPbI_3$ (MACl)+MePEACl	1.098	24.76	78.6	21.4

The results on the device optimization show a net increase in the PV parameters with a distinct effect due to the use of both bulk and surface treatment. The bulk engineering with MACl mainly affects the device J_{SC}

(with an average increase of 18%), while the combined surface treatment also improves the device V_{OC}, without compromising the FF, whose value is enhanced after the adoption of each passivation strategy. We suggest that the increase of the FF can be a consequence of the concomitant improvement of the perovskite crystal quality, induced by MACl bulk treatment, and the reduced defect-mediated recombination losses provided by the LDP coating, as proven in the following by the increase in the PLQY. This suggests a double role of Cl passivation affecting both the bulk and the active layer surface. This assumption is further confirmed by light-intensity-dependent V_{OC} and transient photovoltage (TPV) measurements, displayed in Figure 60. Upon MACl addition and after the combined bulk and surface passivation, the slope values, obtained from the linear fitting of light-intensity-dependent V_{OC} data, decrease, while charge carrier lifetimes, extrapolated from TPV analyses, increase. This suggests that bulk and surface treatments of the perovskite active layer hinder carrier recombination, promoting charge extraction, which is confirmed by the V_{OC} improvement[83].

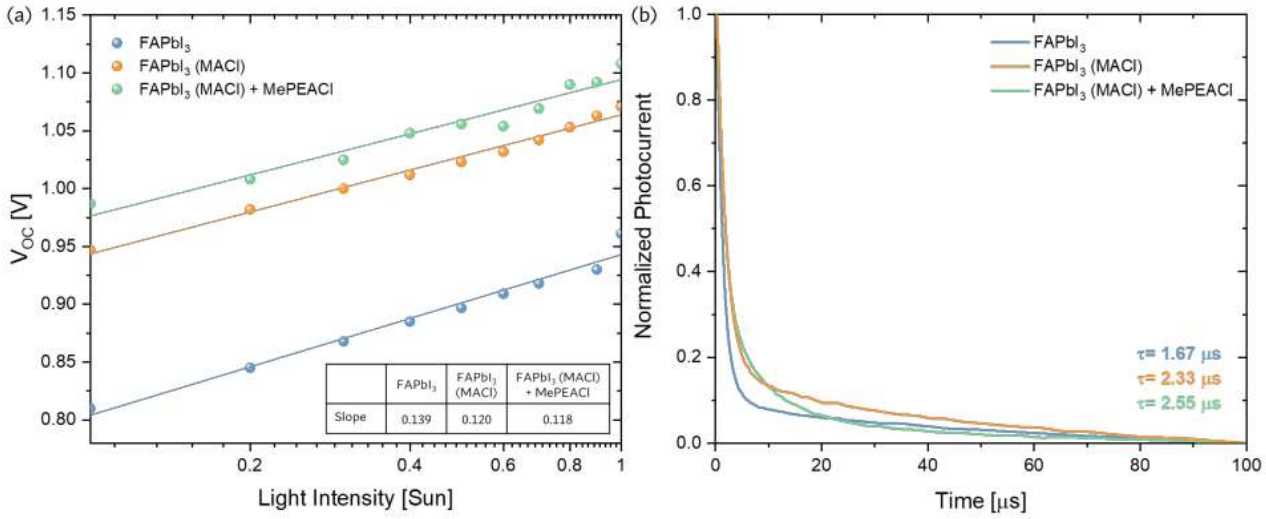

Figure 60 – (a) Light-intensity-dependent analysis of PSCs containing FAPbI3, FAPbI3 (MACl) and FAPbI3 (MACl) + MePEACl as active layers. Slope values are reported in the inset for each architecture. b) TPV decays and charge carrier lifetimes of FAPbI3, FAPbI3 (MACl) and FAPbI3 (MACl) + MePEACl based PSCs.

To evaluate the effect that the double passivation has on the time of life of the cells, we performed stability measurements. Figure 61a shows the maximum power point (MPP) tracking analysis evaluated over continuous illumination at AM1.5G 1 Sun intensity for 300 min. $FAPbI_3(MACl) + MePEACl$ retains more than 90% of its initial MPP, while bare $FAPbI_3$ and $FAPbI_3(MACl)$ lose more than 30% and 20%, respectively. Figure 61b presents the normalized PCE of the three types of cells, measured each week for three weeks, keeping the devices under inert atmosphere and in dark conditions. In this case, both the bulk passivation and the combined bulk and surface treatment have a beneficial effect on the shelf-life stability of the cells, which keep more than 90% of the initial PCE.

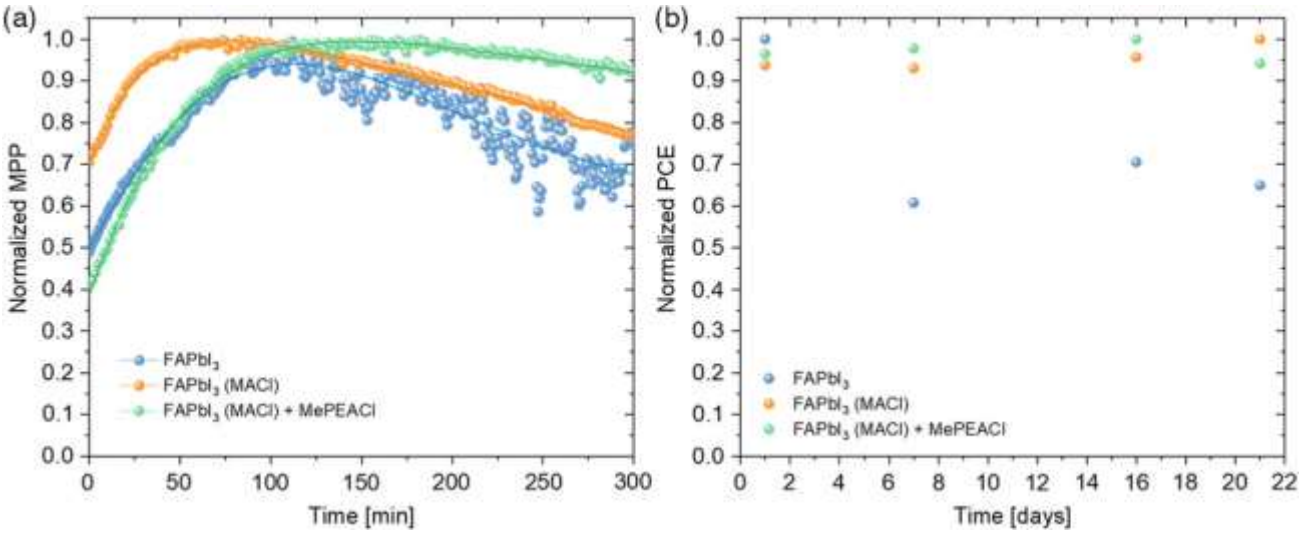

Figure 61 – a) Maximum power point (MPP) tracking of PSCs fabricated with FAPbI3(blue), FAPbI3(MACl) (orange), and FAPbI3(MACl)þMePEACl(green) as active materials. b) Normalized photovoltaic conversion efficiency (PCE) of PSCs fabricated with FAPbI3(blue), FAPbI3(MACl) (orange), andFAPbI3(MACl)þMePEACl (green) as active materials evaluated for 21 days keeping the cells in dark and inert atmosphere.

3.4.2 Analysis and Structural Investigation

To investigate the origin behind such improvement, we analyzed the chlorine distribution induced by the bulk and the surface treatment with ToF-SIMS, enabling the visualization of the elemental profiles across the sample thickness. Results for the treated configurations are presented in Figure 62a,b.

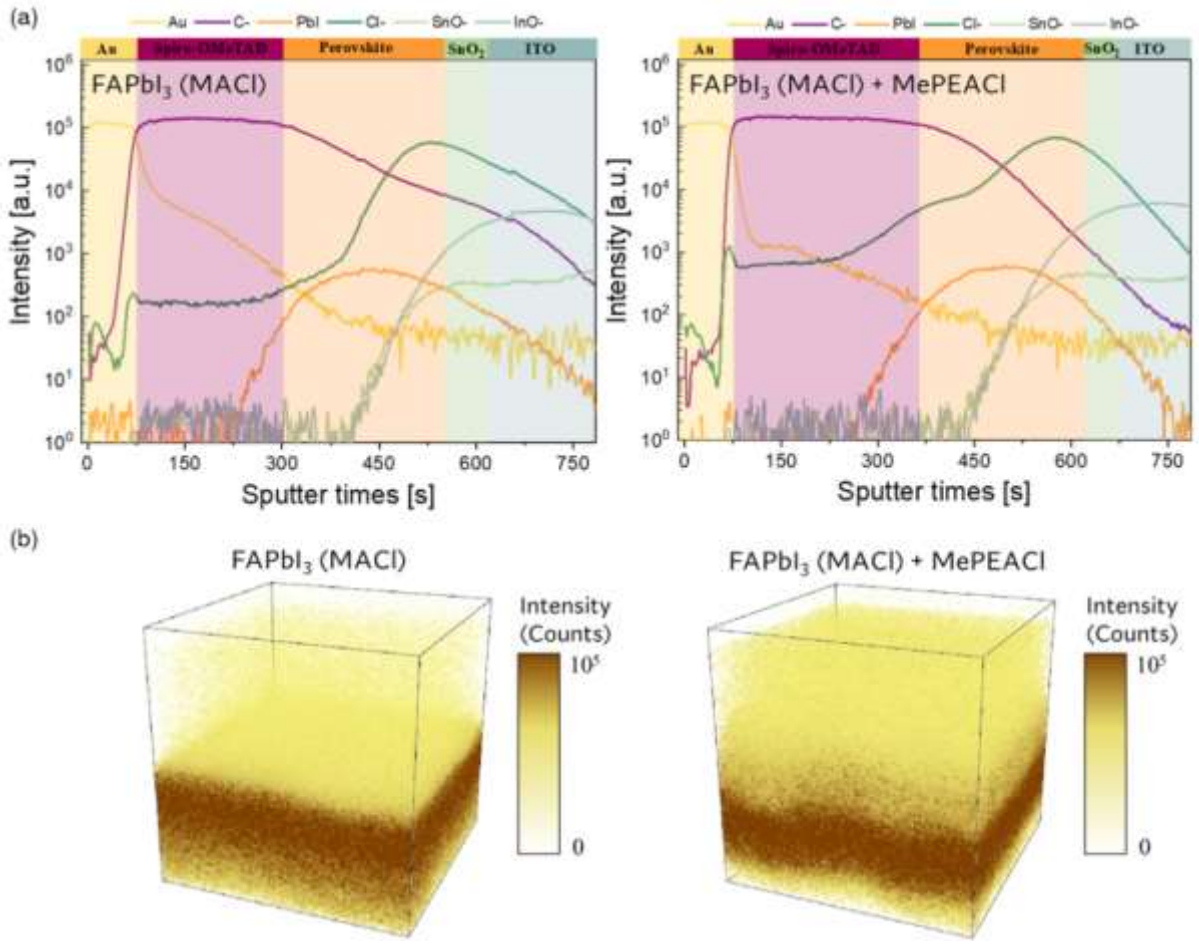

Figure 62 – a) Time-of-flight secondary ion mass spectroscopy (ToF-SIMS) profiles of Au, C-, PbI, Cl-, SnO-, and InO- within FAPbI3(MACl) and FAPbI3(MACl)þMePEACl, b) 3D Cl distributions, extrapolated from ToF-SIMS analyses, of FAPbI3(MACl) and FAPbI3(MACl)þMePEACl.

Those concerning bare $FAPbI_3$ are reported in Figure 63

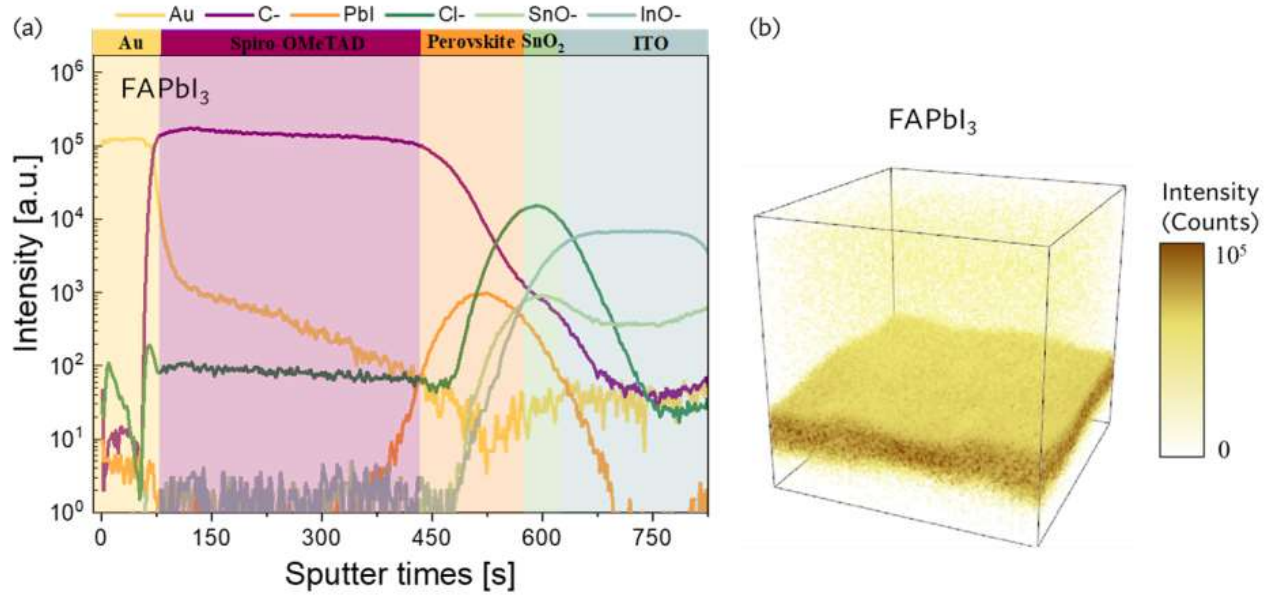

Figure 63 – a) ToF-SIMS profiles of Au, C-, PbI, Cl-, SnO- and InO- and b) 3D Cl distribution 2 of $FAPbI_3$.

Interestingly, when the PbI_2 curve peaks, the amount of C is five times higher in the $FAPbI_3$(MACl) spectrum than for bare $FAPbI_3$. Although it has been reported that MACl is released during the annealing process of the perovskite[84], the evidence of the increased amount of C in the active layer after MACl addition prevents us from excluding the incorporation of a certain amount of MA^+ in the structure of $FAPbI_3$. Furthermore, while the $FAPbI_3$ active layer contains a very little amount of Cl, ten times lower than for the treated systems, within $FAPbI_3$(MACl) the concentration of Cl ions increases, producing a gradient distribution toward the perovskite/ETL interface (see Figure 62b for the spatial Cl distributions in the cells). $FAPbI_3$(MACl) + MePEACl displays almost the same amount of Cl in the bulk as $FAPbI_3$(MACl) but, in addition, a higher quantity of the anion appears at the top perovskite/Spiro-OMe-TAD interface. Interestingly, UV–vis spectra and tauc plots, which are reported in Figure 64a-b, respectively, show a progressive shift in the bandgap of the perovskite material toward higher energy values upon Cl treatment.

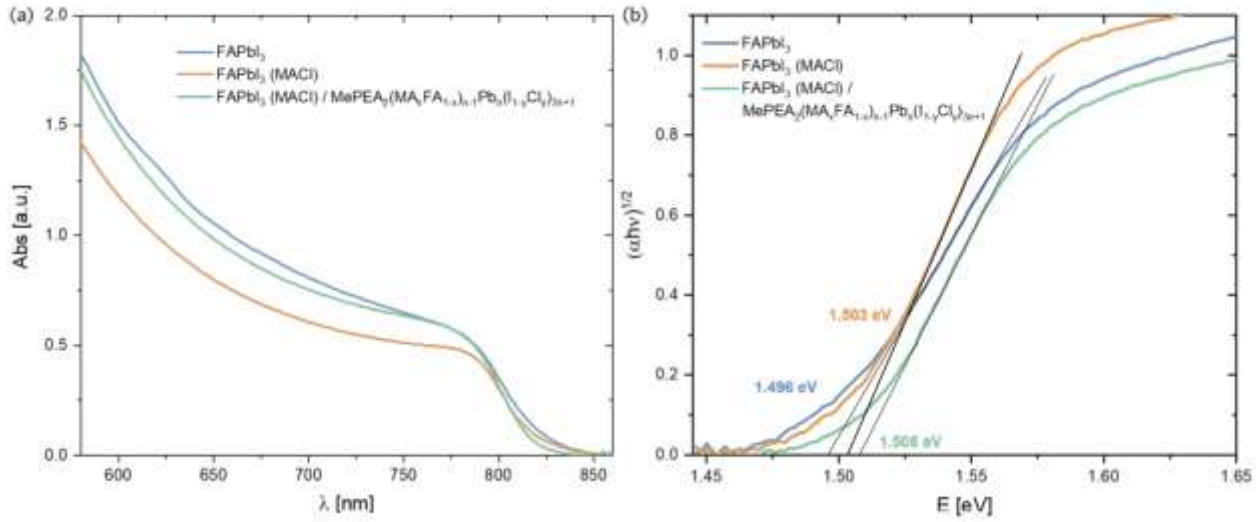

Figure 64 – (a) ToF-SIMS profiles of Au, C-, PbI, Cl-, SnO- and InO- and (b) 3D Cl distribution 2 of FAPbI3.

This result, combined with the insights gained with ToF-SIMS analysis, suggests that Cl^- is indeed incorporated into $FAPbI_3$ crystal structure, presumably passivating structural defects, which is likely the origin of the decreased nonradiative recombination, addressed in the following section, which in turn results in a superior extraction process, verified by TPV analysis. To better reveal the crystal structure and the impact of the MACl addition, we investigated the XRD patterns of $FAPbI_3$, $FAPbI_3$ (MACl), and $FAPbI_3$ (MACl) + MePEACl, as reported in Figure 3c. Characteristic peaks at $2\theta = 14.0°$ and higher order reflections are observed and assigned to α-$FAPbI_3$[85]. For the pure $FAPbI_3$ film, however, a small peak at $2\theta = 11.9°$ is also present, ascribed to the unwanted δ-$FAPbI_3$[85]. Upon MACl addition in the bulk, such secondary peak disappears, indicating that the additive induces the crystallization of a pure α-phase, in agreement with the literature[84,86]. The addition of the MePEACl, leads to the formation of a new phase, as indicated by the presence of the peak at $2\theta = 5.0°$. Our surface treatment demonstrates the formation of an LDP layer, which

we infer it as correlated to the Cl surface segregation observed in the ToF-SIMS profile of $FAPbI_3$ (MACl) + MePEACl[87]. Concomitantly, the peak related to lead iodide at $2\theta = 12.6°$ decreases with respect to $FAPbI_3$ (MACl) which suggests its incorporation in the LDP.

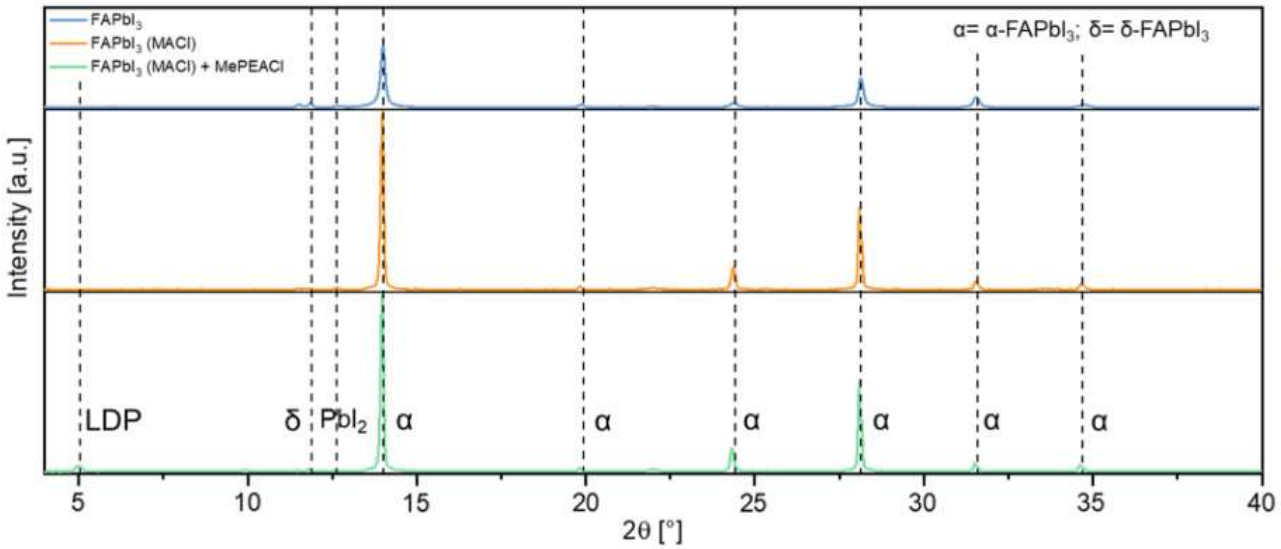

Figure 65 – X-Ray diffraction(XRD) patterns of FAPbI3(blue line), FAPbI3(MACl) (orange line), and FAPbI3(MACl)þMePEACl (green line) thinfilms deposited on glass.www.advancedsciencenews.comwww.solar-rrl.comSol. RRL2022,6, 22000382200038 (5 of 9)© 2022 The Authors. Solar RRL published by Wiley-VCH GmbH

Overall, the XRD analysis reveals a higher crystal quality obtained upon bulk engineering, which hampers the formation of the unwanted δ-FAPbI3. This can suggest a better film crystallinity, which can be related to the higher J_{SC} measured in the device, as further addressed in the following section. In contrast, the LDP surface treatment can be responsible for the improved device V_{OC}.

3.4.3 Microscopic Investigation

Such improvement in the V_{OC} can be assigned to a reduced nonradiative recombination, which we verify by performing PL and EL measurements. While the bandgap of the different samples slightly shifts (see Figure 64), EL spectra of $FAPbI_3$, $FAPbI_3$ (MACl), and $FAPbI_3$ (MACl) + MePEACl significantly change, as reported in Figure 66a. In particular, the intensity of the peak increases when MACl is added to the perovskite and it is further enhanced upon the surface treatment with MePEACl, which is in good agreement with the improved V_{OC} of the devices, previously discussed and presented in Figure 59c.

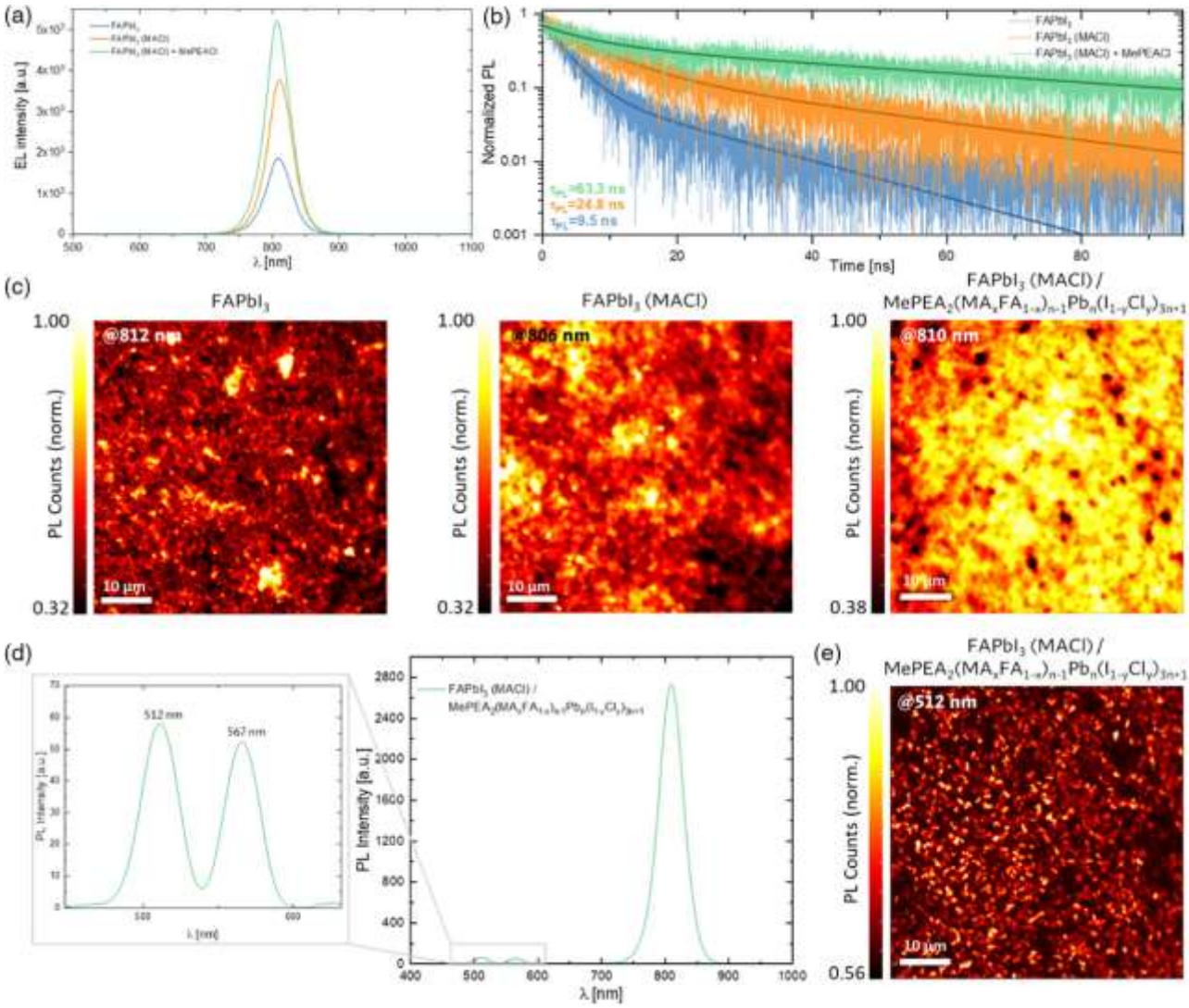

Figure 66 – a) Electroluminescence (EL) spectra of $FAPbI_3$ (blue line), $FAPbI_3$(MACl) (orange line), and $FAPbI_3$(MACl)+MePEACl (green line) thin films deposited on glass. b) Time-resolved photoluminescence (TRPL) decays and related τ_{PL} of $FAPbI_3$, $FAPbI_3$(MACl), and $FAPbI_3$(MACl)+MePEACl thin films deposited on glass, investigated with a 470 nm laser. c) PL 60x60µm maps of $FAPbI_3$, $FAPbI_3$(MACl), and $FAPbI_3$(MACl)/$MePEA_2(MA_xFA_{1-x})_{n-1}Pb_n(I_{1-y}Cl_y)_{3n+1}$ thin films deposited on glass and excited at 405 nm, with emission collected at 812, 806, and 810, respectively. The scale of each image is the intensity normalized to total counts. d) Photoluminescence (PL) spectrum of $FAPbI_3$(MACl)/$MePEA_2(MA_xFA_{1-x})_{n-1}Pb_n(I_{1-y}Cl_y)_{3n+1}$ acquired over the 400–1000 nm region. A zoom in the 455–630 nm region is reported on the side. e) PL 60x60µm map of $FAPbI_3$(MACl)/$MePEA_2(MA_xFA_{1-x})_{n-1}Pb_n(I_{1-y}Cl_y)_{3n+1}$ thin film deposited on glass, excited at 405nm and collected at 512 nm emission wavelength.

Similarly, the chlorine treatment of the bulk and the surface passivation of the perovskite lead to a progressive increase in the relative PLQY (Table 9). The effects that the combined bulk and surface treatment have on carrier lifetime and recombination processes were studied with time-resolved photoluminescence (TRPL) investigation. Thin films of $FAPbI_3$, $FAPbI_3$ (MACl), and $FAPbI_3$ (MACl) + MePEACl were tested with a pulsed 470 nm laser and with an energy fluence of 5.0×10^{-5} J cm^{-2}. TRPL traces, which are reported in Figure 66b, are fitted with a biexponential decay model, expressed by Equation (75), while τ_{PL} was calculated by means of Equation (76). The obtained values of A_1, τ_1, A_2, τ_2, τ_{PL} are reported in Table 10.

$$I_{PL}(t) = A_1 e^{\left(\frac{t}{\tau_1}\right)} + A_2 e^{\left(\frac{t}{\tau_2}\right)} \quad (75)$$

$$\tau_{PL} = \frac{A_1\tau_1^2 + A_2\tau_2^2}{A_1\tau_1 + A_2\tau_2} \quad (76)$$

Table 9 – Relative PLQY evaluated on FAPbI3, FAPbI3(MACl), and FAPbI3(MACl)þMePEACl thin films deposited on glass.

Perovskite	Relative PLQY
$FAPbI_3$	1.00
$FAPbI_3$ (MACl)	2.09
$FAPbI_3$ (MACl)+MePEACl	3.45

Table 10 – Values of A_1, τ_1, A_2, τ_2, and τ_{PL} obtained from biexponential fitting of TRPL decays acquired on $FAPbI_3$, $FAPbI_3$(MACl), and $FAPbI_3$(MACl)+MePEACl thin films deposited on glass.

Perovskite	A_1 (%)	τ_1 (ns)	A_2 (%)	τ_1 (ns)	τ_{PL} (ns)
$FAPbI_3$	87.5 (±0.4)	3.1 (±0.1)	12.5 (±0.4)	17.5 (±0.5)	9.5
$FAPbI_3$ (MACl)	76.1 (±0.8)	7.2 (±0.1)	23.9 (±0.8)	36.0 (±1.0)	24.8
$FAPbI_3$ (MACl)+MePEACl	45.3 (±0.6)	7.1 (±0.2)	54.6 (±0.6)	68.1 (±1.1)	63.3

τ1, which is the shorter lifetime, raises with the bulk treatment but no further increment is displayed after the synergistic employment of MACl and MePEACl, while τ_2 increases upon MACl addition and after the combined bulk and surface passivation. A_1 and A_2 show opposite trends, progressively decreasing and rising respectively. Previous works report that the longer lifetime (τ_2) can be associated with bulk-radiative processes, while the shorter lifetime (τ_1) can be assigned to trap-mediated recombination as a means to quantify the decays but without assuming a physical mode[88]. Hence, the decrease of A_1 can suggest a lower contribution of trap-state-related recombination within $FAPbI_3$(MACl) and $FAPbI_3$(MACl) + MePEACl with respect to bare $FAPbI_3$. Overall, the progressive improvement of τ_{PL} indicates that the PL lifetime of the perovskite film is promoted by bulk and surface passivation. Figure 66c presents PL maps of $FAPbI_3$, $FAPbI_3$(MACl), and $FAPbI_3$(MACl) + MePEACl acquired at the maximum PL peak emission wavelength for each. Bare, untreated $FAPbI_3$ presents spatial inhomogeneities in the PL map with domains of low PL signal. Upon adding MACl in the bulk, the distribution of the PL signal becomes more homogeneous throughout the entire investigated area, which also applies to $FAPbI_3$(MACl) + MePEACl. EL, PL mapping, and PLQY results suggest that, first, the bulk treatment of $FAPbI_3$ with MACl has a beneficial effect on the PL signal distribution within the sample – reflecting a more homogeneous morphology on the macroscopic scale – and, second, the surface treatment with MePEACl boosts the PL emission intensity of the perovskite layer. Figure 66d shows the PL spectrum of $FAPbI_3$ (MACl) + MePEACl, acquired over the entire 400–1000 nm region. Beyond the most intense peak at 810 nm ascribed to α-$FAPbI_3$ emission[89], we observe two

minor peaks at the lower wavelength side at 512 and 567 nm, as highlighted in the inset. Such emission has a homogeneous spatial distribution, as indicated in the PL map recorded at 512 nm, reported in Figure 4e. The results confirm the formation of the LDP, which we can indicate as $MePEA_2(MA_xFA_{1-x})_{n-1}Pb_n(I_{1-y}Cl_y)_{3n+1}$, characterized by different phases of n = 1 (emitting at 512 nm) and n > 1 (emitting at 567 nm). Finally, we also looked more in detail at the nano-morphologies of the films scanned with atomic force microscopy (AFM) and scanning electron microscope (SEM). SEM images in cross-section of the devices are reported in Figure 67.

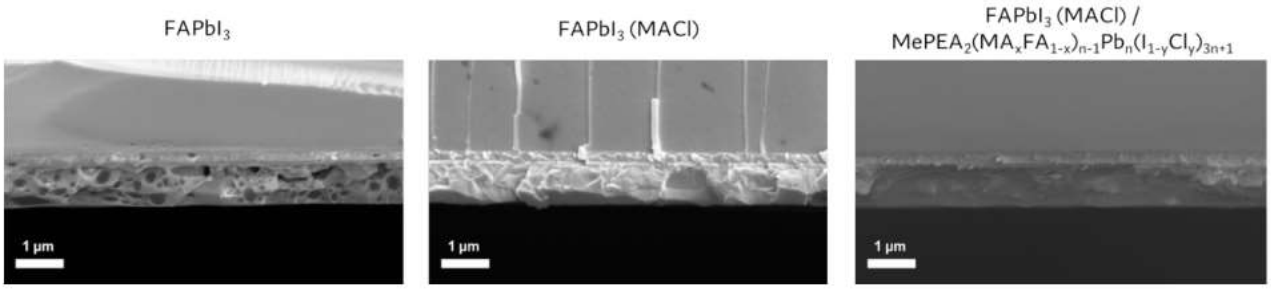

Figure 67 – SEM images in cross-section of PSCs fabricated with $FAPbI_3$, $FAPbI_3$ (MACl) and 10 $FAPbI_3$ (MACl) / $MePEA_2(MA_xFA_{1-x})_{n-1}Pb_n(I_{1-y}Cl_y)_{3n+1}$ as active layers.

While microscopic images of the perovskite films are shown in Figure 68.

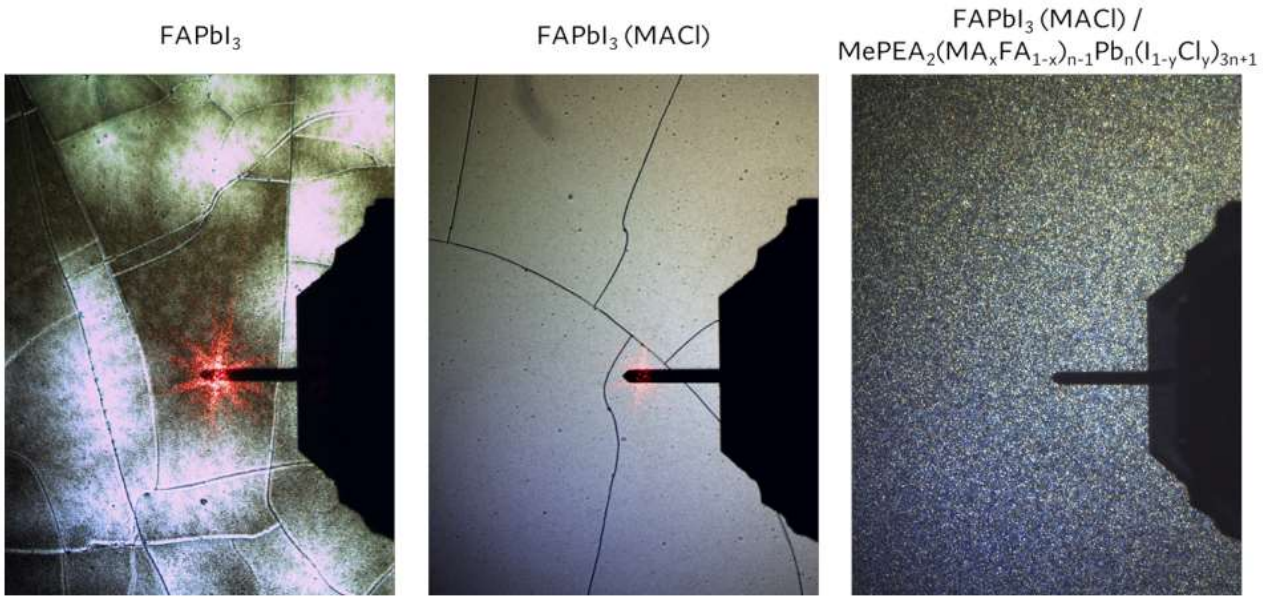

Figure 68 – Microscopic images acquired with AFM microscope (APEResearch srl) of $FAPbI_3$, $FAPbI_3$ (MACl) and 10 $FAPbI_3$ (MACl) / $MePEA_2(MA_xFA_{1-x})_{n-1}Pb_n(I_{1-y}Cl_y)_{3n+1}$.

Interestingly, bare $FAPbI_3$ presents surface cracks, which are further analyzed in Figure 69.

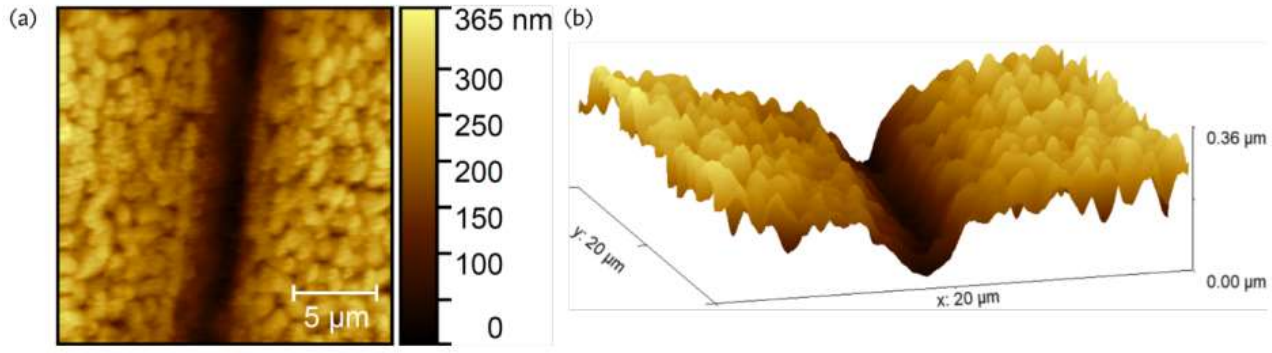

Figure 69 – (a) AFM 20x20 µm image and (b) 3D rendering of a surface crack of $FAPbI_3$. The crack depth is lower than the perovskite thickness, which indicates that the fracture does not extend throughout the entire layer thickness.

As depicted in AFM images, presented in Figure 70a, $FAPbI_3$ morphology is formed of micrometer-sized large regions, while the doped materials seem composed of smaller domains. Importantly, $FAPbI_3$ is characterized by an average higher root mean square (RMS) roughness than $FAPbI_3$ (MACl), namely 8 ± 2 and 6.9 ± 0.1 nm respectively, which also applies to $FAPbI_3$(MACl)/$MePEA_2(MA_xFA_{1-x})_{n-1}Pb_n(I_{1-y}Cl_y)_{3n+1}$. Overall, the calculated values of RMS roughness are lower than those presented in the literature[90], indicating a smoother morphology and higher crystal homogeneity as a result of our double passivation.

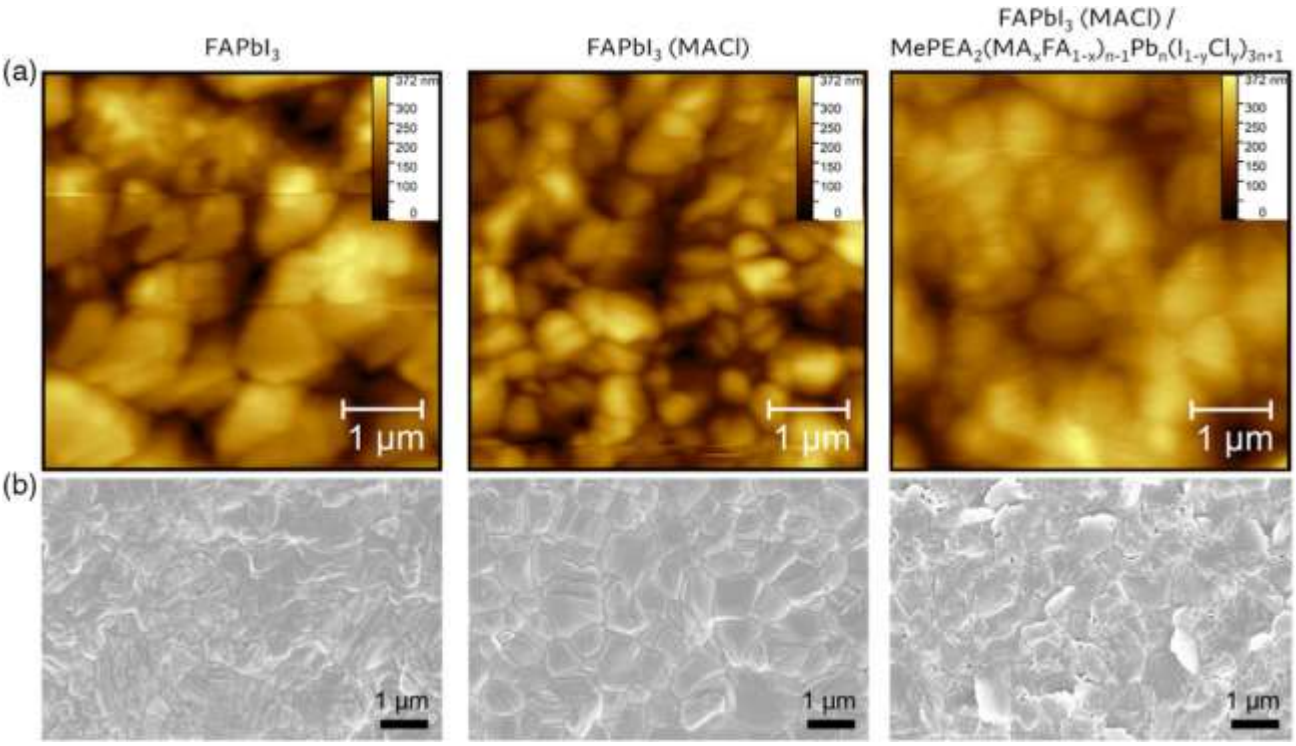

Figure 70 – a) Atomic force microscopy (AFM) 5x5µm images, collected in contact mode, of $FAPbI_3$, $FAPbI_3$ (MACl) and 10 $FAPbI_3$ (MACl) / $MePEA_2(MA_xFA_{1-x})_{n-1}Pb_n(I_{1-y}Cl_y)_{3n+1}$ thin films deposited on glass. The scale for each image is the intensity normalized to total counts of $FAPbI_3$, $FAPbI_3$ (MACl) and 10 $FAPbI_3$ (MACl) / $MePEA_2(MA_xFA_{1-x})_{n-1}Pb_n(I_{1-y}Cl_y)_{3n+1}$. b) Scanning electron microscope (SEM) top-view images of $FAPbI_3$, $FAPbI_3$ (MACl) and 10 $FAPbI_3$ (MACl) / $MePEA_2(MA_xFA_{1-x})_{n-1}Pb_n(I_{1-y}Cl_y)_{3n+1}$ thin films deposited on ITO.

SEM images of the three materials are displayed in Figure 70b. Unaltered $FAPbI_3$ is characterized by smaller grains, of varying dimension, while both $FAPbI_3$(MACl) and

$FAPbI_3$(MACl)/$MePEA_2(MA_xFA_{1-x})_{n-1}Pb_n(I_{1-y}Cl_y)_{3n+1}$ have bigger grains. In the last case, a thin film covers the surface, consistent with the formation of an LPD phase over $FAPbI_3$.

AFM and SEM results suggest that bulk passivation improves the quality of the film, thus enhancing the J_{SC} of the devices, as observed in the photovoltaic parameters trend.

3.4.4 Conclusion

In summary, we have demonstrated double surface and bulk passivation of perovskite films using chlorine atoms dispersed in the bulk and as organic parts forming a shallow LDP phase, providing enhanced device performances with a champion device of 21.4% PCE. Our experimental results suggest that Cl anions diffuse into the bulk of $FAPbI_3$ perovskite, greatly enhancing the bulk morphology and film quality, thus the device J_{SC}. We also demonstrate that Cl-based organic cation top passivation forms a surface layer of mixed-phase LDP, contributing to the overall device enhancement with a special boost in the device V_{OC}. This paves the way for further use of Cl-based or even mixed halide-based compounds for the smart passivation of different types of defects at both bulk and surface levels.

4 Conclusions

In summary, in this thesis we demonstrate the importance of the engineering of the interfaces for PSC, this step is crucial to have an improvement of PSC in efficiency and in stability in both structure nip and pin. We have pointed out how the passivation of perovskite's surface is crucial due the defects located at the interfaces.

For nip structure has been demonstrate that the passivation in the bulk and the surface improves the stability and the efficiency of the device. The bulk passivation improves the quality of the film helping the formation of a pure α-phase of the perovskite and the optoelectronic properties of the film (photoluminescence, lifetime of the carriers). The surface passivation forms a mixed phase of LDP that have similar benefits as the bulk passivation: a enhancement of the emission of the perovskite and longer life of the carriers. The improvement led to achieve more than 21% of efficiency with a remarkably boost in the V_{OC} and J_{SC}.

For the pin structure a novel method has been used and lead to increase the performance of the PSC. With this method there is no evidence of the formation of a 2D perovskite layer, but it is possible observe a similar behavior in the enhance of the efficiency and stability. Thanks to the passivation between the HTL and the perovskite is possible observe an enhancement of the fill factor related to the reduction of the nano pinholes present in the devices, this is also responsible of the slight enhancement in the current density. The top treatment between the perovskite and the ETL has been demonstrated to led to the enhancement of the V_{OC} due to the reduction of the no radiative losses as demonstrated also from ELQE. Also, the enhancement of the photoluminescence supports this thesis and through the photoluminescence maps was possible demonstrate the uniformity in the distribution of the PEAI cations deposited on the surface of the perovskite. Moreover, this top treatment improved the QFLS. The double passivation demonstrates to be extremely effective achieving the efficiency 23.7% with also a remarkably good fill factor of 85% and almost no loss even after 2000 minutes under continuous illumination.

These results are extremely important also for future research and application. A comparison of the different A cations of the 2D perovskite, and a deeper knowledge of when the 2D perovskite is formed or not will be useful to exploit the potential of this material, and eventually improve the protection of the device leading to the commercialization of it.

The study on these cations is extremely important due to the low cost and also their solubility in no toxic solvent (as alcohols) opening the possibility to application on large area techniques for example through technique as inject printing or blade coating. This will be a way to improve the scale-up of PSC minimizing the losses related to scaling up. Moreover, the synthesis of new cations can lead the improvements not just on a single junction but also in tandem solar cells that suffer a lot the losses at the interfaces. It is possible that the passivation with 2D cations can give a boost also in this other field reducing the defects and increasing the efficiency and stability of the devices as for the single junction. These are only a few research

directions but as demonstrated in this thesis the versatility of perovskite is high, for this reason, commercialization is getting closer.

5 Bibliography

1. Council, W. E. World Energy Scenarios Composing energy futures to 2050. *World Energy Counc. Co. Ltd.* 1–138 (2013).

2. Physical, T. & Basis, S. Climate Change 2021 The Physical Science Basis. *Intergov. panel Clim. Chang.* **34**, F0003–F0003 (2020).

3. IRENA. World energy transitions outlook. *Irena* 1–54 (2021).

4. Renewable Energy Market Update. *Renew. Energy Mark. Updat.* (2020) doi:10.1787/afbc8c1d-en.

5. International Energy Agency. Global Energy Review 2021. *Glob. Energy Rev. 2020* 1–36 (2021).

6. Mastoi, M. S. *et al.* A Critical Analysis of the Impact of Pandemic on China's Electricity Usage Patterns and the Global Development of Renewable Energy. *Int. J. Environ. Res. Public Health* **19**, (2022).

7. Mulvaney, D. & Robbins, P. Total Primary Energy Supply. *Green Energy: An A-to-Z Guide* (2012) doi:10.4135/9781412971850.n122.

8. Fox, M. Optical Properties of Solids. *OXFORD MASTER Ser. Condens. MATTER Phys.* 283–314 (2020) doi:10.1201/b12047-14.

9. Brinkworth, B. J. Solar energy. *UIT Cambridge* **249**, 726–729 (2015).

10. Tao, Y. Screen-Printed Front Junction n-Type Silicon Solar Cells. *Print. Electron. - Curr. Trends Appl.* (2016) doi:10.5772/63198.

11. Best Research-Cell Efficiencies. 1 (2022).

12. Nelson, J. *Hysics of Solar*.

13. Green, M. a. Third Generation Photovoltaics - Introduction. *Third Gener. Photovoltaics* 1–6 (2013).

14. Kim, J. Y., Lee, J. W., Jung, H. S., Shin, H. & Park, N. G. High-Efficiency Perovskite Solar Cells. *Chem. Rev.* **120**, 7867–7918 (2020).

15. Wu, T. *et al.* The Main Progress of Perovskite Solar Cells in 2020–2021. *Nano-Micro Lett.* **13**, 1–18 (2021).

16. Snaith, H. J. Perovskites: The emergence of a new era for low-cost, high-efficiency solar cells. *J. Phys. Chem. Lett.* **4**, 3623–3630 (2013).

17. Stranks, S. D. & Snaith, H. J. Metal-halide perovskites for photovoltaic and light-emitting devices. *Nat. Nanotechnol.* **10**, 391–402 (2015).

18. Bisquert, J. & Juarez-Perez, E. J. The Causes of Degradation of Perovskite Solar Cells. *J. Phys. Chem. Lett.* **10**, 5889–5891 (2019).

19. An, Q., Paulus, F. & Vaynzof, Y. Controlling the Microstructure and Porosity of Perovskite Films by Additive Engineering. *ACS Appl. Energy Mater.* **4**, 2990–2998 (2021).

20. Bi, C. *et al.* Non-wetting surface-driven high-aspect-ratio crystalline grain growth for efficient hybrid perovskite solar cells. *Nat. Commun.* **6**, 1–7 (2015).

21. Li, Y. *et al.* Two-step solvent post-treatment on PTAA for highly efficient and stable inverted perovskite solar cells. *Photonics Res.* **8**, A39 (2020).

22. Taylor, A. D. *et al.* A general approach to high-efficiency perovskite solar cells by any antisolvent. *Nat. Commun.* **12**, 1–11 (2021).

23. An, Q. *et al.* High performance planar perovskite solar cells by ZnO electron transport layer engineering. *Nano Energy* **39**, 400–408 (2017).

24. Chen, S. *et al.* Stabilizing perovskite-substrate interfaces for high-performance perovskite modules. *Science (80-.).* **373**, 902–907 (2021).

25. Li, W. *et al.* Approaching optimal hole transport layers by an organic monomolecular strategy for efficient inverted perovskite solar cells. *J. Mater. Chem. A* **8**, 16560–16569 (2020).

26. Sutanto, A. A. *et al.* 2D/3D perovskite engineering eliminates interfacial recombination losses in hybrid perovskite solar cells. *Chem* **7**, 1903–1916 (2021).

27. Liu, Y. *et al.* Ultrahydrophobic 3D/2D fluoroarene bilayer-based water-resistant perovskite solar cells with efficiencies exceeding 22%. *Sci. Adv.* **5**, 1–9 (2019).

28. Jang, Y. W. *et al.* Intact 2D/3D halide junction perovskite solar cells via solid-phase in-plane growth. *Nat. Energy* **6**, 63–71 (2021).

29. Fassl, P. *et al.* Fractional deviations in precursor stoichiometry dictate the properties, performance and stability of perovskite photovoltaic devices. *Energy Environ. Sci.* **11**, 3380–3391 (2018).

30. Xin, D. *et al.* Defect Passivation in Hybrid Perovskite Solar Cells by Tailoring the Electron Density Distribution in Passivation Molecules. *ACS Appl. Mater. Interfaces* (2019) doi:10.1021/acsami.9b15166.

31. Wang, J., Jin, G., Zhen, Q., He, C. & Duan, Y. Bulk Passivation and Interfacial Passivation for Perovskite Solar Cells: Which One is More Effective? *Adv. Mater. Interfaces* **8**, 1–18 (2021).

32. Fu, L. *et al.* Defect passivation strategies in perovskites for an enhanced photovoltaic performance. *Energy Environ. Sci.* **13**, 4017–4056 (2020).

33. Bai, S. *et al.* Planar perovskite solar cells with long-term stability using ionic liquid additives. *Nature* **571**, 245–250 (2019).

34. Lin, Y. H. *et al.* A piperidinium salt stabilizes efficient metal-halide perovskite solar cells. *Science (80-.).* **369**, 96–102 (2020).

35. Akin, S., Akman, E. & Sonmezoglu, S. FAPbI3-Based Perovskite Solar Cells Employing Hexyl-Based Ionic Liquid with an Efficiency Over 20% and Excellent Long-Term Stability. *Adv. Funct. Mater.* **30**, 1–8 (2020).

36. Gharibzadeh, S. *et al.* Two birds with one stone: Dual grain-boundary and interface passivation enables >22% efficient inverted methylammonium-free perovskite solar cells. *Energy Environ. Sci.* **14**, 5875–5893 (2021).

37. Turren-Cruz, S. H., Hagfeldt, A. & Saliba, M. Methylammonium-free, high-performance, and stable perovskite solar cells on a planar architecture. *Science (80-.).* **362**, 449–453 (2018).

38. An, Q. *et al.* Effect of Antisolvent Application Rate on Film Formation and Photovoltaic Performance of Methylammonium-Free Perovskite Solar Cells. *Adv. Energy Sustain. Res.* **2**, 2100061 (2021).

39. Lee, S. W., Bae, S., Kim, D. & Lee, H. S. Historical Analysis of High-Efficiency, Large-Area Solar Cells: Toward Upscaling of Perovskite Solar Cells. *Adv. Mater.* **32**, 1–25 (2020).

40. Degani, M. *et al.* 23.7% Efficient inverted perovskite solar cells by dual interfacial modification. *Sci. Adv.* **7**, 1–10 (2021).

41. Kim, E. B., Akhtar, M. S., Shin, H. S., Ameen, S. & Nazeeruddin, M. K. A review on two-dimensional (2D) and 2D-3D multidimensional perovskite solar cells: Perovskites structures, stability, and photovoltaic performances. *J. Photochem. Photobiol. C Photochem. Rev.* **48**, 100405 (2021).

42. Mahmud, M. A. *et al.* Double-Sided Surface Passivation of 3D Perovskite Film for High-Efficiency Mixed-Dimensional Perovskite Solar Cells. *Adv. Funct. Mater.* **30**, 1–11 (2020).

43. Kirchartz, T., Márquez, J. A., Stolterfoht, M. & Unold, T. Photoluminescence-Based Characterization of Halide Perovskites for Photovoltaics. *Adv. Energy Mater.* **10**, (2020).

44. Krückemeier, L., Krogmeier, B., Liu, Z., Rau, U. & Kirchartz, T. Understanding Transient Photoluminescence in Halide Perovskite Layer Stacks and Solar Cells. *Adv. Energy Mater.* **11**, (2021).

45. Goetz, K. P., Taylor, A. D., Paulus, F. & Vaynzof, Y. Shining Light on the Photoluminescence Properties of Metal Halide Perovskites. *Adv. Funct. Mater.* **30**, (2020).

46. Sarritzu, V. *et al.* Optical determination of Shockley-Read-Hall and interface recombination currents

in hybrid perovskites. *Sci. Rep.* **7**, 1–10 (2017).

47. Stolterfoht, M. *et al.* Visualization and suppression of interfacial recombination for high-efficiency large-area pin perovskite solar cells. *Nat. Energy* **3**, 847–854 (2018).

48. Delamarre, A. Characterization of solar cells using electroluminescence and photoluminescence hyperspectral images. *J. Photonics Energy* **2**, 027004 (2012).

49. Bercegol, A., El-Hajje, G., Ory, D. & Lombez, L. Determination of transport properties in optoelectronic devices by time-resolved fluorescence imaging. *J. Appl. Phys.* **122**, (2017).

50. Chan, S. H. *et al.* Enhancing perovskite solar cell performance and stability by doping barium in methylammonium lead halide. *J. Mater. Chem. A* **5**, 18044–18052 (2017).

51. Würfel, P. & Ruppel, W. The chemical potential of luminescent radiation. *J. Lumin.* **24**–**25**, 925–928 (1981).

52. Braly, I. L. *et al.* Hybrid perovskite films approaching the radiative limit with over 90% photoluminescence quantum efficiency. *Nat. Photonics* **12**, 355–361 (2018).

53. Guillemoles, J.-F., Kirchartz, T., Cahen, D. & Rau, U. Guide for the perplexed to the Shockley–Queisser model for solar cells. *Nat. Photonics* **13**, 501–505 (2019).

54. Kirchartz, T., Mattheis, J. & Rau, U. Detailed balance theory of excitonic and bulk heterojunction solar cells. *Phys. Rev. B - Condens. Matter Mater. Phys.* **78**, 1–13 (2008).

55. Ponseca, C. S. *et al.* Mechanism of Charge Transfer and Recombination Dynamics in Organo Metal Halide Perovskites and Organic Electrodes, PCBM, and Spiro-OMeTAD: Role of Dark Carriers. *J. Am. Chem. Soc.* **137**, 16043–16048 (2015).

56. Caprioglio, P. *et al.* On the Relation between the Open-Circuit Voltage and Quasi-Fermi Level Splitting in Efficient Perovskite Solar Cells. *Adv. Energy Mater.* **9**, (2019).

57. Son, D. Y. *et al.* Self-formed grain boundary healing layer for highly efficient CH3 NH3 PbI3 perovskite solar cells. *Nat. Energy* **1**, 1–8 (2016).

58. Park, H., Chaurasiya, R., Jeong, B. H., Sakthivel, P. & Park, H. J. Nickel Oxide for Perovskite Photovoltaic Cells. *Adv. Photonics Res.* **2**, 2000178 (2021).

59. Hutter, E. M., Kirchartz, T., Ehrler, B., Cahen, D. & Von Hauff, E. Pitfalls and prospects of optical spectroscopy to characterize perovskite-transport layer interfaces. *Appl. Phys. Lett.* **116**, (2020).

60. Yang, Y. *et al.* Top and bottom surfaces limit carrier lifetime in lead iodide perovskite films. *Nat. Energy* **2**, (2017).

61. Yang, Y. *et al.* Low surface recombination velocity in solution-grown CH 3 NH 3 PbBr 3 perovskite

single crystal. *Nat. Commun.* **6**, (2015).

62. Taheri, M. M. *et al.* Distinguishing bulk and surface recombination in CdTe thin films and solar cells using time-resolved terahertz and photoluminescence spectroscopies. *J. Appl. Phys.* **130**, (2021).

63. Zhao, X. H. *et al.* Determination of CdTe bulk carrier lifetime and interface recombination velocity of CdTe/MgCdTe double heterostructures grown by molecular beam epitaxy. *Appl. Phys. Lett.* **105**, (2014).

64. Agostinelli, G. *et al.* Very low surface recombination velocities on p-type silicon wafers passivated with a dielectric with fixed negative charge. *Sol. Energy Mater. Sol. Cells* **90**, 3438–3443 (2006).

65. Cacovich, S. *et al.* Light-induced passivation in triple cation mixed halide perovskites: Interplay between transport properties and surface chemistry. *ACS Appl. Mater. Interfaces* **12**, 34784–34794 (2020).

66. Vidon, G. *et al.* Mapping Transport Properties of Halide Perovskites via Short-Time-Dynamics Scaling Laws and Subnanosecond-Time-Resolution Imaging. *Phys. Rev. Appl.* **16**, 1 (2021).

67. Ono, L. K., Liu, S. & Qi, Y. Reducing Detrimental Defects for High-Performance Metal Halide Perovskite Solar Cells. *Angew. Chemie - Int. Ed.* **59**, 6676–6698 (2020).

68. Tennyson, E. M. *et al.* Multimodal Microscale Imaging of Textured Perovskite-Silicon Tandem Solar Cells. *ACS Energy Lett.* **6**, 2293–2304 (2021).

69. Katahara, J. K. & Hillhouse, H. W. Quasi-fermi level splitting and sub-bandgap absorptivity from semiconductor photoluminescence. *J. Appl. Phys.* **116**, (2014).

70. Paul, N., Guen, V. Le, Ory, D. & Lombez, L. Numerical model to extract materials properties map from spectrally resolved luminescence images. 70–74 (2018) doi:10.1109/pvsc.2017.8366049.

71. Ledinsky, M. *et al.* Temperature Dependence of the Urbach Energy in Lead Iodide Perovskites. *J. Phys. Chem. Lett.* **10**, 1368–1373 (2019).

72. Bercegol, A. *et al.* Imaging Electron, Hole, and Ion Transport in Halide Perovskite. *J. Phys. Chem. C* **124**, 11741–11748 (2020).

73. Brenes, R., Laitz, M., Jean, J., Dequilettes, D. W. & Bulović, V. Benefit from Photon Recycling at the Maximum-Power Point of State-of-the-Art Perovskite Solar Cells. *Phys. Rev. Appl.* **12**, 1 (2019).

74. Schileo, G. & Grancini, G. Halide perovskites: current issues and new strategies to push material and device stability. *JPhys Energy* **2**, (2020).

75. Hu, Y. *et al.* Understanding the Role of Cesium and Rubidium Additives in Perovskite Solar Cells: Trap States, Charge Transport, and Recombination. *Adv. Energy Mater.* **8**, (2018).

76. Wetzelaer, G. J. A. H. *et al.* Trap-Assisted Non-Radiative Recombination in Organic-Inorganic Perovskite Solar Cells. *Adv. Mater.* **27**, 1837–1841 (2015).

77. Prochowicz, D. *et al.* Correlation of recombination and open circuit voltage in planar heterojunction perovskite solar cells. *J. Mater. Chem. C* **7**, 1273–1279 (2019).

78. Tress, W. *et al.* Interpretation and evolution of open-circuit voltage, recombination, ideality factor and subgap defect states during reversible light-soaking and irreversible degradation of perovskite solar cells. *Energy Environ. Sci.* **11**, 151–165 (2018).

79. Cappelletti, M. A., Casas, G. A., Cédola, A. P., Peltzer y Blancá, E. L. & Marí Soucase, B. Study of the reverse saturation current and series resistance of p-p-n perovskite solar cells using the single and double-diode models. *Superlattices Microstruct.* **123**, 338–348 (2018).

80. Grancini, G. *et al.* One-Year stable perovskite solar cells by 2D/3D interface engineering. *Nat. Commun.* **8**, 1–8 (2017).

81. Sutanto, A. A. *et al.* Dynamical evolution of the 2D/3D interface: A hidden driver behind perovskite solar cell instability. *J. Mater. Chem. A* **8**, 2343–2348 (2020).

82. Cho, K. T. *et al.* Selective growth of layered perovskites for stable and efficient photovoltaics. *Energy Environ. Sci.* **11**, 952–959 (2018).

83. Mabrouk, S. *et al.* Increased Efficiency for Perovskite Photovoltaics via Doping the PbI2 Layer. *J. Phys. Chem. C* **120**, 24577–24582 (2016).

84. Liu, Y. *et al.* Stabilization of Highly Efficient and Stable Phase-Pure FAPbI3 Perovskite Solar Cells by Molecularly Tailored 2D-Overlayers. *Angew. Chemie - Int. Ed.* **59**, 15688–15694 (2020).

85. Prathapani, S., Choudhary, D., Mallick, S., Bhargava, P. & Yella, A. Experimental evaluation of room temperature crystallization and phase evolution of hybrid perovskite materials. *CrystEngComm* **19**, 3834–3843 (2017).

86. Kim, M. *et al.* Methylammonium Chloride Induces Intermediate Phase Stabilization for Efficient Perovskite Solar Cells. *Joule* **3**, 2179–2192 (2019).

87. Zanetta, A. *et al.* Manipulating Color Emission in 2D Hybrid Perovskites by Fine Tuning Halide Segregation: A Transparent Green Emitter. *Adv. Mater.* **34**, (2022).

88. Peán, E. V., Dimitrov, S., De Castro, C. S. & Davies, M. L. Interpreting time-resolved photoluminescence of perovskite materials. *Phys. Chem. Chem. Phys.* **22**, 28345–28358 (2020).

89. Lu, H. *et al.* Vapor-assisted deposition of highly efficient, stable black-phase FAPbI3 perovskite solar cells. *Science (80-.).* **370**, (2020).

90. Wei, Q., Zi, W., Yang, Z. & Yang, D. Photoelectric performance and stability comparison of MAPbI3 and FAPbI3 perovskite solar cells. *Sol. Energy* **174**, 933–939 (2018).

91. Dhar, N. High Efficiency c-Silicon Solar Cells Based on Micro-Nanoscale Structure High Efficiency c-Silicon Solar Cells Based on Micro-nanoscale Structure by Fred Semendy , Priyalal Wijewarnasuriya , and Nibir K . Dhar. 1–25 (2014).

92. Cuevas, A., Stocks, M., Macdonald, D., Kerr, M. & Samundsett, C. Recombination and trapping in multicrystalline silicon. *IEEE Trans. Electron Devices* **46**, 2026–2034 (1999).

93. Quantum efficiency.